Modeling Rough Energy Landscapes in Defected Condensed Matter

by

Paul Rene Monasterio Velasquez

B.S./B.A., University of California, Berkeley (2006)
S.M., Massachusetts Institute of Technology (2008)

Submitted to the Department of Nuclear Science and Engineering
in partial fulfillment of the requirements for the degree of

Doctor of Philosophy in Nuclear Science and Engineering

at the

MASSACHUSETTS INSTITUTE OF TECHNOLOGY

June 2010

Author .....
Department of Nuclear Science and Engineering
April 30, 2010

Certified by .....
Sidney Yip
Professor of Nuclear Science and Engineering and Materials Science
Thesis Supervisor

Certified by .....
Roland J-M. Pellenq
Visiting Professor of Civil and Environmental Engineering
Thesis Reader

Accepted by .....
Jacquelyn Yanch
Chair, Department Committee on Graduate Theses

Modeling Rough Energy Landscapes in Defected Condensed Matter

by

Paul Rene Monasterio Velasquez

Submitted to the Department of Nuclear Science and Engineering
on April 30, 2010, in partial fulfillment of the
requirements for the degree of
Doctor of Philosophy in Nuclear Science and Engineering

Abstract

This dissertation is a computational and theoretical investigation of the behavior of defected condensed matter and its evolution over long time scales. The thesis provides original contributions to the methodology used for simulating the slow evolution of complex condensed matter, as well as applications to three problems: hydrogen embrittlement of metals, radiation swelling, and cement setting. The problems are characterized by an increasing degree of complexity as the microstructure ranges from a crystalline alloy with few point defects to a highly damaged metal with partial amorphization to a semi-crystalline colloidal system.

First, we investigate the interactions of hydrogen with point defect clusters (PDC) in Fe-C alloys via a combination of density functional theory and a statistical mechanics model. We cast our PDC concentration results in a novel PDC dominance diagram representation that can be generalized to any type of alloy and impurities. We also calculate the migration mechanisms and energy barriers for the most relevant PDC species in Fe-H. Our results demonstrate the essential role of hydrogen-vacancy interactions in mediating the formation and migration of PDCs, and the relevance of these crystalline defects to the problem of hydrogen embrittlement.

Second, we study the effect of self-interstitial atoms (SIA) on radiation swelling at high dose rates. Using a combination of non-equilibrium molecular dynamics and two generalizations of the autonomous basin climbing (ABC) method, we characterize the structure and evolution of the defective species that result from SIA insertion during irradiation. Consistent with ion beam implantation experiments on surfaces, we show that, at high dose rates, swelling is a consequence of the nucleation and growth of disordered phases. This process is governed by a competition between defect generation and recrystallization, even at long times.

Third, a binary colloidal model incorporating sticky interactions is developed to simulate chemomechanical hardening, with an application to cement setting. The model, inspired by a coarse-grained analogy with stress-corrosion cracking, captures gelation, diffusion, and percolation kinetics. The model is characterized and the effects of various parameters on setting kinetics are discussed. We find that, as ob-

served experimentally, the induction time is dependent on the relative concentration and masses of the two colloidal phases. The application of ABC (static and dynamic) to the study of cement setting under more realistic conditions is also discussed, including objective means of calculating the effective elastic moduli of viscoelastic materials via atomistic simulations.

Thesis Supervisor: Sidney Yip
Title: Professor of Nuclear Science and Engineering and Materials Science

Thesis Reader: Roland J-M. Pellenq
Title: Visiting Professor of Civil and Environmental Engineering

Acknowledgments

Throughout my life I have been fortunate to have the support of a multitude of persons who have contributed in a variety of ways to my professional and personal development. Any of my accomplishments would have been impossible without the support provided by the shoulders of the giants of my life.

Thanks go first and foremost to my research advisor, Prof. Sidney Yip, for his always frank and wise advice, deep support, and priceless guidance during the completion of my PhD. Through my conversations and interactions with Prof. Yip not only have I enriched my knowledge about condensed matter physics and materials engineering, but I have also learned many valuable lessons necessary to suceed in any professional or personal endeavor. I feel very fortunate to have had the chance to work with and learn from him and I hope his exacting standards, emphasis on the fundamentals, and professionalism will stay with me during my career. Thank you Prof. Yip.

I would also like to acknowledge some of the other mentors who have played a pivotal role in my scientific formation throughout the years and who have helped shape my professional pathway to this day. My deepest thanks go to my doctoral thesis committee members Prof. Krystyn Van Vliet, Prof. Bilge Yildiz, Prof. Roland Pellenq, and Prof. Sow-Hsin Chen for their valuable suggestions and comments during my thesis research and during our collaborations. I also want to extend my gratitude to Prof. Brian Wirth at UC Berkeley, Prof. Nicola Marzari at Oxford University, Dr. Jaime Marian and Dr. Malvin Kalos at the Lawrence Livermore National Laboratory, and Prof. Rafael Sánchez Lamoneda at the Universidad Central de Venezuela who have provided important insight and support at various stages of my career.

I am also grateful for the support of all the members of the Yip group during the past four years. They all have contributed to to my scientific success and were always happy to provide helpful comments or an extra pair of eyes when debugging faulty algorithms. Many thanks to Dr. Akihiro Kushima, Dr. Timothy Lau, Dr. Mukul Kabir, Prof. Xi Lin, Dr. Xiaofeng Qian, Dr. Robert Boyer, and Dr. Emilio Silva for

their friendship and support.

In addition, I am greatly indebted to those who have been with me through good and bad and who have provided me with encouragement, advice, and many good moments and conversations during my years at MIT. My graduate experience would have been very different without Andrew Mastin, my comrade in exploring Boston's nightlife who was always available for a quick bite and insightful conversation, or without my fellow GSCers: Oaz Nir, Alex H. Chan, Kevin McComber, Wendy Lam, Rob Wang, and David Opolon. I am also very grateful for many lively chats with the always colorful Lydia Kamps, and for the many fond memories I have made alongside Kevin Davis, Christina Sedighi, Chris Heckman, Prateek Bhakta, Nick Hwang, Diana Nguyen, James Li, Pokai Chen, Angela Wu, and Emilie Dandan. I thank them all for their friendship.

Last, but certainly not least, I thank the most important people in my life and the reason for all of my efforts: my family. I cannot write enough words to thank my mother, sister, and grandmother for their love, unwavering support throughout the years, and for laying the foundations that have made me the man I am today. To them I dedicate this thesis and all of my work.

Contents

List of Figures

List of Tables

Chapter 1

Introduction

1.1 Motivation

One of the main factors limiting the development and improvement of new technologies is the lack of a truly fundamental understanding of the behavior of complex condensed matter. Various scientific and engineering challenges, ranging from the fabrication of superconducting wires for efficient electricity allocations to the development of ultralight long lasting batteries to the confinement of plasmas for fusion applications, are deeply linked to materials issues which remain unresolved.

Condensed matter research has changed dramatically during the past few decades as a result of the advent of high performance computing. Joining the traditional paradigm of experimental and theoretical work, modeling and simulation have emerged as powerful alternatives in understanding the behavior of complex many body systems such as those present in condensed matter problems [1]. When based on robust theoretical principles and validated against clean and rigorous experiments, computational methods drastically extend the reach of the traditional scientific method.

The applications are many. From analyzing the surface chemistry of catalysts [2] to calculating the heat conduction in fluids [3] to understanding the mechanical behavior of beams and trusses under stress [4], computational methods in condensed matter research have the ability to provide deep insights into a broad range of questions [1]. Nevertheless, it is precisely this breadth of systems, mechanisms, and complexity

which results in one of the most fundamental challenges of the field: the multiplicity of scales.

Any complex system can, in a reductionistic approach, be broken down into fundamental units which interact given a certain set of predetermined laws. This gives rise to, at least, two scales of complexity: one emanating from the individual behavior of the units and one, or many scales, arising from their collective interactions. In the case of condensed matter systems the fundamental units are chosen according to the desired resolution in the problem but are typically electrons (electron waves) or atoms. Answering a specific phenomenological question can then be fundamentally resolved by understanding how individual atoms or electrons interact with each other and then the statistical mechanics of their collective behavior.

Despite the apparent simplicity of this abstraction, such a straightforward approach fails in practice due to the changes in scales associated from going from the fundamental understanding of the units (atoms or electrons) to that of a macroscopic phenomenon. For perspective consider that twelve grams of carbon-12 contain 6.022×10^{23} atoms of carbon. The electronic structure of an atom is on the length scale of a picometer and the time scale at which atoms vibrate is less than 1/10 of a picosecond. On the other hand, many macroscopic phenomena of interest occur on length scales of over 1 m and in time scales of days or years. This range, spanning 12-15 orders of magnitude in both time and length is accompanied by an equally wide range of associated energies. Therefore, despite the power of modern computing and the highly parallelized architectures available, a "brute force" approach to simulation, in which a macroscopic number of electrons and atoms are allowed to interact for a macroscopic time, is impossible. Therein lies the challenge of multiscale modeling in condensed matter physics: the development of a methodology sufficiently complete to answer questions which cut across multiple length, time, and energy scales while remaining rigorous.

The challenge of multiple length scales and immense numbers of constitutive particles in a macroscopic sample has been addressed in a variety of ways, giving rise to theoretical breakthroughs such as statistical mechanics (to describe the interactions

of a large number of particles in a statistical manner), mean-field theories, and continuum mechanics. These theories rely on a simple understanding of the underlying atomic or electronic properties which are then coarse grained to capture only the essential interactions which then guide the larger scale behavior. Developing rigorous coarse graining procedures - in which the essential information from the fundamental scales is preserved at higher scales - is a challenging problem on its own. Nevertheless, progress in the creation of ab initio informed interatomic potentials [5–7] and approaches such as the quasicontinuum method [8] have greatly contributed to addressing the length scale challenge, though it still remains an active area of research. In tandem, developments in parallel computing, multiple core architectures, and various adaptations of the simulation algorithms have also provided partial computational solutions to the length scale question, allowing the division of large systems into smaller subunits that can be then rigorously simulated.

On the other hand, solutions which address the variation in time and energy scales remain a lot less developed. In some cases, such as the Bohr-Oppenheimer approximation [9], the disparity in time scales can be used as a simplifying assumption to treat a seemingly unified phenomenon as a combination of simpler phenomena occurring at different time scales. However, in general, time-driven methods such as Molecular Dynamics (MD), in which Newton's equations of motion determine the system dynamics, are dramatically limited by the time scale problem. In these methods, the magnitudes of the time steps required for accurate numerical integration need to be on the order of atomic vibrations, i.e., over 12 orders of magnitude away from macroscopic scales. The existence of widely different time scales also gives rise to more fundamental theoretical problems as some of our classical physical concepts become constrained. In particular, slow evolving systems compromise the most basic notion of an equilibrium state and necessitate the use of non-equilibrium methods for their understanding. This conceptualization of a physical system beyond its equilibrium state gives rise to one of the fundamental themes in this thesis, the idea of an *energy landscape.*

At their core, multiple relevant temporal scales emerge when a given phenomenon

consists of different kinetic mechanisms. This is also the case with spatial scales, and the properties of condensed matter have been proven to change dramatically with size, especially once the characteristic lengths drop to a few nanometers [10,11]. However, in the case of time and energy the problem is exacerbated by the fact that the properties of interest not only require the observation of the system as it evolves through time with a given mechanism, but the form of that mechanism itself also changes with time. As with many of the fundamental issues in condensed matter physics, this rich dynamic behavior has tremendous universality and takes place in seemingly unrelated systems ranging from steels under environmental attack to molten metals during casting to the unfolding of proteins. All of these systems share important characteristics: complex and disordered underlying microstructures and processes which comprise multiple kinetic mechanisms such as chemical and mechanical relaxation. These far-from-equilibrium complex materials, exhibiting multiple time scales in their evolution, represent the next frontier in the emerging field of computational condensed matter physics and multiscale materials modeling and are the primary subject of this dissertation.

1.2 Problem Statement

This thesis represents an investigation of multiple questions associated with the theoretical understanding of complex defected condensed matter systems and their evolution over time. In particular this work addresses the following specific topics:

1. Generalization of a theoretical and computational framework, the Autonomous Basin Climbing (ABC) method, for the analysis of slow dynamical systems: The ABC method [12] represents a computational alternative to time-driven and stochastic simulation methods and allows for the study of condensed matter systems which evolve over a large range of time scales. In this thesis, the theoretical underpinning of the method is described within the context of nonequilibrium statistical mechanics and transition state theory. In addition, the method is generalized from its static, microcanonical formulation to be consistent with both canonical and constant stress

ensembles as well as dynamic energy landscapes. Applications of the method in various contexts are also explored.

2. Calculation of the energetics, concentrations, and kinetics of hydrogen-containing point defect cluster species in Fe-C alloys and their connection with hydrogen embrittlement: Using a combination of density functional theory (DFT) and a statistical mechanics model, we study the interactions of hydrogen with point defects in Fe-C alloys, casting our results for the concentrations into a point defect cluster (PDC) dominance diagram highlighting the changes in the defect microstructure as a function of composition, in the spirit of a phase diagram. We find that as a result of the strong binding effects of vacancies on the stability of the clusters, hydrogen accumulation requires the total hydrogen and vacancy concentrations to be comparable. Furthermore, because of the interplay between repulsive and attractive binding processes, PDC populations in Fe-C-H are shown to effectively decouple into the binary systems Fe-C and Fe-H. This results in significant vacancy-hydrogen PDC populations even for low total hydrogen concentrations. We also study the energetics of methane formation in Fe-C alloys and their potential connection to hydrogen embrittlement. Additionally, we calculate, using the nudged elastic band (NEB) method coupled with DFT calculations, the migration mechanisms of the most prevalent PDCs in Fe-C-H. We then calculate an effective diffusivity as a function of hydrogen concentration in steels.

3. Analysis of the role of self-interstitial atoms in radiation swelling and the application of ABC and ABCD to the study of the evolution of irradiated microstructures: We analyze the effect of self-interstitial atom (SIA) implantation in Fe on the long run swelling of the material. Our MD simulations reveal that in this case, swelling is the result of the nucleation and growth of highly disordered phases. The evolution of these phases is found to be strongly dependent on the specific disorder topology. In particular, the dependence of swelling on the irradiation dose rate is non-monotonic and can be divided into three distinct stages in which the prevalent defected species changes from small relatively stable dislocation loops to small unstable highly disordered/partially amorphized pockets to larger and more stable pockets of defects. This

behavior is further explored at longer time scales by using the ABC method extension to isobaric systems post irradiation, as well as the ABCD method to study the complete evolution of the irradiated material during and after irradiation. The conclusions are consistent with those resulting from MD though additional, but minor, relaxation of the microstructure takes place at longer time scales. The combination of MD, constant stress ABC, and ABCD for the study of the long term evolution of irradiated microstructures is presented as a powerful simulation alternative for the study of cascade aging in irradiated materials.

4. Development of a colloidal model of chemomechanical hardening to simulate cement setting: We develop a binary colloidal model exhibiting the characteristic sigmoid, three-regime hardening behavior which characterizes a variety of soft condensed matter systems, such as cement slurries. The model, inspired by a coarse-grained analogy with stress corrosion cracking (SCC), gives rise to this behavior by the rapid formation of a gel phase in which the larger particles diffuse through until they form a strong percolating network. We present a comparison between experimental and theoretical methods of estimating effective shear moduli and viscosity of viscoelastic materials and propose an objective approach for calculating these viscoelastic moduli from atomistic simulations. We also characterize the effect of various model parameters on the setting behavior, comparing with experimental observations during C-S-H hydration. Finally, we present results on the evolution of the model using ABC as well as proposed refinements to more accurately model the energy landscapes and time evolution of hydrated C-S-H.

The thesis is divided into two parts, Theory and Applications, as follows. The first part, consisting of Chapter 2, discusses the theory and computational developments behind the modeling of condensed matter phenomena across multiple time and energy scales. The chapter starts from basic concepts in equilibrium and nonequilibrium statistical mechanics which give rise to the notion of an energy landscape (Section 2.1.) and its interpretation within the context of the time evolution of condensed matter systems. Section 2.2 gives an overview of the basics of atomistic simulation of materials and the limitations of the standard methodology in analyzing our problems of

interest. These limitations are addressed by the Autonomous Basin Climbing (ABC) method developed by Kushima and collaborators [12] which is described in Section 2.3. along with two generalizations for use in constant temperature (canonical) and constant stress simulations. The chapter closes with a description of a dynamic generalization to ABC, termed ABCD, which further extends the method to changing energy landscapes. The second part, comprising Chapters 3 through 5, leverages the methods described in Chapter 2 to study three distinct condensed matter problems characterized by an increasing degree of microstructural complexity, the combination of both chemical and mechanical processes, and roughness in their underlying energy landscapes. Chapter 3 discusses results concerning the problem of hydrogen embrittlement of metals. Section 3.1. describes results concerning the interactions of hydrogen with point defects in an iron lattice and the resulting distribution of defect clusters. Section 3.2 studies the migration and diffusion behavior resulting from those interactions and Section 3.3 highlights the implications to long run degradation and embrittlement. Chapter 4 follows with a study of the, more complex, microstructure of an irradiated metal which includes a large number of point defects and partial loss of order. Section 4.1. discusses the theories concerning the formation of voids in metals and how they lead to volumetric swelling. Section 4.2. takes a different emphasis and discusses the effects of self interstitial atoms (SIA) in the swelling process, in particular concerning the formation of highly disordered phases in the material. Section 4.3. further expands into the problem of swelling by discussing the evolution of irradiated materials over long time periods using the methods developed to model slow dynamical systems. Chapter 5 closes our study of rough energy landscapes in condensed matter by describing and analyzing a colloidal model of chemomechanical hardening with applications to cement setting. In this case, long range order is completely lost in favor of glass like behavior. Section 5.1. summarizes the basic experimental knowledge about cement hydration, setting, and hardening. Section 5.2. discusses the atomistic modeling of viscoelasticity in colloidal suspensions, highlighting the well known phenomena of shear thinning and thickening. In addition the section discusses the ways to estimate and measure viscosities and shear moduli in

viscoelastic materials within the context of the theory of isothermal linear viscoelasticity and linear response theory. Finally, in Section 5.3, by relying on a new binary colloidal model, we analyze the phenomenon of colloidal setting and the genesis of rigidity in soft condensed matter in the context of cement setting and C-S-H hydration. A summary of the results and their implications is given in Chapter 6, along with proposals for future work. In addition, a novel algorithm for synchronous parallel kinetic Monte Carlo in both continuum and discrete systems, a summary of a recently developed model of the atomic structure of CSH, and benchmarking of our ABC generalizations are provided in the appendices.

Theory

Chapter 2

Time Scales in Atomistic Simulation: Energy Landscape Approach

2.1 Nonequilibrium Statistical Mechanics

The field of statistical mechanics relies on the basic assumption that as a result of the large number of degrees of freedom in any macroscopic physical system, the properties of matter at the macroscale can be determined by averaging specific variables (or Hermitian operators when dealing with a quantum mechanical formalism) over an ensemble of microstates corresponding to the same macroscopic realization. This limit, at which the number of degrees of freedom tends to infinity, is then referred to as the *thermodynamic limit.* Each of the microstates is assumed to have an equal probability of occurring as any other, so long as they correspond to the same equilibrium macrostate. Macrostates, in turn, are defined by state variables such as the total energy, number of particles, and volume which characterize the observable state of the system.

This abstraction, bridging the behavior of individual constitutive particles and their collective interactions through ensemble averaging, relies on the concept of an

equilibrium in which the macrostate remains constant while the specific microstate can vary.

In nonequilibrium statistical mechanics, on the other hand, we seek to model time dependent processes beginning with an understanding of the motion and interactions of individual electrons, atoms, or molecules. Therefore, in addition to the changes in microstates, which occur even at equilibrium for a given ensemble, the macrostate itself is also allowed to change with time. In particular, taking the simplest of the equilibrium statistical mechanical ensembles - the microcanonical ensemble - out of equilibrium turns the system's potential energy into a dynamic variable. This gives rise to an essential concept in the study of dynamical systems in this thesis: *the energy landscape.*

For the nonequilibrium systems described above, both the micro and macrostates change with time. Nonetheless, there are direct correspondences between a given microstate (which can be analyzed with computational tools such as MD) and the system's total, kinetic, potential, and free energies. Although in real physical systems or in time driven simulation methods the processes by which the system moves from one microstate to another (which may or may not correspond to the same macrostate) take place as a function of time, the correspondence between microstates and energies is not explicitly time dependent. [1]

More precisely, to give a complete description of the state of a three-dimensional N-particle system at any given time it is necessary to specify the $3N$ coordinates and $3N$ momenta that describe the microstate. Then the equations of motion of the system result in motion through the $6N$ dimensional *phase space* (or Γ space) in which all microstates are points. We can then define the correspondence between a microstate $\mu = (\mathbf{q_1}, \mathbf{q_2}, ..., \mathbf{q_N}, \mathbf{p_1}, \mathbf{p_2}, ..., \mathbf{p_N})$ and the total, potential, and kinetic energies directly. In this case the correspondences are single valued and properly

[1] An explicit time dependence of the energy will result in a dynamic energy landscape. This generalization of our formalism is discussed in Section 2.4.

defined functions. So we can write:

$$E_{potential} = E_{potential}(\mu) = E_{potential}(\mathbf{q_1}, ..., \mathbf{q_N}, \mathbf{p_1}, ..., \mathbf{p_N}) \quad (2.1)$$

$$E_{kinetic} = E_{kinetic}(\mu) = E_{kinetic}(\mathbf{q_1}, ..., \mathbf{q_N}, \mathbf{p_1}, ..., \mathbf{p_N}) \quad (2.2)$$

$$E_{total} = E_{kinetic} + E_{potential} = E_{total}(\mu) = E_{total}(\mathbf{q_1}, ..., \mathbf{q_N}, \mathbf{p_1}, ..., \mathbf{p_N}) \quad (2.3)$$

For most cases of physical interest these relations can be further simplified by assuming that for a specific reference frame the potential energy depends exclusively on the position vectors while the kinetic energy depends on the momenta. Equations (2.1-2.3) then reduce to:

$$E_{potential} = E_{potential}(\mu) = E_{potential}(\mathbf{q_1}, ..., \mathbf{q_N}) \quad (2.4)$$

$$E_{kinetic} = E_{kinetic}(\mu) = E_{kinetic}(\mathbf{p_1}, ..., \mathbf{p_N}) \quad (2.5)$$

$$E_{total} = E_{kinetic} + E_{potential} = E_{total}(\mu) = E_{total}(\mathbf{q_1}, ..., \mathbf{q_N}, \mathbf{p_1}, ..., \mathbf{p_N}) \quad (2.6)$$

Then the vectors given by $(E_{potential}, \mu)$, $(E_{kinetic}, \mu)$, and (E_{total}, μ) (also denoted as $(\Phi(\mu), \mu)$, $(K(\mu), \mu)$, and $(H(\mu), \mu)$) are in $(3N + 1)$-, $(3N + 1)$-, and $(6N + 1)$-dimensional spaces respectively, and give rise to hypersurfaces. These complete hypersurfaces, which characterize the correspondences between the energies and the microstates as described by Equations (2.4-2.6) are what we term energy landscapes. In this thesis we focus on potential energy landscapes, to which we will refer to as energy landscapes without the "potential" qualifier from now on and unless otherwise noted.

The relation between the microstate and the system's potential energy becomes particularly powerful when metastable or local equilibrium macrostates occur. In such cases we can allow the system to relax by changing its microstate (associated to potentially different macrostates) until a local equilibrium is reached corresponding to an *energy well* or local minimum of the energy landscape. As explained in the following subsection, it is precisely the topology of these wells and of the local energy landscape that determines the time evolution of the system and the time dependent

properties or transport coefficients.

2.1.1 Transition State Theory

The connection between energy landscapes and the kinetics of physico-chemical processes was established in 1935 by Henry Eyring, Meredith Gwynne Evans, and Michael Polanyi within the context of the rates of chemical reactions [13–16]. While the concept of an energy landscape had been laid by Rene Marcelin, who proposed that the progress of a chemical reaction could be described as the motion of a point in the energy landscape, the actual calculation of a real energy landscape did not occur until Eyring, Evans, and Polanyi's seminal work. In this section we summarize essential results in transition state theory (TST) [16,17] which are used repeatedly throughout the thesis.

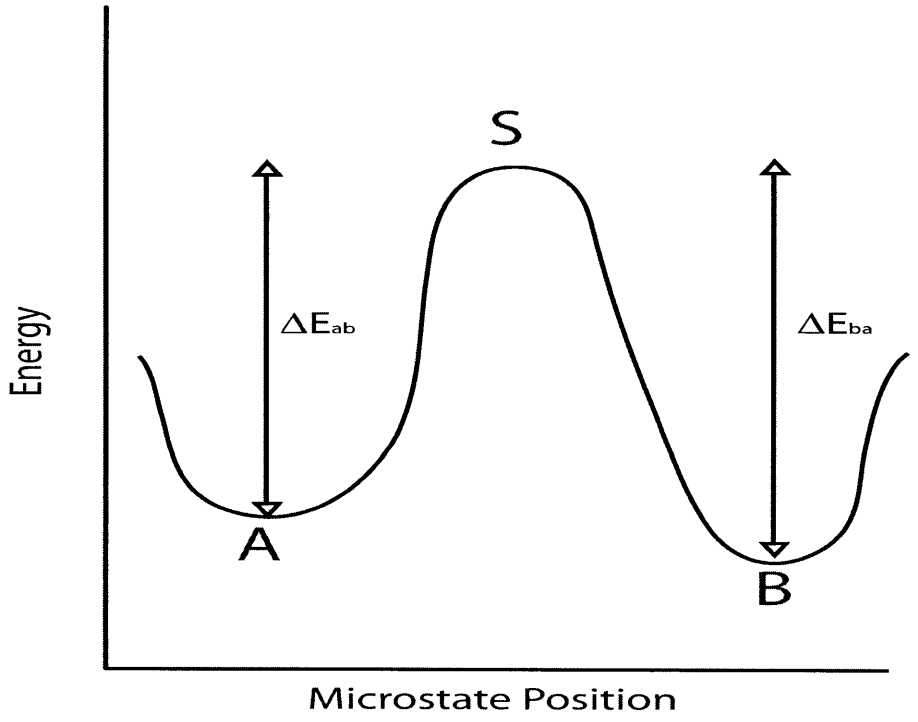

Figure 2-1: Schematic of the energy landscape between two microstates A and B. S denotes the intermediate saddle point and ΔE_{ab} and ΔE_{ba} denote the forward and backward activation energy barriers respectively.

The basic equation in transition state theory (TST) [16] relates the rate of a

physico-chemical process to its associated energy landscape. In particular, considering a physical process (chemical reaction) in which the system begins at a microstate A, e.g. a microcanonical microstate such as the ones described in the previous section or a Grand canonical microstate for chemical reactions, and finishes at a microstate B, gives rise to two associated energies in the landscape: $\Phi(A)$ and $\Phi(B)$ (we assume without loss of generality that we are referring to microcanonical microstates though the abstraction can be trivially generalized to other ensembles). Taking a continuous path between A and B, and if the function in Equation (2.4) is continuous and non-diverging, then by the intermediate value theorem that there is a microstate S such that $\Phi(S)$ is a maximum in the path. Furthermore if A and B are chosen to be local equilibrium states, i.e., $\Phi(A)$ and $\Phi(B)$ are local minima, then S is different from A and B and is then a saddle point in the landscape associated with energy $\Phi(S)$ (see Figure 2.1). We can then define two activation energy barriers for the $A \rightarrow B$ transition (forward and backward) as:

$$\Delta E_{ab} = \Phi(S) - \Phi(A) \tag{2.7}$$

$$\Delta E_{ba} = \Phi(S) - \Phi(B) \tag{2.8}$$

Now consider the unique hyper-surface Σ of dimensionality $3N$ passing through the saddle point S and perpendicular to the constant energy contours. With this construction, Σ divides phase space into two separate regions in which A and B lie respectively (see Figure (2.2)). Calculating the rate of the transition is equivalent to calculating the rate at which points in the $3N$-dimensional phase space cross the surface from "left" to "right" (i.e., from the region which point A lies to that in which point B lies) [17], which is given by:

$$\Gamma = \frac{I}{Q_A} \tag{2.9}$$

where I is the number of points moving from "left" to "right" per unit time, and Q_A is the number of points in the region "left" of Σ. In the case of our energy

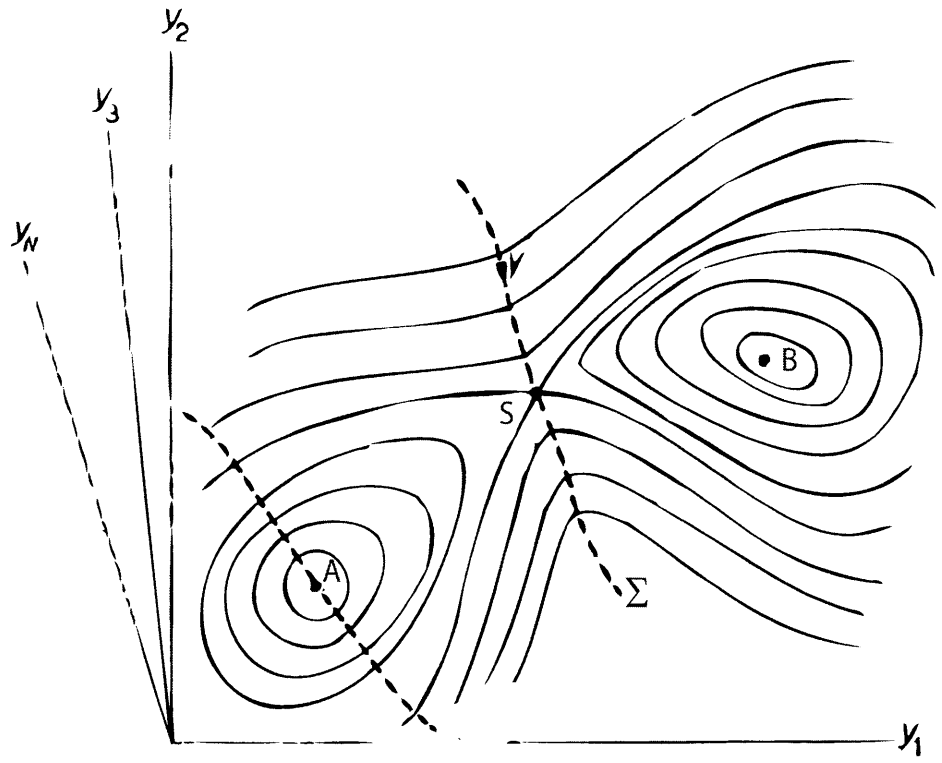

Figure 2-2: Schematic of the constant energy contours describing the landscape between two microstates A and B of the dividing hyper-surface Σ [17].

microstates, we can calculate Q_A from the canonical distribution as:

$$Q_A = \rho_0 \int_A e^{\frac{-\Phi}{kT}} dv \tag{2.10}$$

where ρ_0 is a normalizing constant, k denotes Boltzmann's constant, T the system temperature, Φ denotes the potential energy function from Equation (2.4), and the integration is over all phase space "left" of Σ. I can be calculated by noticing that the number of representative points at any given point Y of Σ per unit volume, with hyper-velocity $\mathbf{V} = (\dot{y_1}, \dot{y_2}, ..., \dot{y_{3N}})$ within a range $d\mathbf{V}$ is given by:

$$\rho(Y, \mathbf{V}) = \rho_0 (2\pi kT)^{-3N/2} e^{\frac{-\Phi(Y)}{kT}} \cdot e^{\frac{-\mathbf{V}^2}{2kT}} d\dot{y_1} \cdots d\dot{y_{3N}} \tag{2.11}$$

Then dI is given by:

$$dI = d\Sigma \int \mathbf{V}\rho(Y, \mathbf{V})d\mathbf{V} \tag{2.12}$$

where $d\Sigma = (d\Sigma_1, ..., d\Sigma_N)$ is an infinitesimal section of Σ around Y, and the integration is performed over all $\mathbf{V}$ such that $dS \cdot \mathbf{V} > 0$. Therefore from Equations (2.11) and (2.12), I is given by:

$$I = \int dI = \rho_0 \sqrt{kT/2\pi} \int_S e^{\frac{-\Phi}{kT}} dS \tag{2.13}$$

so plugging into Equation (2.9) we find:

$$\Gamma = \sqrt{\frac{kT}{2\pi}} \frac{\int_S e^{\frac{-\Phi}{kT}} dS}{\int_A e^{\frac{-\Phi}{kT}} dv} \tag{2.14}$$

Classical TST then assumes that the integrals can be simplified by taking an average of an uniform potential energy function. This implies that the rates corresponding to this process (A to B) and its inverse are given by:

$$\Gamma_{ab} = \nu_{ab} e^{\frac{-\Delta E_{ab}}{kT}} \tag{2.15}$$

$$\Gamma_{ba} = \nu_{ba} e^{\frac{-\Delta E_{ba}}{kT}} \tag{2.16}$$

where ν_{ab} and ν_{ba} are both constants associated with the average frequency of attempts and associated with natural vibrations of the system. While quantum corrections, introduced to account for tunneling effects, add a multiplier to Equations (2.9) and (2.10), these effects are minimal for the problems discussed in this thesis. More importantly, though, while for many applications the attempt frequencies ν_{ab} and ν_{ba} are phenomenologically chosen to correspond to average vibration frequencies in the material of interest, they can be rigorously calculated following the seminal work of Vineyard [17] by invoking a harmonic approximation of the energy landscape, in what is termed Harmonic Transition State Theory (HTST). We expand Φ to second order

around point A by letting:

$$\Phi = \Phi(A) + \sum_{j=1}^{3N} \frac{1}{2}(2\pi\nu_j)^2 q_j^2 \tag{2.17}$$

where we abuse the notation somewhat by letting $q_1, .., q_{3N}$ be the normal coordinates (scaled by the mass) and $\nu_1, ..., \nu_{3N}$ the corresponding normal vibration frequencies at point A. Similarly around the saddle point S we can expand the potential energy function in the hyper-surface Σ as:

$$\Phi = \Phi(S) + \sum_{j=1}^{3N-1} \frac{1}{2}(2\pi\nu_j')^2 q_j'^2 \tag{2.18}$$

where $q_1', .., q_{3N-1}'$ are the corresponding normal coordinates and $\nu_1', ..., \nu_{3N-1}'$ the corresponding normal vibration frequencies at point S. Plugging Equations (2.17) and (2.18) into (2.14) we find:

$$\Gamma = (\frac{\prod_{j=1}^{3N} \nu_j}{\prod_{j=1}^{3N-1} \nu_j'}) e^{-[\Phi(S)-\Phi(A)]/kT} \tag{2.19}$$

and therefore, from Equation (2.15) (and analogously for Equation (2.16)) we find:

$$\nu_{ab} = \frac{\prod_{j=1}^{3N} \nu_j^A}{\prod_{j=1}^{3N-1} \nu_j^S} \tag{2.20}$$

$$\nu_{ba} = \frac{\prod_{j=1}^{3N} \nu_j^B}{\prod_{j=1}^{3N-1} \nu_j^S} \tag{2.21}$$

where ν_j^P denotes the j-th normal frequency around point P.

2.1.2 Microstructural Complexity and Rough Energy Landscapes

Slowly evolving systems tend to result from four strongly related causes: naturally rough energy landscapes due to complex microstructure, the combination of processes

with different kinetic mechanisms such as chemistry and mechanics, external perturbations driving the system far from equilibrium, or the coupling of all three. These alternative driving forces give rise to two different transport coefficients [18]: *externally driven transport coefficients*, arising from an external perturbation, or *thermal transport coefficients*, where the rough energy landscape or boundary conditions in question are the ones giving rise to the transport.

While at each instant in time the specific microstate in the system is constantly fluctuating, the macrostate (characterized by gross, macroscopic variables such as total energy or volume) only evolves slowly by jumping from one local minima in the energy landscape to another. *Transport* is then defined as this slow migration of macrostates through the landscape and associated to the underlying microstructural evolution of the system. Appendix B summarizes the main ideas in the linear response theory of transport culminating in fluctuation-dissipation theorems for both thermal and externally driven transport coefficients. These results are used in various sections in the thesis.

TST and linear response theory link the time evolution of a physico-chemical process with the underlying topology of the energy landscape. In particular, and as highlighted in Chapter 1, the topology of the energy landscapes for systems whose behavior takes place over a wide range of time scales is highly complex. Condensed matter systems which exhibit such behavior range from solid to glassy to liquid, from metals to semiconductors to ceramics, and from mechanically to electrically to chemically driven. Nonetheless, these system share important similarities in the complexity of their underlying microstructures, and this gives rise to multiple mechanisms and time scales.

The complex microstructures which give rise to so-called *rough energy landscapes*, characterized by the presence of wells, plateaus, and valleys with very distinct topology interspersed with many energy barriers of comparable height and curvature (see Figure 2.3 for an illustration), tend to share three important characteristics:

- They are far from equilibrium due to external chemical, electrical, or mechanical stresses.

- Highly defective microstructures.
- Kinetic processes at different scales, such as chemistry and mechanics, occur on equal footing.

Systems far from equilibrium tend to result from constant external forces that effectively distort the energy landscape, such as electric fields, chemical fields or irradiation, or from a highly distorted landscape topology in which shallow wells are interspersed with deep energy wells giving rise to very slowly evolving states.

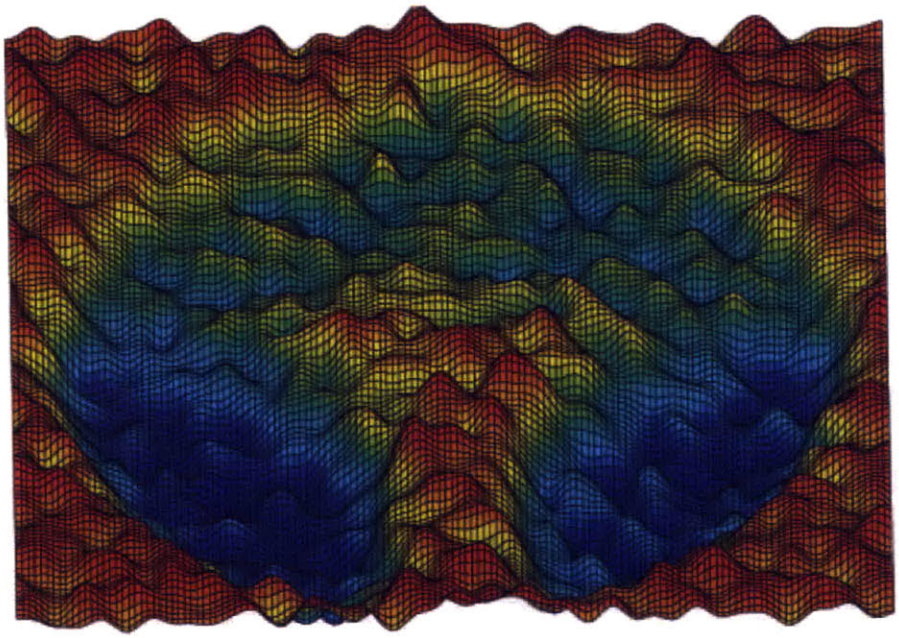

Figure 2-3: Illustration of a two-dimensional rough energy landscape. At a suitable temperature, the two dark blue regions are metastable states in which the macrostates spend most of the time; yet transitions occur infrequently, mainly via the light blue/yellow rough valley [19]

High disorder configurations normally produce frustrated or metastable states due to the large activation energies required for relaxation and as a result, in addition to their technological applications, highly defected materials represent prime examples for the study of slow relaxations and rough energy landscapes. The framework for calculating transport coefficients in these systems is based on linear response theory, transition state theory, and atomistic simulations which will be discussed sub-

sequently. As will become apparent in latter sections and chapters, the increase in complexity in both microstructure and energy landscape topology requires the use of more powerful and innovative theoretical frameworks and modeling techniques in order to understand the system. Nonetheless, and despite the increasing ingenuity and power of the simulation methods, the type of physical conclusions that can be extracted become less definite as complexity increases.

Such defective systems, ranging from crystalline solids to amorphous or semi-crystalline colloidal suspensions, are explored in the second part of this thesis, which is concerned with applications of our theoretical developments. As such, and for completeness, here we summarize the most essential features of the complex microstructures in which our methods will be applied.

In the case of crystalline materials these defects, responsible for much of the energy landscape roughness, and their associated complexity, can be categorized according to their spatial dimension:

Point defects, those which do not extend in space in any dimension, comprise the two most fundamental irregularities in a perfect lattice: vacancies and interstitials. In the case of an impurity, the atom is often incorporated at a regular atomic site in the crystal structure. This defect, called a substitutional defect, is neither a vacant site nor is the atom on an interstitial site. The atom is not supposed to be anywhere in the crystal, and is thus an impurity. Small atoms, such as hydrogen, in some crystals can occupy interstitial sites without high energy. We study the evolution of such a system in Chapter 3 within the context of hydrogen embrittlement of metals. The energy landscape in that case is dependent on the geometry of individual point defect clusters as well as on the overall concentrations of defect species in the material.

Line defects, which can be described by gauge theories, include dislocations, essential in the study of crystal plasticity, and disinclinations which are observed in liquid crystals. Although dislocations are of paramount importance in understanding embrittlement in metals and creep, we only discuss them tangentially in this thesis while proposing ways to generalize our approaches to their study.

Planar defects, such as grain boundaries, anti-phase boundaries, and stacking

faults, are characterized by their two-dimensional topologies in a three-dimensional bulk. While present in most materials and important in the slow dynamics of Coble creep, we also omit them from most of this work. Finally, bulk defects include voids and precipitates which are agglomerations of point defects.

Topological defects are regions in a crystal where the normal chemical bonding environment is topologically different from the surroundings. For instance, in a perfect sheet of graphite (graphene) all atoms are in rings containing six atoms. If the sheet contains regions where the number of atoms in a ring is different from six, while the total number of atoms remains the same, a topological defect has formed. An example is the Stone Wales defect in nanotubes, which consists of two adjacent 5-membered and two 7-membered atom rings. Also amorphous solids may contain defects. These are naturally somewhat hard to define, but sometimes their nature can be quite easily understood. For instance, in ideally bonded amorphous silica all Si atoms have 4 bonds to O atoms and all O atoms have 2 bonds to Si atom. Thus e.g. an O atom with only one Si bond (a dangling bond) can be considered a defect in silica. These type of defected structures, which give rise to very slow relaxation behavior, are explored in Chapters 4, in which local amorphization occurs as a result of high irradiation dose rates in Fe, and Chapter 5, in which we study flow, gelation, and solidification of amorphous colloidal suspensions as a function of time.

2.2 Review: Atomistic Modeling Fundamentals

Two main classes of computational methods are used in the atomistic modeling of condensed matter systems, both in and far from equilibrium: time driven and stochastic methods. For these classes of methods the system goes through different microstates in either a dynamic fashion, in which the system evolves naturally as a function of time, or by directly sampling from a distribution of microstates, respectively. The first class of methods, with a natural time evolution, rely on time averaging to determine equilibrium properties and an analysis of the time evolution for non-equilibrium ones. This class is spearheaded by Molecular Dynamics (MD), the oldest and most

basic, yet extremely powerful, atomistic modeling tool. The second class relies on probabilistic tools. These methods directly sample the microstates corresponding to a given macrostate, in the case of equilibrium systems, or sample the microstates directly from the energy landscapes described previously, for non-equilibrium processes. This class of methods is headlined by the Monte Carlo (MC) and kinetic Monte Carlo (KMC) algorithms. The equivalence of these two classes of computational tools to describe the behavior of physical systems relies on the axiom of *ergodicity*, which assumes that in the thermodynamic limit the system goes through a sufficient number of microstates as it evolves in time to ensure that time averages are statistically equivalent to ensemble averages. For finite simulations the axiom of ergodicity gains an additional dimension, as time averages are dependent not only on the nature of the system but also in the time range over which the average is taken. This results in a lack of ergodicity in practice even for systems that would otherwise be ergodic for infinite simulations. This is particularly important for the complex condensed matter systems of interest in this thesis since the roughness of the underlying energy landscapes limits the applicability of time driven methods such as MD because the system remains constrained in deep potential energy wells for times which are on the order of or higher than the allowable simulation time.

2.2.1 Molecular Dynamics

Molecular Dynamics (MD) is the most basic of the time driven methods. In MD we follow the laws of classical mechanics [20], in particular Newton's second law:

$$\mathbf{F}_i = m_i \mathbf{a}_i \tag{2.22}$$

for each atom i in a system of N atoms. Where $\mathbf{a}_i = \frac{d^2\mathbf{q}_i}{dt^2}$ is the acceleration, $\mathbf{F}_i$ is the force resulting from interactions with other atoms, and m_i is the mass of the atom. The many-body problem then reduces to the resolution of the system of coupled second-order differential equations as a function of time. MD is thus a deterministic method (within the constraints of finite integration and possibly chaotic behavior) in

which the initial conditions uniquely define the full solution to the system.

While fully quantum mechanical MD simulations are possible through the Car-Parrinello method [21], the majority of simulations of atomistic systems with MD are carried out using the classical equations of motion. This approximation is valid so long as the de Broglie thermal wavelength, given by:

$$\Lambda = \sqrt{\frac{2\pi\hbar^2}{MkT}} \tag{2.23}$$

satisfies $\Lambda << a$, where M is the atomic mass, k is Boltzmann's constant, and T is the temperature, and a is the mean nearest neighbor separation. For liquids and colloidal suspensions, Λ/a is of the order of 0.1 for light elements, and decreases for heavier elements such as C and Fe. For very light systems such as hydrogen or helium molecules the classical approximation is poor and a quantum mechanical treatment is needed.

MD simulations naturally lead to a time driven evolution of the system. After possible initial transients (which may be long lasting), the phase space distribution function characterizing the location of the microstates becomes essentially time independent. In this case, the properties of the system relax to fixed average values for equilibrium systems, as well as for metastable non-equilibrium steady states. For this system we evaluate any phase variable B by resorting to a time average given by:

$$\langle B \rangle_t \equiv \lim_{T \to \to \infty} \frac{1}{T} \int_{t_0}^{t_0+T} B(t)dt \tag{2.24}$$

where t_0 is the time after which the system reaches the (meta)stable state.

While size limitations for MD simulations have been greatly reduced with the implementation of highly efficient parallel algorithms which allow for simulation of up to a billion atoms [22], simulating slowly evolving systems still remains a major challenge. A simulation can be considered rigorously accurate in regards to its duration if the simulation time is much longer than the relaxation time of the quantities of interest [20]. However complex microstructures such as those described in the previous

section and systems close to phase transitions exhibit very slow and sluggish behavior because collective motions, requiring the surmounting of a large energy barrier, are required for relaxation. Since MD simulations must resolve atomic vibrations the time step for integrations needs to be on the order of 10^{-15} s for most materials. This therefore limits the total simulation times to less than one microsecond which is insufficient for allowing slow systems to rigorously relax.

The connection between the energy landscape and the system dynamics is very direct in an MD simulation. If the potential energy function in Equation (2.4) is translationally and rotationally invariant, as is generally the case, then the forces in Equation (2.22) are given by the as gradients of the potential with respect to displacements as:

$$\mathbf{F}_i = -\nabla_{\mathbf{q}_i}\Phi(\mathbf{q}_1, ..., \mathbf{q}_N) \tag{2.25}$$

In general, though, the potential function is written as the sum of individual, pair, and local terms, so understanding the instantaneous relationship between the function and the trajectories is insufficient to calculate the topology of the landscape explicitly.

Nonetheless, this form leads in a straightforward way to the conservation of total energy in the system and therefore, under ergodic assumptions, standard MD simulations following a Hamiltonian $\mathcal{H}(\mu)$ generate a phase space probability distribution $\delta(\mathcal{H}(\mu)-E)$ (constrained by other conservation laws such as angular momentum [23]), which is the microcanonical ensemble. Constant temperature MD simulations, corresponding to the canonical ensemble, can be achieved by coupling the system to a thermostat. This can be achieved in variety of ways ranging from velocity rescaling, which does not completely reproduce the statistics of the canonical ensemble, or more precisely via Langevin-type dynamics such as the Nosé-Hoover thermostat [24]. In this case the microstates sample the probability distribution $\exp(-\beta\mathcal{H}(\mu))$ where $\beta = 1/kT$. Additionally we can perform constant stress and constant temperature MD simulations which can be directly compared with experiments by combining Nosé-Hoover thermostats with Parrinello-Rahman dynamics [25] in which the system

evolves according to the Lagrangian:

$$\mathcal{L} = \frac{1}{2}\sum_{i=1}^{N} m_i \dot{\mathbf{s}}_\mathbf{i}' \mathbf{G} \dot{\mathbf{s}}_\mathbf{i} - \Phi(\mathbf{q_1}, ..., \mathbf{q_N}) + \frac{1}{2} W_{piston} Tr \dot{\mathbf{h}}' \dot{\mathbf{h}} - pV - 1/2 Tr \mathbf{\Sigma G} \qquad (2.26)$$

where $\mathbf{h}$ is the matrix defining the unit cell, $\mathbf{s_i} = \mathbf{h}^{-1}\mathbf{q_i}$ are the fractional coordinates, p is the hydrostatic pressure, V is the volume and:

$$\mathbf{G} = \mathbf{h}'\mathbf{h} \qquad (2.27)$$

$$\Sigma = \mathbf{h_0}^{-1}(\mathbf{S} - p)\mathbf{h}_0'^{-1} V_0 \qquad (2.28)$$

where $\mathbf{S}$ is the stress tensor and $\mathbf{h_0}$ is the initial cell shape. With the system evolving according to this Lagrangian it changes its shape in response to stresses. In the particular case of constant pressure, the microstates sample the isobaric-isothermal ensemble.

2.2.2 Kinetic Monte Carlo

As explained previously, the ergodic hypothesis conjectures that ensemble averages over the energy landscape are the same as time averages. Hence as a simulation alternative to the time driven methodologies (such as MD) we can directly sample the probability distribution of the ensemble and calculate the properties by averaging. The algorithms used to sample the probability distribution rely on random numbers and belong to a broad class of, so called, Monte Carlo methods.

The most famous of such methods is the Metropolis algorithm [26] which elegantly samples the equilibrium properties of a given physical ensemble. To study the dynamic evolution of the system as it moves from microstate to microstate, Monte Carlo methods can be adapted to evolve dynamically in what has come to be known as kinetic Monte Carlo (KMC). The scope of applications of KMC is extremely wide, ranging from population kinetics to radiation damage [27].

The interest on KMC results from MD's inherent limitation in simulating long time scales. As described previously the need to use time steps short enough to resolve

atomic vibrations (10^{-12} s) limits the maximum MD simulation. KMC attempts to overcome this limitation by exploiting the fact that the long run dynamics typically consist of diffusive jumps from state to state. Rather than following the full microstate trajectory, the state-to-state transitions are treated directly. As a result KMC can reach much longer time scales, above seconds and beyond [27]. The key assumption in KMC is that the topology of the energy landscape is such that a microstate caught in a basin stays there for a long time and forgets its history. Then for each possible escape path we can characterize the jump from basin i to basin j by a rate constant Γ_{ij}, which can be calculated from TST as in Section 2.1.1. Thus KMC relies on *a priori* knowledge of a given set of transition rates characterizing the simulated processes, which are assumed to obey Poisson statistics, and lead to a Markov chain. Based on this approach, if we know the transition rates exactly or alternatively, if we know the energy landscape topology perfectly, then the time evolution of average properties in the KMC approach is indistinguishable from that of a MD simulation.

The most widely used variant of the method is the Monte Carlo time residence algorithm, also known as rejection-free n-fold method, or BKL in reference to its authors [28]. Assuming the complete set of transition rates is available the algorithm proceeds as follows:

- Consider a microstate located at an initial basin i with M possible escape pathways $j = 1, 2, .., M$ and known corresponding transition rates Γ_{ij}.
- Let $\Gamma_{tot} = \sum_{j=1}^{M} \Gamma_{ij}$ and $q_l = \sum_{j=1}^{l} \Gamma_{ij}/\Gamma_{tot}$.
- Select a random number η between 0 and 1.
- Then if $q_{n-1} \leq \eta \leq q_n$ for $1 \leq n \leq M$ the pathway n with corresponding transition rate $\Gamma = \Gamma_{in}$ is chosen and the system microstate is changed to that corresponding to basin n.
- Independently elect another random number ζ between 0 and 1.
- We advance total simulation time by τ, where $\tau = -\frac{1}{\Gamma}\ln(\zeta)$, and repeat the process.

With this simple algorithm the microstate moves from basin to basin in the energy landscape while maintaining rigorous Poisson statistics.

Despite its power and breadth of applications, KMC has two major flaws that limit its applicability. The first issue is associated with the inputs to the KMC algorithm: the assumption of *a priori* known transition rates and pathways is a strong one. In particular, an incorrect choice of potential pathways prevents specific mechanisms from occurring even if they are possible options physically and would be realized in a MD simulation. Since KMC requires such rates as inputs an additional technique must be used for their calculation or estimation. In the literature this can be accomplished by using energy landscape sampling methods such as NEB [29] in conjunction with TST, or by fitting experimental coarse grained observations. However, even if the rate itself can be estimated, the actual possible pathways need to be collectively exhaustive or important physical mechanisms may be lost. The second issue is related to the practical implementation of KMC in the case of rough energy landscapes such as those studied in this thesis. In that case shallow basins or wells are interspersed with deeper ones and as such the algorithm can jump from shallow basins to shallow basins continuously without much gain in total simulated time. Furthermore when very shallow basins - corresponding to more frequent events - are present, the "loss of memory" assumption is not necessarily valid and the Markov chain formalism can fail to capture the correct evolution. As will be discussed in the following section both of these issues are resolved by using an altogether different method termed Autonomous Basin Climbing (ABC).

Finally, in addition to the two major problems highlighted above, KMC has another important shortcoming. Unlike MD simulations which can take advantage of highly parallelizable computer architectures with simple algorithms in order to, partially, address the length scale challenge, KMC simulations do not lend themselves to trivial parallel implementations. The problem lies in the intrinsic time discreticity underlying event-driven (as opposed to time-driven) simulations, which are sequential in character. Several parallel algorithms for KMC have been proposed with various degrees of rigor and efficiency but they have received limited acceptance. Nonethe-

less, Appendix A presents details on a new synchronous parallel kinetic Monte Carlo (PKMC) algorithm for both continuous and discrete/lattice-based systems which addresses some of these issues.

2.3 Autonomous Basin Climbing

Both the time-driven and stochastic approaches described in the previous section have obvious limitations in dealing with the slowly evolving systems and rough energy landscapes that we study in this thesis. The principles of TST described in Section 2.1. suggest an alternative approach to the time evolution of condensed matter systems directly relying on the energy landscape that circumvents the need for *a priori* inputs that limits the effectiveness of KMC. This is the basic idea behind some recent acceleration methodologies such as metadynamics [30,31] and the Autonomous Basin Climbing (ABC) method [12] on which rely for various applications in this thesis. In this section we discuss the principles of ABC's microcanonical incarnation as developed by Kushima et al., and present two new extensions of the method to the canonical and constant stress ensembles.

The ABC method developed by Kushima et al. [12] generates a set of inherent structures and activation energy barriers from which the dynamical variables (viscosity of supercooled liquids in its original application) can be determined. The inherent structures correspond to the local minima in the energy landscape which are found by quenching a system from configurations generated by constant temperature MD simulations. Different temperatures allow the system to sample multiple regions of phase space and thus lead to the underlying structures of the system at a given temperature. More importantly, the ABC method is able to also sample the saddle points in addition to the local minima (or inherent structures) and hence provides a more complete topological picture of the energy landscape. The algorithm by which the ABC method samples the topology is schematically illustrated in Figure 2.4 and is a modification of that introduced by Laio and Parrinello [30] and which is the basis of metadynamics methods.

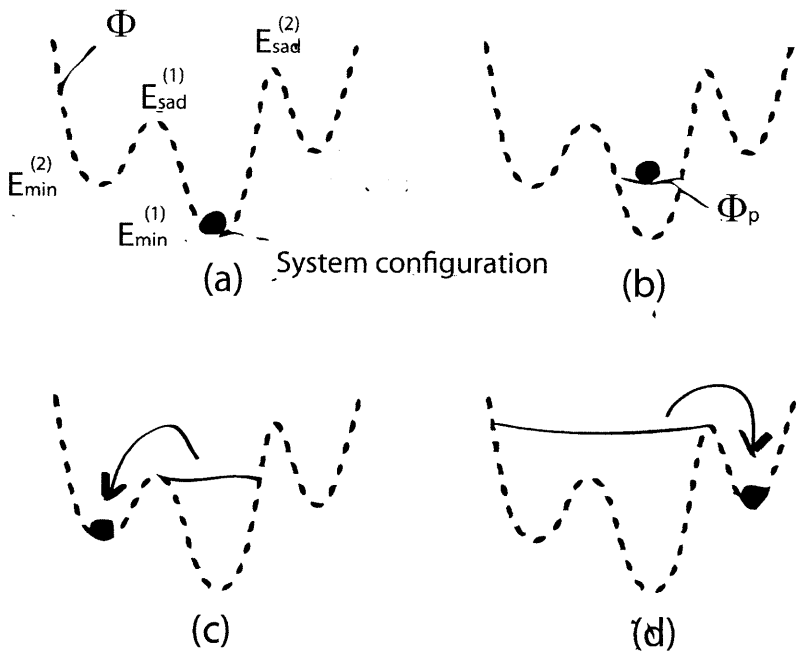

Figure 2-4: Schematic illustration explaining the Autonomous Basin Climbing (ABC) method. Dashed and solid lines indicate the original and penalty potential energy landscapes respectively [12].

We consider an initial microstate that is relaxed to a local minimum in the energy landscape with spatial configuration $\mathbf{Q}_{min}^{(1)} = (\mathbf{q}_1^{min}, ..., \mathbf{q}_N^{min})$ and with corresponding potential energy given from Equation 2.4: $E_{min}^{(1)} = \Phi(\mathbf{Q}_{min}^{(1)})$. The system is then driven away from this configuration by imposing an additional penalty function to the potential energy which results in fictitious forces which move the system out of the basin. This penalty function is given by a 3N-dimensional Gaussian as:

$$\phi_1(\mathbf{Q}) = W \exp(-\frac{(\mathbf{Q} - \mathbf{Q}_{min}^{(1)})^2}{2\sigma^2}) \tag{2.29}$$

where the parameters W and σ are prescribed constants which determine the strength and curvature of the fictitious penalty. The total (penalized) system potential energy then becomes $\Phi_p^1 = \Phi + \phi_1$. The microstate is then relaxed in the new penalized landscape by standard energy minimization procedures until it reaches a new config-

uration $\mathbf{Q}_{int}^{(2)}$ with corresponding energy $E_{int}^{(2)}$. The process is then repeated by adding more penalty functions of the form in Equation (2.29) but centered in the new configuration until a new local minimum configuration $\mathbf{Q}_{min}^{(2)}$ is identified by checking that both $\partial\Phi/\partial\mathbf{Q}(\mathbf{Q}_{min}^{(2)}) = 0$ and $\phi_p(\mathbf{Q}_{min}^{(2)}) = 0$. The minimization path is backtracked until the saddle point separating the two minima is identified, corresponding to a configuration $\mathbf{Q}_{sad}^{(12)}$ with energy $E_{sad}^{(12)}$.

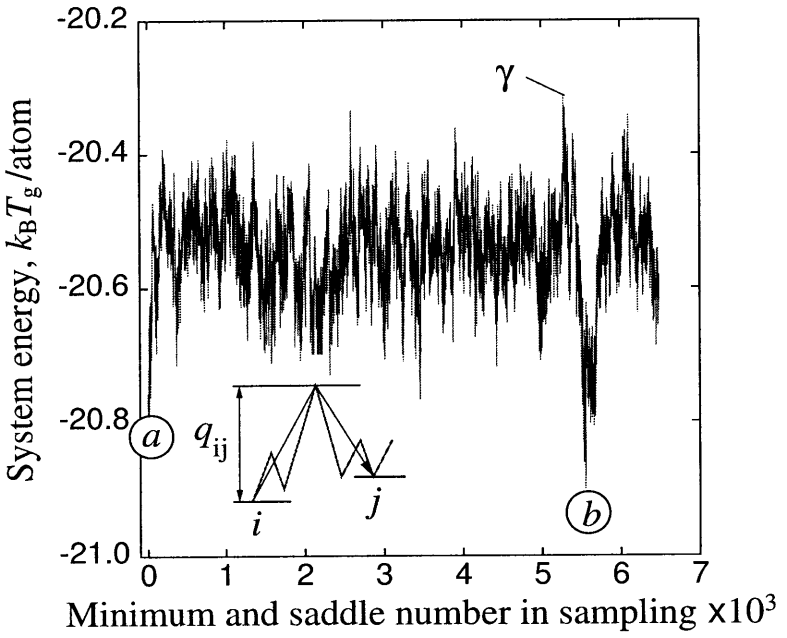

Figure 2-5: Trajectory generated from Autonomous Basin Climbing (ABC) for the case of a glassy system at $T_g = 0.37$. q_{ij} is the activation barrier between basins i and j [12].

By repeating this process we generate a trajectory of minima and saddle points through the energy landscape $\Gamma(E_{min}, E_{sad}) \equiv (E_{min}^{(1)}, E_{sad}^{(1)}, E_{min}^{(2)}, E_{sad}^{(2)}, ...)$. A sample calculation in the case of supercooled liquids is shown in Figure 2.5. Since the Gaussian penalty functions are preserved even after a new minimum is found frequent recrossing of small barriers is eliminated so the system proceeds efficiently in rough landscapes in which methods such as KMC perform poorly. However, the requirement of preserving the full penalty function history puts important constraints on memory and leads to potentially poor scaling of the method with system size (and correspondingly Gaussian penalty dimensionality). Nonetheless, in systems in which

particles are effectively confined to their local atomic positions (e.g. solid crystals, glasses, and sluggish colloidal suspensions) the volume of configuration space which must be samples is much smaller than the full phase space (as shown in Appendix B) and hence the method scaling with size improves.

By following the system evolution with ABC we can sample the topology of the landscape which in turn provides kinetic information via TST. Unlike methods such as nudged elastic band (NEB) [32] or the dimer method [29] no final state or direction of search for the pathways is necessary, so ABC is not constrained in regards to the possible kinetic mechanism which it explores. In addition to the energy landscape information which it generates, ABC also produces the local equilibrium configurations at the sampled basins so the microstructural evolution of the system can be directly tracked without the need for an additional method. In this manner the trajectories generated by ABC can be directly compared to those from time-driven methods such as MD. The only caveat to this approach is that, by design, ABC simulates a microcanonical ensemble (in which the variable of interest is the potential energy). However, and unlike in MD simulations of the microcanonical ensemble, the concept of time, which is not explicitly present in the relationship between the energy landscape and the configurational space (as highlighted in Section 2.1) is absent. Thus, the system evolves through the energy landscape by jumping from basin to basin in "metasteps" which, in principle, are artificial. Addressing this problem and extending ABC to more general systems (constant temperature, constant stress, dynamic energy landscapes) is the main methodological contribution of this thesis and is discussed in the next sections.

2.3.1 Canonical Ensemble ABC

The lack of a time coordinate in ABC can be addressed in two possible ways: (1) by relating "metasteps" to real time via TST, or (2) by coupling ABC with KMC. Each of these solutions has advantages depending on the problem of interest and are discussed more extensively subsequently. It is important to note that these methods effectively switch the ensemble from which the microstate is sampled from the micro-

canonical (constant E_{tot}) to the canonical (constant T) ensemble since the concept of time evolution is inherently linked to the velocities of the evolving particles and hence to their temperature. While this has no effect on thermodynamic variables (i.e. first-order derivatives of thermodynamic potentials such as T, P, t_{ij}, etc.) as long as the system size is sufficiently large, it does change the static susceptibilities (i.e. second order derivatives). Nonetheless, the canonical ensemble is a more accurate representation of most experimentally realizable physical systems than the microcanonical one, so this switch is beneficial for the predictive ability of the method.

The first approach is a straightforward application of the principles of TST to the energy landscape sampled by ABC. It involves adding two extra steps to the standard ABC methodology after a saddle point is found. As before consider the initial configuration $\mathbf{Q}_{min}^{(1)}$ with corresponding energy $E_{min}^{(1)} = \Phi(\mathbf{Q}_{min}^{(1)})$ which then transitions to a different basis with configuration $\mathbf{Q}_{min}^{(2)}$ and energy $E_{min}^{(2)} = \Phi(\mathbf{Q}_{min}^{(2)})$. These two distinct local minima in the energy landscape are then separated by a saddle point with configuration $\mathbf{Q}_{sad}^{(12)}$ with energy $E_{sad}^{(12)}$, all of which are given by the standard ABC approach. Now letting $A = \mathbf{Q}_{min}^{(1)}$, $B = \mathbf{Q}_{min}^{(2)}$, and $S = \mathbf{Q}_{sad}^{(12)}$ we have an identical configuration to that illustrated in Figure 2.1. with:

$$\Delta E_{ab} = \Phi(\mathbf{Q}_{sad}^{(12)}) - \Phi(\mathbf{Q}_{min}^{(1)}) \tag{2.30}$$

$$\Delta E_{ba} = \Phi(\mathbf{Q}_{sad}^{(12)}) - \Phi(\mathbf{Q}_{min}^{(2)}) \tag{2.31}$$

which are analogous to Equations (2.7-2.8). We can then calculate the rate for this transition from Equation (2.15), where we can either use a phenomenological estimate for ν_{ab} or we can calculate it using HTST by obtaining the normal frequencies around A and S as described in Section 2.1.1. and summarized in Equation (2.20) We then obtain the time step τ for the transition stochastically by:

$$\tau = -\frac{1}{\Gamma_{ab}} \ln(\zeta) = -\frac{e^{\frac{\Delta E_{ab}}{kT}}}{\nu_{ab}} \ln(\zeta) \tag{2.32}$$

where ζ is a random number between 0 and 1, and T is the system temperature

(which was a variable absent from the ABC simulations except in the generation of the inherent structures). The simulation time is then advanced by τ, the configuration switches from $\mathbf{Q}_{min}^{(1)}$ to $\mathbf{Q}_{min}^{(1)}$ and the process is repeated. Equation (2.32) then relates the length of the "metasteps" to the underlying landscape by assuming Poisson statistics and TST. In this fashion we can follow the trajectory $\Gamma(E_{min}, E_{sad})$ with a corresponding time coordinate associated to a specific temperature T. That is, our trajectory becomes $\Gamma(E_{min}(t), E_{sad}(t))$.

The second approach, which we term *hybrid ABC-KMC*, uses ABC to address the two flaws that limit the effectiveness of KMC that were described in Section 2.2.2. In a static case, i.e. to calculate equilibrium properties, the landscape generated by ABC (Figure 2.5) can be used to generate the canonical probability distribution $p(\mathbf{Q}) = \exp(-\beta\Phi(\mathbf{Q}))$ such that the probability of basin i with corresponding configuration $Q_{min}^{(i)}$ is given by:

$$p(i) = \exp(-\beta E_{min}^{(i)}) \tag{2.33}$$

where $\beta = 1/kT$. Then sampling over this distribution with a standard Metropolis algorithm produces the necessary configurations and averages. In the dynamical setting, the need for *a priori* possible escape pathways and rates is one of the main limiting factors for KMC. However the landscape produced by ABC naturally generates escape pathways and activation energy barriers for each of the basins. In particular, each local equilibrium configuration $\mathbf{Q}_{min}^{(i)}$ represents a basin i in the energy landscape. Furthermore the ABC method naturally orders these minima sequentially as it fills the landscape, such that configuration $\mathbf{Q}_{min}^{(j-1)}$ leads to configuration $\mathbf{Q}_{min}^{(j)}$ which in turn leads to configuration $\mathbf{Q}_{min}^{(j+1)}$. These transitions are separated by barriers given by:

$$\Delta E_{j-1\to j} = \Phi(\mathbf{Q}_{sad}^{(j-1\to j)}) - \Phi(\mathbf{Q}_{min}^{(j-1)}) \tag{2.34}$$

$$\Delta E_{j\to j+1} = \Phi(\mathbf{Q}_{sad}^{(j\to j+1)}) - \Phi(\mathbf{Q}_{min}^{(j)}) \tag{2.35}$$

with corresponding rates calculated from TST. These escape pathways from each basin configuration and their corresponding rates can be coupled dynamically with

a KMC algorithm. First, a Markov chain can be formed with nodes at each basin and edges to only the nearest neighbors with probabilities given by the rates as described above. This Markov chain can then be sampled using the standard KMC algorithm. Furthermore, the first nearest neighbor network described above can be generalized to k nearest neighbors, in which a the appropriate saddle point between basin i and $i + l$ with $0 < l \leq k$ is given by the highest saddle point in the chain connecting the two as illustrated in Figure 2.5. The parameter k thus controls what is considered a possible unit step in the KMC simulation. This process can be performed dynamically by adding an ABC step to the BKL algorithm for KMC in a similar fashion to adaptive KMC methods [33]. Starting the KMC algorithm from a given initial configuration, neighboring local minima are sampled on-the-go with ABC (from various initial quenches to obtain appropriate statistics). Energy barriers and rates are then computed and the resulting escape pathways are sampled with the standard BKL algorithm. Unlike adaptive KMC, the post-escape states do not need to be specified and are explicitly found by ABC. While this hybrid method addresses the major flaw associated with KMC of *a priori* knowledge of escape mechanisms and pathways, on-the-go hybrid ABC-MC is very computationally intensive. Less rigorous alternatives such as using ABC to create the escape pathway lists for the essential basins prior to the KMC routine and then using the calculated rates as inputs are therefore preferred for most applications.

2.3.2 Constant Stress ABC

As is also the case MD simulations, in many instances we are interested in simulating systems under experimentally realizable conditions such as constant temperature or pressure. These ensembles (canonical or isobaric) can be sampled via MD by using the thermostats or barostats described in Section 2.2.1. In addition, the previous section described two distinct approaches to sample canonical ensembles using ABC. In this section we provide a new generalization of the method to the constant stress ensemble, of which the isobaric ensemble is a particular example.

A fully rigorous approach would consider the Gibbs potential energy given by:

$$\mathcal{G}(\mathbf{h}, \mathbf{S}) = \mathcal{F}(\mathbf{h}, \mathbf{S}) + PV \tag{2.36}$$

where $\mathbf{h}$ and $\mathbf{h}_0$ are the matrices defining the shapes of the unit cell at the given minimum and initial configuration respectively, $V = \det(\mathbf{h})$ and $V_0 = \det(\mathbf{h}_0)$ are the corresponding volumes, $\mathbf{S} = (\mathbf{s}_1, \mathbf{s}_2, ..., \mathbf{s}_N)$ with $\mathbf{s_i} = \mathbf{h}^{-1}\mathbf{q_i}$, and $\mathcal{F}$ is the Helmoltz free energy at fixed shape $\mathbf{h}$. We can then use ABC in this higher dimensional Gibbs energy landscape and follow the evolution of the system through its topology in a manner analogous to standard ABC. For the kinetics we then need to choose the "masses" corresponding to the $\mathbf{h}$ variables by calibrating in a way similar to that for the "mass of the piston" or "weight of the wall" in Parrinello-Rahman dynamics [25]. As is well known, the equilibrium properties of an ensemble are independent of particle masses, so these masses are irrelevant for determining the equilibria in the landscape but determine the time scaling of the kinetics. The problem with this theoretically rigorous approach is that it is very inefficient in practice, because of the disparities between the contributions of $\mathbf{Q}$ and $\mathbf{h}$ to the topology of the landscape. More precisely, the principal curvature of the Gibbs energy landscape corresponding to the $\mathbf{h}$ coordinates is much lower (i.e., the landscape is "flatter" in that direction) than the principal curvature corresponding to the $\mathbf{S}$ coordinates. Therefore the size of any given basin increases in the $\mathbf{h}$ directions and a much larger number of Gaussian penalty functions is necessary to escape from it. As a result the efficiency of position relaxation is compromised by the cell shape relaxation.[2] Hence, in practice, we use a step-wise process to perform constant stress ABC simulations. That is, the cell shape relaxation takes place (almost) independently from that of the atomic positions. While this rigorously insures the local minima are found (because iterations of the relaxation in separate coordinates will lead to the local minima of the full Gibbs potential energy of Equation (2.36), especially if the principal curvatures are very

[2]We can, in principle, address the inefficiency of the rigorous method in filling the basins, resulting from the $\mathbf{h}$ coordinates, by penalizing each dimension with a different σ or by moving away from Gaussian penalty functions altogether. Optimizing the choice of the function for a particular landscape geometry remains an open question in the development of ABC.

dinerent), the calculated activation energy barriers separating the basins in the $3N+6$-dimensional landscape ($3N$ atomic degrees of freedom and 6 cell shape degrees of freedom) may overestimate the minimum barriers necessary to transfer basins, as will be discussed below. This step-wise constant stress ABC can be accomplished in three different ways that are illustrated in Figure 2.6. The choice of the specific methodology depends on the nature of the system and the computational constraints.

The first method (Figure 2.6.a) consists of the addition of a cell relaxation step (e.g., through the insertion of Parrinello-Rahman dynamics, described in Section 2.2.1) during the minimization procedure that follows a jump to a new basin. In this algorithm a fixed shape is chosen and standard ABC (with a constant cell shape $\mathbf{h}$) is performed until a new minimum (and saddle point) are found. Gaussian penalties are imposed on fractional, rather than cartesian, coordinates such that:

$$\phi_i(\mathbf{S}) = W \exp(-\frac{(\mathbf{hS} - \mathbf{hS}_{min}^{(i)})^2}{2(\sigma(\frac{V}{V_0})^{1/3})^2}) \tag{2.37}$$

After the new local minimum configuration is found, the cell shape is relaxed and particle positions are allowed to converge to a new minimum. This cell relaxation can take place at $T = 0$ as in standard minimization or at a non-zero finite temperature [3]. After a local equilibrium cell shape is found and the stress tensor $\mathbf{p}$ is sufficiently averaged, we can once again quench the atomic configuration with a fixed shape, additional Gaussian penalties are added to the potential energy landscape, and the evolution is continued. This method is best used when the slow step is the relaxation of atomic positions at a given volume, but the volume relaxation itself does not involve a high activation energy barrier. This is the case in highly disordered and frustrated structures such those that form during high dose rate irradiation swelling and are explored in Chapter 4. The need to penalize in fractional coordinates and to maintain the Gaussian penalties even after the cell is relaxed results from the fact that the energy barriers that must be overcome to change the cell shape are small. This implies that the system can return to an already visited basin via a slightly different

[3] If the cell relaxation step takes place at $T = 0$ a fictitious stress must be introduced to account for the thermal stresses of the constant T MD simulation.

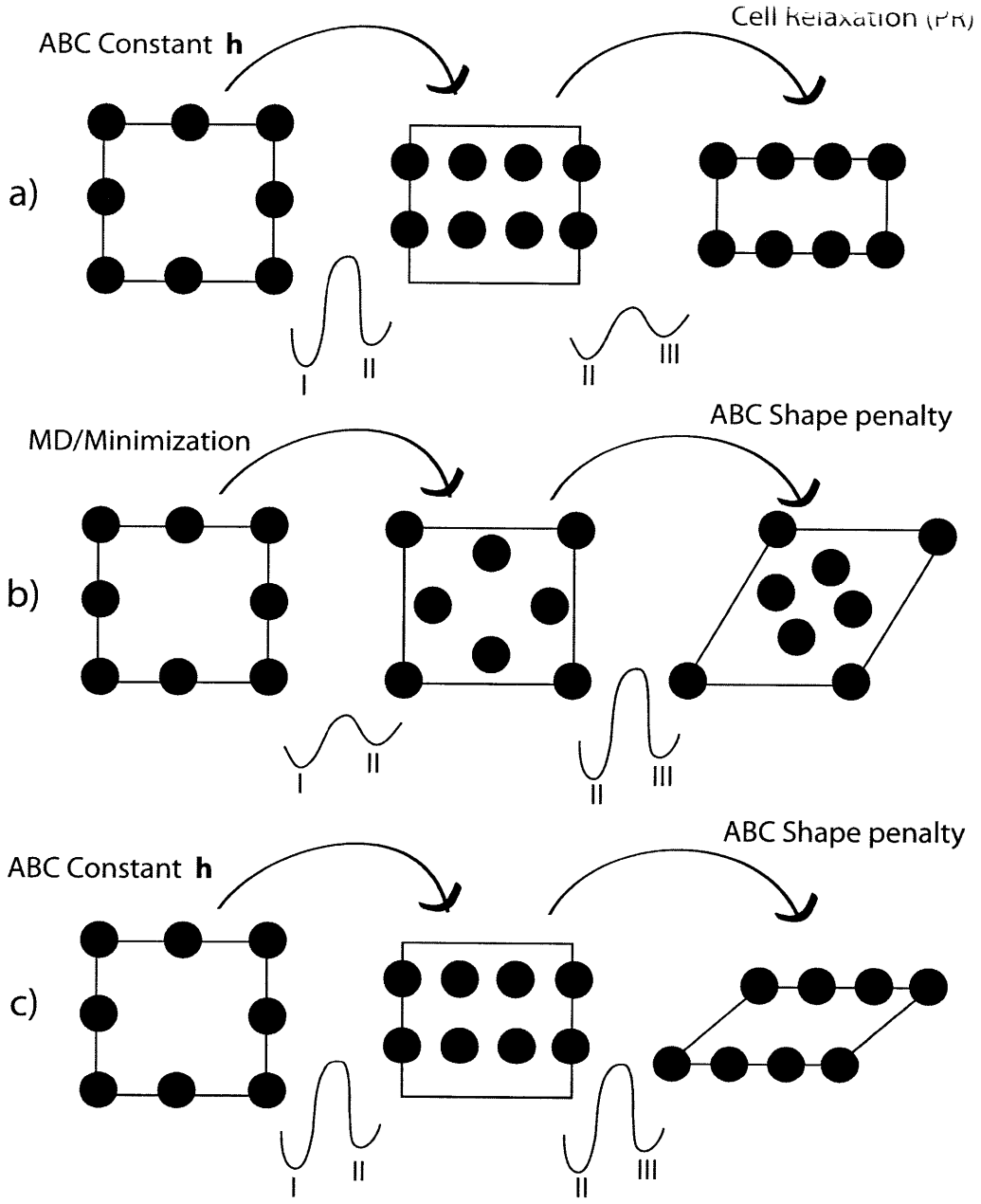

Figure 2-6: Three methods for performing constant stress Autonomous Basin Climbing (ABC): (a) ABC on the potential energy landscape plus a cell relaxation step, (b) Minimization plus ABC on the Gibbs energy surface, (c) ABC on both the potential and Gibbs energy surfaces. The insets illustrate the relative activation energy barriers for each of the steps in the algorithm as well as the corresponding microstructural changes.

chain of shape changes if the Gaussians are removed which would greatly reduce the efficiency of the algorithm. We adjust the parameters of the penalty function dynamically since the size of phase space sampled is volume-dependent and each given basin grows with the cell volume. Appendix D shows some results benchmarking this method.

The second method (Figure 2.6.b) involves MD equilibration of the atomic positions for a fixed cell shape $\mathbf{h}$ (at constant stress and temperature) until the stress tensor $\mathbf{p}$ is sufficiently averaged. Then the ABC method is applied directly to the cell shape in a manner analogous to the metadynamics described by Martonák, Laio, and Parrinello [34]. In this case, the penalty functions are added to a 6-dimensional Gibbs potential surface given by fixing the fractional atomic positions in Equation (2.36):

$$\mathcal{G}(\mathbf{h}) = \mathcal{F}(\mathbf{h}) + PV \tag{2.38}$$

with derivative:

$$-\frac{\partial \mathcal{G}}{\partial h_{ij}} = V(((\mathbf{p} - P)\mathbf{h}^{-1})_{ij} + ((\mathbf{p} - P)\mathbf{h}^{-1})_{ji})(1 - \frac{1}{2}\delta_{ij}) \tag{2.39}$$

and penalty functions:

$$\phi_i = We^{-|\mathbf{h}-\mathbf{h}^{t'}|^2/2(\delta h)^2} \tag{2.40}$$

where $\mathbf{h}^{t'}$ denotes the shape corresponding to the last visited basin, δh is equivalent to σ in the standard ABC formulation and determines the resolution. Finally the cell shape evolves according to:

$$\mathbf{h}^{t+1} = \mathbf{h}^t + \delta h \frac{F_p^t}{|F_p^t|} \tag{2.41}$$

where $F_p^t = \mathbf{F} + \mathbf{F}_g = -\frac{\partial \mathcal{G}}{\partial \mathbf{h}} + \mathbf{F}_g$, where $\mathbf{F}_g$ is the artificial force resulting from the superposition of Gaussians. After finding a new shape the particle atomic positions are rescaled to fit in the new box by taking $\mathbf{q}_{t+1} = \mathbf{h}_{t+1}\mathbf{s}_t = \mathbf{h}_{t+1}\mathbf{h}_t^{-1}\mathbf{q}_t$ This method is most effective when the cell shape relaxation is much slower than the relaxation of the atomic positions at a given cell shape, e.g. in the case of first-order phase transitions. This approach has been benchmarked in by Martonák et al [34] for the

phase transition of diamond into graphite.

The third method can be interpreted as a combination of the previous two and is included for completeness. In this case we combine a constant $\mathbf{h}$ step for atomic relaxations with a "cell" ABC step in the Gibbs potential for the shape relaxation. As a result this approach is extremely computationally intensive and only necessary when the barriers that need to be overcome are very high in both steps. We do not explore this method in this thesis and, to our knowledge, no calculation using this combined approach has been reported in the literature. A potential application of interest would be the evolution of irradiated materials in the neighborhood of a phase transition, such as in the self-organization of ion beam implanted substrates.

An important issue, shared with constant $\mathbf{h}$ ABC, is that there is no obvious connection between the metasteps, in which the systems traverse the energy landscape in all four of these methods (three step-wise, one theoretically rigorous), and physical time. For the first method the dynamics of the cell relaxation step at a non-zero temperature T are physical and have a proper time coordinate associated to them. We can then use TST to calculate time scales for the transitions in the ABC step, as described in Section 2.3.1., and provide the whole trajectory with a time coordinate, i.e. $(\mathbf{S}_{min}(t), \mathbf{h}_{min}(t), \mathbf{S}_{sad}(t), \mathbf{h}_{sad}(t))$. However, the decoupling of the coordinates implies that the ABC relaxation takes place under a lower number of degrees of freedom than an equivalent MD simulation with a barostat would, and as a result the calculated energy barriers would be overestimates of the real barriers (with the error depending on the relative principal curvatures of the landscape) but a closer approximation that those from a constant $\mathbf{h}$ simulation.

Including the time variable in the other three methods is more difficult. In this case the barriers in the Gibbs potential energy landscapes of Equations (2.36) and (2.38) cannot be interpreted within the context of TST in a straightforward matter because the concept of temperature for shape relaxation is not well defined. However based on the Parrinello-Rahman Lagrangian of Equation (2.26) we propose a *cell shape temperature* $T_{\mathbf{h}}$ as:

$$T_{\mathbf{h}} = \frac{1}{9k} W_{piston} Tr\dot{\mathbf{h}}'\dot{\mathbf{h}} \tag{2.42}$$

and

$$T_{tot} = \frac{2}{3(N+3)k}(\frac{1}{2}\sum_{i=1}^{N} m_i \dot{\mathbf{s}}_\mathbf{i}' \mathbf{G} \dot{\mathbf{s}}_\mathbf{i} + \frac{1}{2} W_{piston} Tr \dot{\mathbf{h}}' \dot{\mathbf{h}}) = \frac{N}{N+3} T + \frac{3}{N+3} T_\mathbf{h} \quad (2.43)$$

From which we can calculate transition rates from the Gibbs potential energy landscapes by:

$$\Gamma = \nu e^{-\frac{\Delta \mathcal{G}}{kT_\mathbf{h}}} \quad (2.44)$$

in the case of Equation (2.38) (and methods 2 and 3), and:

$$\Gamma = \nu e^{-\frac{\Delta \mathcal{G}}{kT_{tot}}} \quad (2.45)$$

for the more general Gibbs surface of Equation (2.36) and of the theoretically rigorous approach. We conjecture that the parameter W associated with the weight of the wall can be calibrated against specific well know relaxation times and then used to calculate the physical time corresponding to the processes, though this has not yet been benchmarked.

2.4 Autonomous Basin Climbing - Dynamic

The energy landscapes constructed from the ABC method provide a mechanism to describe the slow dynamics of a variety of systems via TST. In addition, the generalization to constant temperature and constant stress provide additional ways of comparing the systems dynamics to those realizable in physical systems beyond those in the NVE microcanonical ensemble. [4] Nonetheless, despite its power, ABC is, at its core, a static method. Regardless of the ensemble defining the macrostates, the (potential) energy surface through which they traverse is fixed in time. As highlighted in Section 2.1. this lack of an explicit time dependence in the potential allowed us

[4] Even the constraint of a fixed number of particles could, in principle, be relaxed to a grand-canonical formulation by considering the number of particles of each atomic species $\mathbf{N} = (N_A, N_B, ...)$ macrostate variables, and then sampling a generalized Gibbs free energy given by $\mathcal{G}(\mathbf{S}, \mathbf{h}, \mathbf{N}) = \mathcal{F}(\mathbf{S}, \mathbf{h}, \mathbf{N}) + PV + \sum_{species} N_k \mu_k$ for fixed chemical potentials $\mu_A, \mu_B, ...$

to associate an individual configuration or microstate with a specific energy in the landscape regardless of the time coordinate. This allowed us to connect the topology of the landscape to the time evolution of the system via TST.

However, for many problems of interest the landscape itself is either explicitly or effectively time dependent. We can write Equation (2.4) (or the equivalent free energy that defines the landscape) as:

$$E_{potential} = \Phi(t, \mu) = \Phi(t, \mathbf{q_1}, ..., \mathbf{q_N}) \tag{2.46}$$

This is the case if, for example we have an external time dependent force. This can be an electric field or a strain rate, or a change in the number of particles in the system as a function of time in a predefined fashion and not as a result of bringing the system in contact with an equilibrium particle reservoir as is the case for the grand-canonical ensemble. Alternatively, the interactions between the particles themselves could be time dependent leading to an obvious time dependence in the energy landscape. In this section we introduce the latest generalization of the ABC method to dynamic energy landscapes.

In order to apply ABC to these systems we need to generalize our static formalism to accommodate dynamic energy landscapes. We denote this new method: Autonomous Basin Climbing - Dynamic or ABCD. There is an important assumption that we make in ABCD: that the rate of change of the energy landscape due to its explicit (or effective) time dependence is much slower than the atomic fluctuations near a local equilibrium. More precisely:

$$|\frac{\partial \Phi}{\partial t}| << |\frac{\partial \Phi}{\partial \mathbf{Q}}| \tag{2.47}$$

This assumption, while essential, is not a major constraint in practice, since it only implies that the atoms need to have time to respond to the changes in the interactions or external fields which is generally the case for the slowly evolving systems for which ABCD is used.

We then note that, even though the standard ABC model samples the full land-

scape, the transition rate out of a specific basin is determined only by the *local* topology of the energy landscape. Therefore, and from assumption (2.47), we can approximate (to first order in the changes in the energy landscape) the local energy landscape that a macrostate traverses through in a short period of time as fixed. ABCD then consists on performing ABC on the fixed local energy landscape, extract information on the kinetics of the evolution of the microstate, adjust the landscape accordingly, and then repeat the process. As such, ABCD can be considered a local perturbative approach to traversing a dynamic landscape.

The ABCD algorithm proceeds as follows: As in ABC, consider an initial microstate that is relaxed to a local minima in the energy landscape at time t, with spatial configuration $\mathbf{Q}_{min}^{(t)}$ with corresponding energy $E_{min}^{(t)}$. Following the standard ABC algorithm (Section 2.3) we generate a new local minima with configuration $\mathbf{Q}_{min}^{(t')}$ with potential energy $E_{min}^{(t')}$ and a saddle point configuration $\mathbf{Q}_{sad}^{(t\to t')}$ with potential energy $E_{sad}^{(t\to t')}$. From this we can calculate an activation energy barrier and associated transition rate from TST as:

$$\Delta E = E_{sad}^{(t\to t')} - E_{min}^{(t)} \tag{2.48}$$

$$\Gamma = \nu(\mathbf{Q}_{min}^{(t)}, \mathbf{Q}_{sad}^{(t\to t')}) \exp(-\frac{\Delta E}{kT}) = \nu(\mathbf{Q}_{min}^{(t)}, \mathbf{Q}_{sad}^{(t\to t')}) \exp(-\frac{E_{sad}^{(t\to t')} - E_{min}^{(t)}}{kT}) \tag{2.49}$$

from which we can calculate the corresponding time step as described in Section (2.3.1):

$$\delta t = -\frac{1}{\Gamma} \ln(\zeta) \tag{2.50}$$

where ζ is a random number between 0 and 1. We can then move the system to configuration $\mathbf{Q}_{min}^{(t')}$, and adjust the energy landscape by:

$$\Phi^{t+\delta t}(\mathbf{Q}) = \Phi(t + \delta t, \mathbf{Q}) \tag{2.51}$$

We then relax the macrostate according to this new landscape until we reach a new local minimum $\mathbf{Q}_{min}^{(t+\delta t)}$. We then consider the saddle point configuration $\mathbf{Q}_{sad}^{(t\to t+\delta t)} = \mathbf{Q}_{sad}^{(t\to t')}$ with saddle point energy $E_{sad}^{(t\to t+\delta t)} = \Phi^{t+\delta t}(\mathbf{Q}_{sad}^{(t\to t')})$. By assumption (2.85) this

relaxation takes place much more rapidly than the rate of change of the landscape, so we can consider this new local minimum and saddle points to be the correct local minimum and saddle point in the new landscape. We then remove the previous Gaussian penalty functions and repeat the process. Benchmarking for the model is summarized in Appendix E for the case of a material under ion irradiation.

As is clear from the algorithm, the slower the landscape changes, the more accurate our approach becomes. In particular, the equality $E_{sad}^{(t\to t+\delta t)} = \Phi^{t+\delta t}(\mathbf{Q}_{sad}^{(t\to t')})$ has an error given, to first order, by:

$$\delta E_{sad}^{(t\to t+\delta t)} = \frac{\partial \Phi^t}{\partial t}(\mathbf{Q}_{sad}^{(t\to t')})\delta t \tag{2.52}$$

so the method is accurate as long as:

$$|\frac{\partial \Phi^t}{\partial t}(\mathbf{Q}_{sad}^{(t\to t')})|\delta t << |\mathbf{Q}_{sad}^{(t\to t')}| \tag{2.53}$$

$$\Rightarrow \delta t << |\mathbf{Q}_{sad}^{(t\to t')}(\frac{\partial \Phi^t}{\partial t}(\mathbf{Q}_{sad}^{(t\to t')}))^{-1}| \tag{2.54}$$

and therefore the slower the rate of change of the landscape the more accurate our estimate of the saddle point energy with ABCD becomes. In addition, δt is dependent on the height of the energy barrier found during the ABC step. Therefore, reducing σ in the Gaussian penalties, and thus increasing the resolution of what we consider two separate local minima results in a larger number of intermediate transition steps and in turn reduces δt, also increasing ABCD's accuracy, at the cost of computational efficiency. Therefore the parameter σ can be tuned to improve not only the accuracy of the ABC calculation but also that of the ABCD calculation as a whole. Furthermore, as the landscape is dynamic the parameters σ and W optimally chosen for the initial sampling may not be appropriate any longer and should be adjusted dynamically to enhance the performance and accuracy of the algorithm.

The removal of the penalty functions after a transition could reduce the efficiency of the method, especially if the changes in the landscape are very small in the long run, and the system continues to return to previously visited configurations, so one

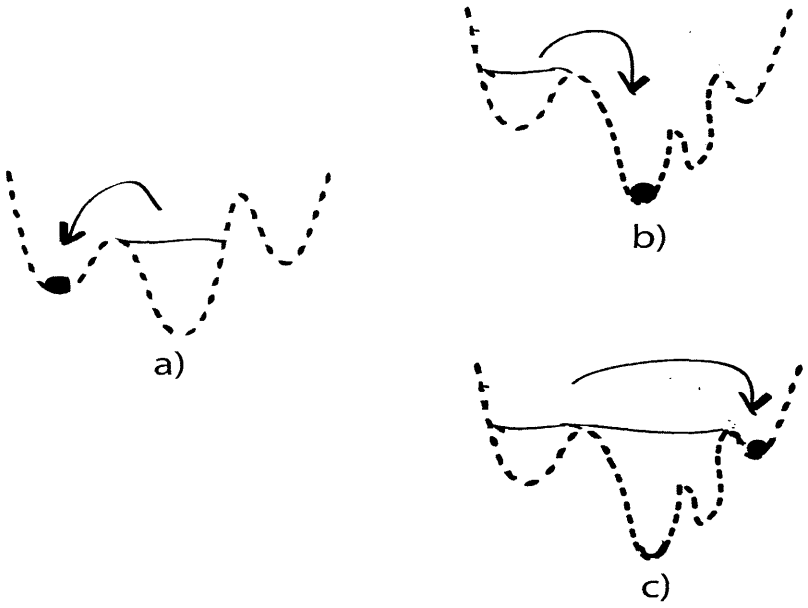

Figure 2-7: Schematic illustration explaining the effects of maintaining Gaussian penalties in ABCD. a) A new minimum is found during the ABC step and the energy landscape changes. b) With the Gaussian penalties removed the system can go to a newly formed energy minimum nearby the former old configuration, which is correct physically. c) Without removing the Gaussian penalties the newly formed minima are not sampled.

can opt to keep the Gaussian penalties. However, dramatic changes in the energy landscape in the long run could give rise to new basins which were non-existent at the beginning of the simulation (see Figure 2.8). Therefore maintaining the Gaussian penalty functions could limit the accuracy of the method.

2.4.1 Time Dependent Number of Particles: N=N(t)

A particular example of a changing energy landscape results from a systematic change in the number of particles. This in turn modifies the dimensionality of the system as a function of time, so the local topology is altered. While the changes in the number of particles are discrete, as long as Equation (2.54) holds, the changes to the local topology with respect to the "old" atomic positions are small. This is the case if, for

example, $N(t) >> \delta N$ at all times and the particles are introduced (or removed) very slowly. It must be noted that a systematic $N = N(t)$ is not the same as taking the system to a grand-canonical formulation because even though N varies, it is not an endogenous variable which fluctuates due to a fixed chemical potential μ.

In this case, we can proceed as described in the previous section by inserting or removing particles according to $N = N(t)$ as the system evolves in time. This dynamic condition is of particular use for the problem of materials irradiated with ions, in which the number of interacting particles increases after each implantation (discussed in Chapter 4) or in the growth of materials such as films or tubes by deposition.

2.4.2 Time Dependent Simulation Cell Shape: h=h(t)

Another case of interest is one where the shape of the simulation cell changes as a function of time due to an exogenous mechanism, for example due to an imposed linear or sinusoidal shear strain. This is different from the natural fluctuations that take place in a constant stress ensemble in which the cell shape is an endogenous variable so our constant stress ABC formulation is unable to handle it.

In this instance, the simulation shape can be fixed according to $\mathbf{h} = \mathbf{h}(t)$ and ABCD can be used to traverse the changing landscape with the simulation cell shape adjusting in between transitions. For example, in the case of a constant strain rate $\dot{\gamma}$ (we can assume that it is in the x-direction without loss of generality), the shape of the cell can be adjusted after a transition with associated time step δt as follows:

$$\mathbf{h}(t + \delta t) = \mathbf{h}(t) + L\dot{\gamma}\delta t\mathbf{A}_{\mathbf{x}} \tag{2.55}$$

where $\mathbf{A}_{\mathbf{x}}=\begin{pmatrix} 0 & 0 & 1 \\ 0 & 0 & 0 \\ 0 & 0 & 0 \end{pmatrix}$. This can be generalized to more complex strain rate conditions or other possible time-dependent changes in the shape of the simulation unit cell as long as they occur slowly enough.

Applications

Chapter 3

Hydrogen Embrittlement of Metals

This chapter (up to Section 3.1) includes work that has been published in part in the Physical Review Letters [35].

The effects of hydrogen on the properties of materials have been studied both theoretically and experimentally for many decades. Under hydrogen-rich conditions metallic alloys exhibit a variety of fundamental phenomena. These include large volume contractions in body-centered cubic (bcc) α-Fe [36, 37], enhancement of diffusion at metal-metal junctions [38], and degradation of the mechanical properties in the form of hydrogen-induced embrittlement in a variety of metallic alloys.

The problem of hydrogen embrittlement in metals serves as a first application of the methodology developed in Chapter 2 for the analysis of rough energy landscapes in defected condensed matter. As detailed below, the embrittling effect of hydrogen results from complex interactions between hydrogen impurities and the underlying defective microstructure of the material. Hence, in addition to its technological and scientific importance, the problem of hydrogen embrittlement in metals introduces the first level of microstructural complexity in the study of rough energy landscapes: the presence of multiple interacting defects in an otherwise perfect crystalline lattice.

Moreover, as a consequence of the interactions between point defects (such as hydrogen impurities and free vacancies) and extended defects (such as dislocations and grain boundaries) the problem of hydrogen embrittlement is characterized by a

complex coupling between structural and chemical effects. This coupling results in rich physical phenomena comprising multiple length, energy, and time scales as the system traverses a rough underlying energy landscape.

The literature focused on the topic of hydrogen embrittlement is vast and encompasses large contributions on energy related technology [39], hydrogen in metals [40–42], and corrosion [43, 44] among others. Of particular industrial importance is the embrittlement of hardened steels (Fe-C alloys) such as those used for bearings, in which the operating conditions are such that pickup of atomic hydrogen from the environment or the hydrocarbons used for lubrication is unavoidable. At least two potential plasticity mechanisms have been proposed to explain the experimental evidence of embrittlement in those steels: the hydrogen enhanced localized plasticity (HELP) mechanism [45–47] and a mechanism of stress relaxation induced by hydrogen-enhanced vacancy populations [37, 48–52].

Both of these mechanisms, and a large portion of the experimental and theoretical literatures suggest that these hydrogen-mediated effects are a consequence of the strong interaction between hydrogen impurities and other point defects in the material. Furthermore, the delayed fracture and creep characteristic of hydrogen embrittlement are at their root deeply connected with the slow relaxation of the alloy microstructure under the influence of the hydrogen impurities.

A complete understanding of the embrittlement phenomena therefore requires a thorough analysis of both the equilibrium distributions of point defect clusters (PDCs) in the material, which determine the type of species and interactions that are of concern under different environmental conditions, as well as the kinetics of diffusion and relaxation of the complex hydrogen-containing microstructure. This chapter addresses both questions within a multiscale modeling methodology based on electronic structure density function theory (DFT) calculations coupled with statistical mechanics and transition state theory tools to describe both equilibrium and dynamical properties.

5.1 Point Defect Cluster Populations

This section discusses the first and most fundamental of the issues posed above: the formation, binding, and concentrations of point defect cluster species in bcc Fe-C alloys containing hydrogen [35]. Our approach relies on the use of density functional theory calculations for the energetics, coupled with a free- energy functional to determine the PDC concentrations as a function of total hydrogen and vacancy concentrations.

The total energy DFT calculations were performed using the VASP code [53] with Blöchl's projector augmented method [54]. Calculations were carried out with a plane-wave energy cutoff of 400 eV in 128-atom super-cells with the theoretical lattice constant of 2.835 $\AA$, using a 2x2x2 k-point mesh for integration over the Brillouin zone and a Methfessel Paxton Fermi-surface smearing parameter of 0.05 eV [55]. Calculations included spin polarization effects and assumed an initial ferromagnetic charge density consistent with the bcc ferritic Fe phase. No symmetry constraints were imposed. The geometric relaxation was terminated with a force cutoff of 5 $meV/\AA$. Vibrational frequency calculations were performed in 54-atom super-cells with the same k-point mesh. All results are reported at a benchmark temperature of 160°C, representative of the tempering temperatures for carbon-rich bcc Fe-C alloys.

The strong interactions between defects in the crystalline microstructure result in a rough total free energy landscape for individual PDCs, in this case as a function of their geometrical configuration. Numerous shallow local energy minima exist near the optimized geometry for any given PDC stoichiometry, and hence the use of straightforward energy minimization procedures is limited. This results in an error for the binding energies of approximately 0.1 eV, implying an error in the magnitude of the defect cluster concentrations of, at most, 2 orders of magnitude at 160°C. However, as shown subsequently, conclusions regarding the dominant PDC types as a function of alloy composition are not modified by this level of uncertainty and the results presented in this chapter are sufficiently robust for predictions.

Calculations are performed with a constrained grand canonical free-energy func-

tional, similar to presented for the bcc Fe-C binary alloy [56], in order to account for the variable concentrations of PDC in the system and obtain a unique solution for the species distributions. Specifically, the formation energy of each PDC in a closed Fe-C-H system is given by:

$$E^D_{form}(T, \mu_{Fe}, \mu_H, \mu_C) = E^D(T) - E^0(T) - \mu_{Fe}\Delta n_{Fe} - \mu_C \Delta n_C - \mu_H \Delta n_H$$

where $E^D(T)$ and $E^0(T)$ are the DFT-calculated free energies (only including vibrational entropy) for the PDC-containing and perfect super-cells respectively, μ_X is the chemical potential of element X, and Δn_X is difference in the number of atoms of element X in the two cells. Vibrational contributions to the free energy are obtained by approximating the atoms as 3D harmonic oscillators with DFT-calculated frequencies. The binding energy for point defect cluster D comprising n_{Va} vacancies, n_C carbon atoms, and n_H hydrogen atoms relative to the elementary defects (free vacancies, octahedral carbon, and tetrahedral hydrogen interstitials) is then computed by:

$$E_{binding}(T) = n_{Va}E^{Va}_{form}(T) + n_C E^C_{form}(T) + n_H E^H_{form}(T) - E^D_{form}(T) \qquad (3.1)$$

where $E^D_{form}(T)$ is defined in (3.1), and here normalized by corresponding chemical potentials, and $E^{Va}_{form}(T)$, $E^C_{form}(T)$, and $E^H_{form}(T)$ are the formation energies for free vacancies, octahedral carbon and tetrahedral hydrogen interstitials, respectively.

Binding energies at 0 K and 433 K (160°C) for dominant PDCs are summarized in Table 3.1. At 0 K, the formation energy for a C octahedral interstitial is 0.86 eV lower than that for a C tetrahedral interstitial, consistent with experimental observations [57]. In contrast, hydrogen is more stable in a tetrahedral site, with a calculated formation energy 0.12 eV lower than that for an octahedral hydrogen site; also consistent with empirical data [58].

Equilibrium PDC concentrations are calculated by minimizing the Helmholtz free

Table 3.1: Binding free energies for different defect stoichiometries at 0 K and 433K (160°C). Only the deepest energy minimum for each point defect cluster (PDC) stoichiometry is shown. Experimental values are given in parentheses for comparison, where available.

PDC	$E_{binding}(eV)$	
	$T = 0K$	$T = 433K$
$H_{octahedral}$	-0.12 (-0.07 [57])	-0.18
$C_{tetrahedral}$	-0.86	-0.84
$Va_2\langle 100\rangle$	0.17	0.17
$Va_2\langle 111\rangle$	0.14	0.14
Va_1H_1	0.51 (0.46 [59])	0.61
$Va_2H_1\langle 100\rangle$	0.76	1.05
$Va_2H_1\langle 111\rangle$	0.70	0.77
$Va_2C_1\langle 100\rangle$	1.04	1.20
$Va_2C_1\langle 111\rangle$	0.79	0.86
C_1H_1	0.02(0.03 [59])	0.02
Va_1C_1	0.52(0.85 [57])	0.63
Va_1C_2	1.44	1.65
$Va_1C_1H_1$	1.14	1.31
$Va_1C_2H_1$	1.38	1.63
$Va_2C_1H_1\langle 100\rangle$	1.37	1.65
$Va_2C_1H_1\langle 111\rangle$	0.86	1.20
$Va_2C_2H_1\langle 100\rangle$	1.10	1.50
$Va_2C_2H_1\langle 111\rangle$	2.38	2.76
H_2	0.01(0.04 [59])	0.004
Va_1H_2	1.11	1.31
$Va_2H_2\langle 100\rangle$	1.22	1.65
$Va_2H_2\langle 111\rangle$	1.29	1.44
$Va_2C_2\langle 100\rangle$	1.81	2.01
$Va_2C_2\langle 111\rangle$	1.91	2.12
C_1H_2	-0.05	0.01
$Va_1C_1H_2$	0.92	1.19
$Va_2C_1H_2\langle 100\rangle$	1.77	2.16
$Va_2C_1H_2\langle 111\rangle$	1.31	1.65
Va_1H_3	1.38	0.82

energy of the system:

$$F(T, \mu_{Fe}, \mu_H, \mu_C) = \sum_i n_i E_{form}(T, \mu_{Fe}, \mu_H, \mu_C) - k_B T \sum_i \ln\left(\frac{(\alpha_i N)!}{(\alpha_i N - n_i)! n_i!}\right) \quad (3.2)$$

where the first term is described in (3.1) and the second term accounts for the configurational entropy of the system; k_B represents Boltzmann's constant and T the absolute temperature. Here, n_i is the total number of PDCs of type i, N is the total number of bcc lattice positions, and α_i is defined such that $\alpha_i N$ is the number of indistinguishable configurations in the lattice for the defect cluster i for large N. For example, for free vacancies $\alpha_i = 1$, because any bcc lattice site could serve as a possible Va site, while for a tetrahedral interstitial $\alpha_i = 6$ because there are six tetrahedral sites for each bcc lattice site. The entropic term in (3.3) counts the number of possible ways to rearrange the PDC in the crystalline lattice. Using Stirling's approximation we find that this entropic term is given by:

$$\ln(\frac{(\alpha_i N)!}{(\alpha_i N - n_i)! n_i!}) = \alpha_i N \ln(\alpha_i N) - (\alpha_i N - n_i) \ln(\alpha_i N - n_i) - n_i \ln n_i \tag{3.3}$$

and defining the defect concentration of a given PDC with respect to the bcc Fe lattice by $c_i = \frac{n_i}{N}$ equation (3.3) becomes:

$$\begin{aligned} \frac{F(T, \mu_{Fe}, \mu_H, \mu_C)}{N} &= \sum_i c_i E_{form}(T, \mu_{Fe}, \mu_H, \mu_C) \\ -k_B T \sum_i (\alpha_i \ln \alpha_i - (\alpha_i - c_i) \ln(\alpha_i - c_i) - c_i \ln c_i) & \end{aligned} \tag{3.4}$$

and then minimizing the free energy in (3.5) we find:

$$c_i = \frac{\alpha_i}{\exp(\frac{E_{form}(T, \mu_{Fe}, \mu_H, \mu_C)}{k_B T}) + 1} \tag{3.5}$$

The chemical potentials are related to the total concentrations of C, H, and Va by the following constraints:

$$Va_{tot} = \sum_{clusters} x[Va_x C_y H_z] \tag{3.6}$$

$$C_{tot} = \sum_{clusters} y[Va_x C_y H_z] \tag{3.7}$$

$$H_{tot} = \sum_{clusters} z[Va_x C_y H_z] \tag{3.8}$$

where $[Va_xC_yH_z]$ is the concentration of a particular PDC type calculated from (3.4) that comprises x iron vacancies, y carbon atoms, and z hydrogen atoms.

3.1.1 Point Defect Cluster Dominance Diagram

Figure 3.1 shows these results in a PDC dominance diagram. Boundaries are determined by changes in the most dominant PDC, dividing the diagram into nine distinct regions, each characterized by a single prevalent PDC. Statistically relevant, but non-dominant PDCs (defined in this study as PDCs with concentrations within two orders of magnitude of the most prevalent one), vary in concentration within a given zone and thus their precise concentration ranking is not reported. Figure 3.1 thus indicates which PDCs are of macroscopic importance for a given alloy composition and point defect concentration, providing a framework to delve into more detailed analysis of the microstructure. A full dominance representation ordinarily would require a three dimensional graph indicating the prevalent PDCs as a function of total C, H, and Va concentrations. However, since our interest lies primarily on the effects of hydrogen, we focus on the changes as a function of the $[H_{tot}]$ and $[Va_{tot}]$. Thus, although our methodology can generate the full diagram, the total carbon concentration is fixed to be that reported for high-carbon steels ($[C_{tot}] = 0.01$ in Figure 3.1) [56]. [1]

Most zones in the diagram, except for H_I and C_I, are dominated by Va-containing PDCs. Thus, the vacancy-mediated interactions are the primary factors that determine the PDC populations in the alloy, and the full complexity of the PDC spectrum can only be appreciated in the regime in which $[Va_{tot}]$ is significant. In the C- and H-regions of the diagram, these Va-containing PDCs exhibit concentrations many orders of magnitude higher than the free vacancies and di-vacancy clusters. Hence, consistent with previous studies [60], the presence of hydrogen is observed to stabilize free vacancies in bcc Fe, in the form of vacancy-solute clusters. In addition, for $[H_{tot}] >> [C_{tot}]$, and low $[Va_{tot}]$ (H_I zone), interstitial atomic hydrogen is prevalent

[1] Since the alloys of interest in this study are not exposed to radiation, the concentrations of Fe self-interstitials in the material are negligible and therefore ignored. However, our approach can also be generalized to include such point defects and their interaction with impurities and allow for the study of PDC formation and concentrations in irradiated alloys as well.

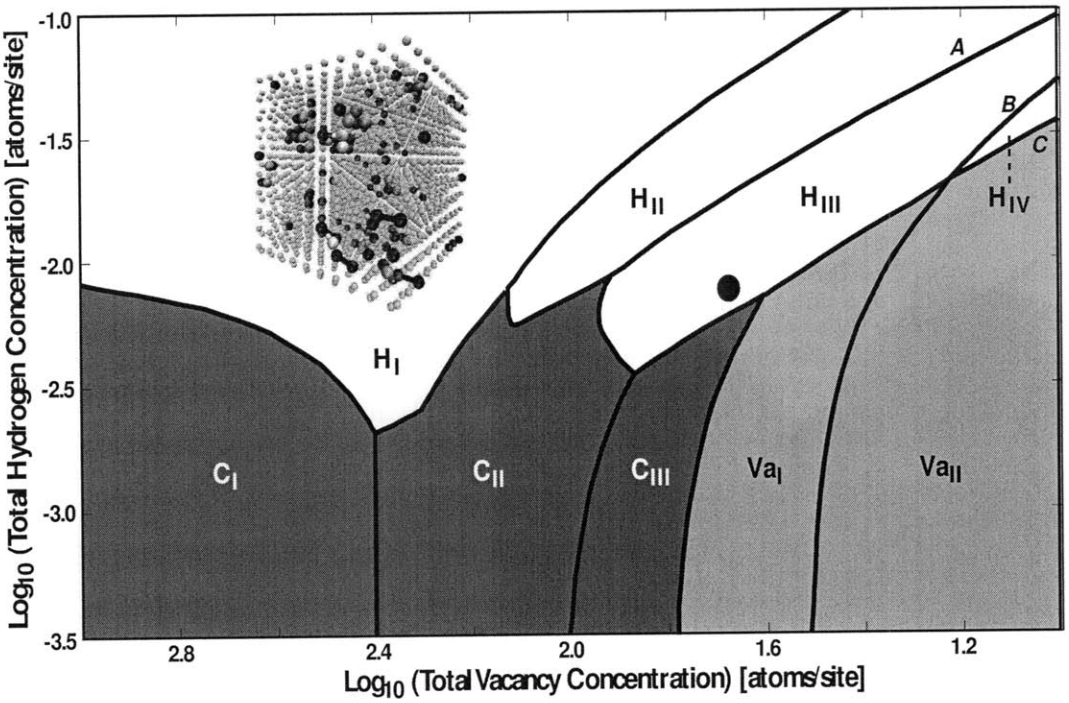

C_I	C_{oct},Va_2C_1,H_{tet}	H_I	H_{tet},Va_2C_1,C_{oct}
C_{II}	Va_2C_4,Va_2C_2,Va_1H_1, Va_1H_2, Va_{free}	H_{II}	Va_1H_2,Va_2C_4
C_{III}	Va_2C_2,Va_{free},Va_2C_4,Va_1H_1, Va_1H_2	H_{III}	Va_1H_1,Va_2C_4,Va_2C_2, Va_{free}
Va_I	Va_{free},Va_2	H_{IV}	Va_2H_1,Va_2,Va_1H_1, Va_{free}
Va_{II}	Va_2,Va_1H_1,Va_{free}		

Figure 3-1: Dominance diagram for PDCs in Fe-C-H alloys with $[C_{tot}] = 0.01$ (1.0 at. %).The PDC of highest concentration in each zone is indicated first, and other statistically relevant PDCs are listed. The A, B, and C boundaries in the high $[H_{tot}]$, high $[Va_{tot}]$ regime are also indicated. The inset shows a schematic of the defect population at the marked point. Vacancies (black), hydrogen (white), and carbon (gray) atoms bind in a background bcc Fe matrix (orange). Va_2 clusters are oriented along the $\langle 111 \rangle$ direction.

Table 3.2: Energy changes in binding reactions involving the Va_1C_1 and H_{tet} PDCs

Reaction	$\Delta E_{reaction}(eV)$
$Va_1C_1 + H_{tet} \rightarrow Va_1C_1H_1$	-0.62
$Va_1C_1 + H_{tet} \rightarrow Va_1H_1 + C_{oct}$	0.01

over molecular hydrogen ($E_b = 0.004eV$), in the constrained geometries of the bcc Fe lattice, and hydrogen accumulation is not thermodynamically favored. Nonetheless, once one or multiple vacancies are present, the formation energy for molecular hydrogen (H_2) is substantially lowered and the formation of localized clusters containing multiple hydrogen atoms (Figure 3.2.c) is facilitated (H_{II} zone). On the other hand, the stabilizing effect of H in Va-only PDCs implies that the most significant defect clusters in the alloy contain H_2 only up to a maximum $[Va_{tot}]$, which, in principle, is amenable to experimental comparison. This maximum is denoted by boundary A between the H_{II} and H_{III} zones, and is approximately linear on $[H_{tot}]$, i.e., $(2\frac{[H_{tot}]}{3})^{0.9}$. Above this upper-bound, atomic hydrogen-containing PDCs (Figure 3.2.b) again dominate (as in H_I). In this regime ($[H_{tot}] >> [C_{tot}]$), as vacancy concentrations increase for a fixed $[H_{tot}]$, dominant PDCs first switch from tetrahedral hydrogen interstitials to Va_1H_2 (zone H_{II}); upon crossing zone boundaries A, B, and C, stoichiometry of the dominant PDC then changes from Va_1H_1 (zone H_{III}) to Va_2H_1 (zone H_{IV}) to Va-only PDCs (zone Va_{II}) respectively.

Turning now to regions in which all three point defect types (Fe vacancies, H, and C) interact and carbon-containing PDCs are statistically relevant, the full complexity of the PDC populations is apparent. Interactions between hydrogen and carbon interstitials are similarly mediated by vacancies. Our energy calculations (Table 2) show which binding mechanisms are thermodynamically disfavored for H and C in the presence of Va. We observe that hydrogen does not bind with carbon in the absence of iron vacancies. This is consistent with observations showing that hydrogen is repelled from regions of high mass and charge density [61] such as interstitial carbon atoms within the highly confined geometry of the bcc Fe lattice (Figure 3.2.e). Furthermore, as shown in the second reaction in Table 2, hydrogen is unable to displace

carbon from existing PDCs and instead binds to those clusters. The absorption of hydrogen into larger PDCs is also thermodynamically favored (Table 3). However, as the number of solute atoms in the PDC grows, the presence of additional vacancies is required to promote hydrogen binding. For example, two vacancies are insufficient for complete binding of one carbon and two hydrogen atoms (especially given the instability of CH_2 in vacuum) so the $Va_2C_1H_2$ PDC lowers its energy by spreading from a symmetric configuration to a loose structure where the C atom is as far away from the H_2 molecule as possible while remaining bound. Appreciable lattice distortions in the form of extended defects, such as precipitate interfaces [41], can also provide an analogous effect to that of vacancies in the bulk lattice by facilitating C-H binding. The combination of the two competing processes of hydrogen-carbon interactions (repulsion in the absence of vacancies but high affinity when mediated by vacancies) results in an effective decoupling of the Va_xH_z and Va_xC_y PDC populations; that is, vacancy-solute (Va-H and Va-C) interactions become the primary contributors to the binding processes. The remaining interactions which complete the three-body description of this alloy, i.e., the C-H and Va-C-H interactions, represent a substantially less significant effect in terms of determining the type and concentration of PDCs. In particular, for low total vacancy concentrations no dominance zone in which C_yH_z PDCs dominate exists. Furthermore, as can be seen in Figure 1, in the regime in which $[H_{tot}] \sim 0.1[C_{tot}]$, the spectrum of the Fe-C-H system shows a rich variety of statistically relevant PDC types due to the vacancy mediated interactions. Therefore, the dominance of specific PDCs in this regime is strongly dependent on $[Va_{tot}]$ in a highly non-trivial manner. Nonetheless, the transition from atomic to molecular to atomic hydrogen is preserved as $[Va_{tot}]$ increases, though these PDCs are no longer dominant.

For low $[Va_{tot}]$ (in this regime in which $[H_{tot}] \sim 0.1[C_{tot}]$), carbon interstitials are the prevalent PDC (C_I zone) and no binding between H and C is found to occur. Clusters containing both H and C, such as $Va_1C_1H_1$ (Figure 3.2.d) or $Va_2C_1H_2$ (Figure 3.2.e) PDCs, are never statistically relevant. As $[Va_{tot}]$ increases, Va_2C_4 clusters become the dominant PDC (C_{II} zone), and the concentration of hydrogen-

Table 3.3: Energy changes in binding reactions involving the Va_1C_2 and $Va_2C_1\langle 100\rangle$ PDCs

Reaction	$\Delta E_{reaction}(eV)$
$Va_1C_2 + H_{tet} \rightarrow Va_1C_2H_1$	0.06
$Va_1C_2 + H_{tet} \rightarrow Va_1C_1H_1 + C_{oct}$	0.30
$Va_2C_1 + H_{tet} \rightarrow Va_2C_1H_1$	-0.33
$Va_2C_1 + H_{tet} \rightarrow Va_2H_1 + C_{oct}$	14.6

containing PDCs such as Va_1H_1 and Va_1H_2 also increases. In fact, the addition of H pushes the system into the high-hydrogen regime of the C_{II} zone, rendering the Va_1H_1 and Va_2H_1 PDCs statistically relevant. Based on experimental observations of rapid hydrogen diffusion [38] and given the relatively small radius of the hydrogen atom as compared to bcc Fe vacancies and interstitials, we conjecture that these small Va_xH_z PDCs should be mobile, therefore having important macroscopic consequences which can be tested experimentally. This conjecture is discussed in Section 3.2 when we analyze the migration mechanisms of these PDCs. When the total hydrogen and carbon concentrations become more similar (e.g., $[H_{tot}] = [C_{tot}] = 0.01$), the relative dominance in the diagram changes. Carbon-free defect clusters such as Va_1H_1 (lower end of the H_{III} zone) and Va_1H_2 (lower end of the H_{II} zone) become the dominant PDC. However, Va_2C_4 and Va_2C_2 PDCs remain of significant concentration throughout the $[Va_{tot}]$ range examined. Although never significant, $Va_2C_2H_1$ clusters (di-vacancies oriented in the $\langle 111\rangle$ direction of the bcc Fe lattice) approach significant concentrations when $[Va_{tot}]$ becomes comparable to $[C_{tot}]$ and $[H_{tot}]$; however, in this range, the concentration of several Va_xC_y and Va_xH_z clusters also increases such that the $Va_2C_2H_1$ clusters represent only a minor fraction of the overall PDC spectrum. Similarly, $Va_1H_1C_1$ PDCs are never present in significant proportions, underscoring the effective decoupling of the Fe-C and Fe-H PDC populations.

This decoupling of the PDC types provides a simplifying framework for the study of hydrogen binding in alloys of more complex composition and/or crystalline defect types. Moreover, these observations inform macroscopic concerns of hydrogen damage by indicating conditions under which mechanisms of primary degradation by internal

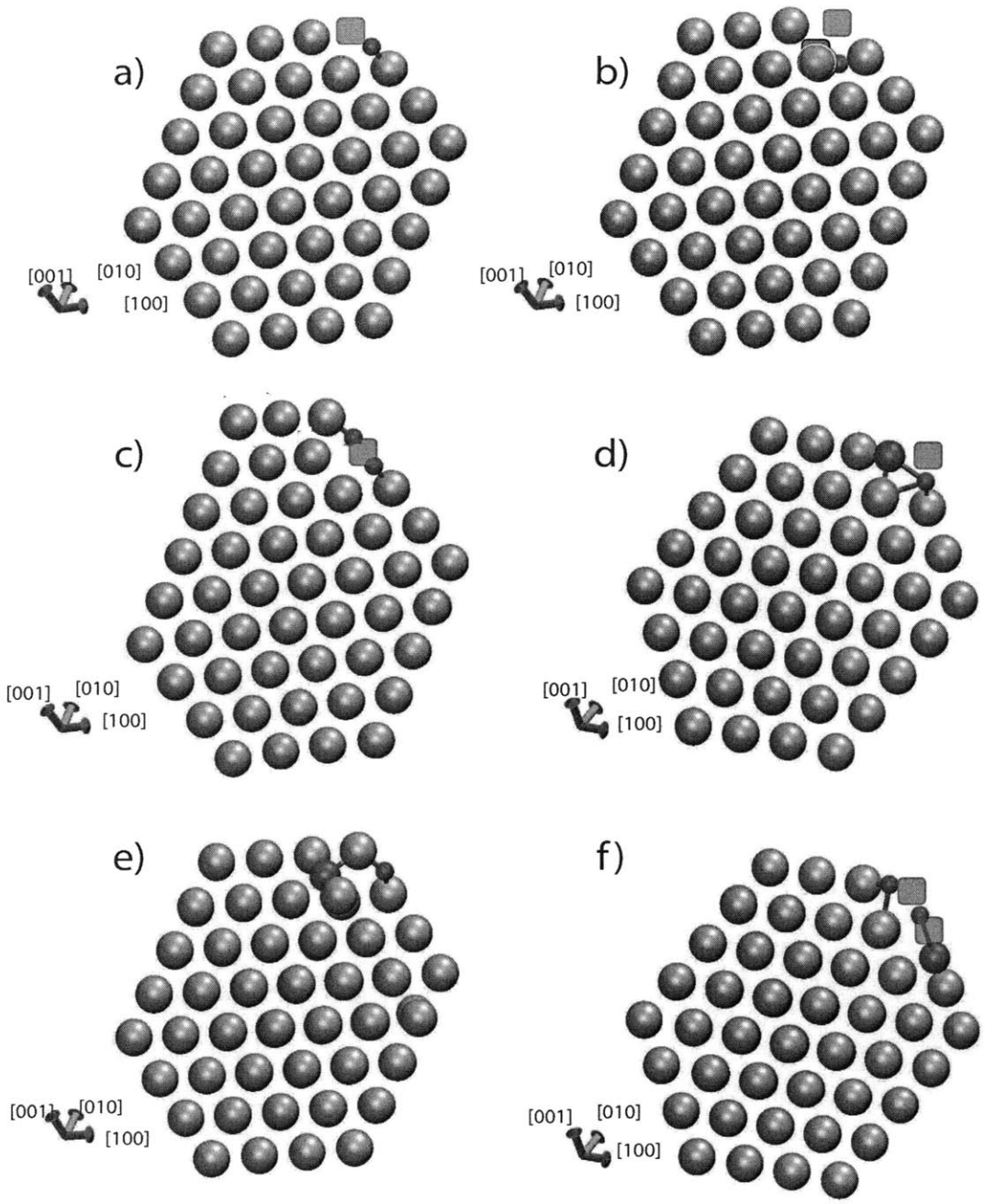

Figure 3-2: Stable geometric configurations for various PDCs comprising vacancies (red squares), hydrogen (blue spheres), and carbon (purple spheres) in a bcc iron (gray spheres) matrix. a) Va_1H_1, b)Va_2H_1, c)Va_1H_2, d)$Va_1C_1H_1$, e)C_1H_1, f)$Va_2C_1H_2$ [62]

hydrogen pressure buildup [41] (i.e., H accumulation) are viable. For such processes to occur, the local vacancy concentration must be such that molecular hydrogen formation is favored, such as in the neighborhood of a micro-void or micro-crack [41]. In other words, the point defect composition must be within the H_{II} dominance zone in Figure 3.1. Finally, given the high concentration of Va_1H_1 and Va_1H_2 PDCs, even when total hydrogen concentrations are relatively small ($[H_{tot}] < 10^{-2.5}$ or ~ 0.3 at. % at the top of C_{II} and C_{III}), these PDCs are likely to be responsible for macroscopic effects which are controlled by the diffusion of Va (and Va-containing PDCs) toward line and surface defects such as dislocations or grain boundaries.

3.1.2 The Role of Methane

Hydrogen in steels at high temperatures is able to react with carbides present in the microstructure to form decarburized structures and methane gas which has a low diffusivity because of its size [63]. Methane bubbles form and eventually grow into fissures and cracks at grain boundaries. The combined process of decarburization, which locally reduces the yield strength from the prepared hardened steel, and fissure production may provide sudden and catastrophic reductions in both strength and ductility. We apply our methodology to calculate the binding energies of different

Table 3.4: Binding free energies for methane-based PDCs at 0 K. Only the deepest energy minimum for each PDC stoichiometry is shown. Other PDCs are shown for comparison.

PDC	$E_{binding}(eV)$
C_1H_4	-0.09
$Va_1C_1H_4$	1.31
$Va_2C_1H_4$	1.15
$Va_1C_1H_1$	1.14
$Va_1C_2H_1$	1.38
C_1H_2	-0.05
$Va_1C_1H_2$	0.92
$Va_2C_1H_2\langle 100\rangle$	1.77
$Va_2C_1H_2\langle 111\rangle$	1.31
Va_1H_3	1.38

geometric configurations of the methane molecule confined in a bcc Fe matrix as well as its interactions with vacancies in the material. These calculations, at 0 K, are summarized in Table 3.4:

The table highlights two important results regarding methane formation in steels which fall within the general framework described in the previous section. First, and similarly to other C-H PDCs, methane gas does not form in a bcc Fe lattice in the absence of vacancies due to the repulsion between the high mass and electron density regions at solute interstitial sites. On the other hand, binding to a single vacancy stabilizes the methane molecule. Second, the stability of the methane molecule is reduced when an additional vacancy binds. This suggests that the ranges at which methane formation is favored are bound in a similar manner to that for molecular hydrogen in the PDC diagram.

However, as can be seen from Table 3.4 by comparing their binding energy to those of other PDCs, methane containing clusters can become a significant PDCs only in regions with very high carbon and hydrogen concentrations, i.e. far outside of the boundaries of the PDC dominance diagram of Figure 3.1. While such conditions are unattainable in the bulk they can occur locally in the neighborhood of grain boundaries, consistent with the experimental observation of grain boundary decarburization and bubble formation [63]. On the other hand, unlike the smaller clusters discussed in the previous section (which are the only ones that can form in significant quantities under realistic bulk concentrations of impurities), a methane molecule bound to a vacancy contains six different elementary point defects and therefore, even though their formation is thermodynamically allowed in equilibrium, this process may not occur in practice due to the energy barriers associated with collective binding of the individual species. Calculating the kinetics of methane formation in steels, by applying the techniques described in this thesis such as nudged-elastic band (NEB) or the ABC method is thus a natural next step in understanding embrittlement in steels.

3.2 Point Defect Cluster Migration

Interactions between point defects and the resulting PDC dominance diagram of the previous section are essential in understanding the mechanisms of hydrogen degradation in steels because they provide insight into the possible species that define the microstructure of the material. However, the phenomenon of embrittlement is, at its core, a time-dependent phenomenon which manifests itself as delayed hydrogen-induced cracking (HIC) in high-strength alloys and loss in tensile ductility and ductile fracture for lower strength stainless steels. As a result we must study the kinetic behavior in addition to the equilibrium properties. That is, we must determine the saddle points in addition to the configurations at the energy basins.

Unlike the roughness characterizing the free energy landscape of each specific cluster, i.e., the free energy as a function of the positions of the species in a given PDC, the energy landscape characterizing the migration of a cluster through the matrix is more predictable. This is intuitive since the PDC geometric configuration is highly dependent on the interactions between specific species in which quantum mechanical effects play a very important role. On the other hand, since the concentrations of impurities is low and the Fe matrix remains crystalline the number of type of transitions during bulk diffusion are easy to determine from basic symmetry principles. Therefore we can determine the migration energy barriers using the NEB method without resorting to ABC. This is particularly advantageous in this case since by using a less demanding method to study the (simpler) topology of the landscape we can refine the accuracy of the total energy calculations and include important electronic structure effects via DFT.

From the PDC dominance diagram of Figure 3.1. we see that the most important hydrogen-containing species for high hydrogen containing steels are those which dominate regions H_I through H_{IV}, that is H_{tet},Va_1H_1, Va_1H_2 and Va_2H_1. Given the small size and high vacancy concentrations required for the system to be in H_{IV} we choose to only study the migration mechanisms of the first three of these PDCs. For each defect species we evaluate a small number of potential migration mechanisms

which are chosen based on symmetry principles. The lowest migration barrier is then chosen as the most likely candidate mechanism unless multiple ones have activation barriers of similar height. As before, all the NEB/DFT calculations were performed using the VASP code [53] with Blöchl's projector augmented method [54]. Calculations were carried out with a plane-wave energy cutoff of 400 eV in 54-atom, rather than 128-atom, super-cells with the theoretical lattice constant of 2.835 $\mathring{A}$, using the same settings as those for the total energy calculations. Four (4) images are chosen for the NEB and the RMM-DIIS algorithm is used for geometric relaxation, terminated with a force cutoff of 5 $meV/\mathring{A}$.

We first consider the migration of a hydrogen interstitial, H_{tet} in equilibrium, through the bcc Fe matrix. Our NEB/DFT calculations show that the favored migration mechanism has a barrier of $E_m = 0.08$ eV which is consistent with experimental observations [41]. The activation barrier and migration mechanism are illustrated in Figure 3.3 [2]. In this case hydrogen, situated at a tetrahedral site, migrates by diffusing in the $\langle 01\bar{1} \rangle$ direction to a neighboring tetrahedral site, with a saddle point near the trigonal interstitial site. That is, hydrogen diffuses on the atomic planes rather than in between the planes. Migration in between planes (e.g., in the $\langle 10\bar{1} \rangle$ direction in our example) has a much higher barrier of 0.9 eV due to the Fe bonds between planes. Furthermore migration takes place through tetrahedral sites only, without traversing octahedral sites. Two of these tetrahedral-to-tetrahedral transitions result in an effective rotation about the $\langle 1\bar{1}1 \rangle$ direction as highlighted in Figure 3.3.

Figure 3.2.a shows that the presence of a vacancy results on relaxation of the tetrahedral hydrogen interstitial (H_{tet}) into an octahedral site in a dumbbell-like configuration (e.g., in the $\langle 001 \rangle$ direction). Our DFT-NEB calculations, starting from such an equilibrium geometry and summarized in Figure 3.4, suggest that the favored migration mechanism for the Va_1H_1 cluster consists of a nearest neighbor migration of the vacancy away from the hydrogen interstitial, which in turn relaxes to a tetrahedral site almost as if it were free. This process occurs with an activation energy barrier of 0.71 eV, which is slightly higher than the free vacancy migration energy barrier

[2] Throughout this thesis we use visualizations rendered using AtomEye [64].

(0.53 eV). This step is then followed by rapid migration of the hydrogen interstitial (the interstital migration barrier of 0.07 eV decreases slightly as the hydrogen atom approaches a vacancy) from the relaxed tetrahedral site through two tetrahedral sites until it relaxes to an octahedral next to the vacancy forming a new dumbbell. Hence, despite its small mass and associated local charge distortions, hydrogen binding decreases the mobility of the vacancy. Migration of the vacancy to a nearest neighbor in the $\langle 111 \rangle$ direction towards the hydrogen atom (which in turn moves from its octahedral site to a new one by migrating in the $\langle 010 \rangle$ direction or an equivalent one) results in a twist of the dumbbell about the $\langle 010 \rangle$ direction and has a migration energy barrier of $E_m = 1.06$ eV. All other alternative migration mechanisms have energy barriers surpassing 1.2 eV and are thus thermodynamically disfavored. Finally, the dissociative mechanism has a corresponding migration barrier equal to that of the individual defect plus the binding energy for the Va_1H_1 defect which is equal to $0.51eV$ at $T = 0$ as show in Table 3.1. This would result in effective dissociation migration barriers of $E_m = 0.51 + 0.08 = 0.59$ eV for the dissociated hydrogen atom and $E_m = 0.51 + 0.53 = 1.04$ eV for the dissociated vacancy.

Finally, and as discussed in the previous section, the presence of one vacancy promotes the binding of two hydrogen atoms into a H_2 molecule. At equilibrium the 2 hydrogen atoms form a dumbbell with the vacant site in the center (Figure 3.2.c), so we investigate the migration mechanisms starting from that initial configuration. Figure 3.5 shows the favored non-dissociative migration mechanism for the Va_1H_2 PDC. The mechanism consists of a rotation of the dumbbell perpendicular to its axis ($\langle 010 \rangle$ in Figure 3.5) and a translation of the center of mass/vacancy to a nearest neighbor (i.e. $\langle 111 \rangle$ direction in the figure). This mechanism has an activation energy of $E_m = 1.63$ eV. Migration of a Va_1H_1 dumbbell subcluster to a first nearest neighbor configuration is stable but has an activation barrier of $E_m = 1.79$ eV and is thus not favored. Hence even though the configuration with a separated Va_1H_1 cluster and a hydrogen interstitial is only 0.59 eV higher than the Va_1H_2 cluster the activation energy for dissociation into those defects is prohibitively high. In addition, and as shown in Table 3.1, the binding energy of the Va_1H_2 PDC is 1.11 eV at 0

K. Therefore dissociation into individual defects and the migrating has an effective migration barrier of, at least, $E_m = 1.11 + 0.53 = 1.64$ eV. All other migration mechanisms between stable configurations have barriers of 1.8 eV or above. Due to these high barriers, the Va_1H_2 PDC is essentially immobile.

We calculate the jump frequencies ν by relying on Harmonic Transition State Theory (Section 2.1.1). In this case we fit the curvature of the local energy landscape calculated with NEB/DFT near the initial minimum configuration with a quadratic equation from which we obtain the coefficient corresponding to the normal frequency. This is equivalent to taking the normal frequency corresponding to the reaction coordinate from the NEB method, which can be shown to be rigorously equivalent to the expansion of Section 2.1.1. The average distance traveled by the PDC during a jump is also given directly from the calculations. Table 3.5 summarizes the calculated jump characteristics for these three defects as well as for the free vacancy and divacancy clusters.

Table 3.5: DFT calculated migration energy barriers and jump frequencies for H_{tet}, Va_1H_1,Va_1H_2, Va_{free}, and Va_2 in bcc Fe. Experimental values are listed in parenthesis (when available). The jumping characteristics for Va_2 are obtained from Reference [65].

PDC	$E_{migration}(eV)$	Jump frequency (THz)	Distance traveled ($\AA$)
H_{tet}	0.08 (0.07 [41])	14.93	1.01
$Va_1H_1(\langle 100\rangle \rightarrow \langle 554\rangle)$	0.71	3.91	2.35
$Va_1H_1(\langle 100\rangle \rightarrow \langle 010\rangle)$	1.07	2.45	2.43
Va_1H_1 (dis.)	1.04	3.34	2.44
Va_1H_2	1.63	1.92	2.40
Va_1H_2 (dis.)	1.64	3.34	2.44
Va_{free}	0.53 (0.55 [57])	3.34	2.44
$Va_2(\langle 1nn\rangle \rightarrow \langle 2nn\rangle)$	0.98	27.55	2.87
$Va_2(\langle 1nn\rangle \rightarrow \langle 4nn\rangle)$	0.81	9.13	2.87

From our understanding of the migration of individual PDCs we can resort to Einstein's equation to calculate effective diffusion coefficients in the material given

by:

$$D^*_{Fe}(T) = \sum_{i,withVa} a_i^2 c_i \nu_i^o \exp(\frac{-E^{(i)}_{migration}}{kT}) f_i \tag{3.9}$$

$$D^*_{H}(T) = \sum_{i,withH} a_i^2 c_i \nu_i^o \exp(\frac{-E^{(i)}_{migration}}{kT}) f_i \tag{3.10}$$

where a_i is the distance traveled by the PDC during an individual transition, c_i is the concentration of the PDC, ν_i is the jump frequency for the transition, $E^{(i)}_{migration}$ is the migration energy barrier, f_i is the correlation factor of Bardeen and Herring [66] that corrects Einstein's expression to account for geometric correlations in the random walk, and the sums are over Va-containing defects for the self-diffusivity and H-containing defects for the H diffusivity. The correlation factor for single vacancy diffusion is given by $f_{Va} = 0.72149$ for a bcc lattice [67]. In addition, our calculations in Section 3.1. suggest that we can consider H interstitials to effectively block their own site as well as all the nearest neighbor interstitial sites in the absence of a vacancy. We can therefore use the correlation factor for model 1 of Faux and Ross [68] given by:

$$f_{H_{tet}} = 1.0 - 2.18c_{H_{tet}} + 1.56c^2_{H_{tet}} - 7.08c^3_{H_{tet}} \tag{3.11}$$

in addition the correlation factor for divacancies is given by [69]:

$$f_{Va_2} = 0.469 - 0.103s - 0.076s^2 - 0.043s^3 + 0.018s^4 - 0.0055s^5 \tag{3.12}$$

where:

$$s = \frac{1}{0.33e^{0.18/kT}} \tag{3.13}$$

in our case, so at $T = 450K$ we have $s = 0.029$ and $f_{Va_2} = 0.466$. We approximate the correlation factors for Va_1H_1 and Va_1H_2 by those of a single vacancy. [3]

Combining all the data in Table 3.5 with the correlation factors for each of the relevant defects we can calculate diffusion coefficients for the Fe-H alloy from Equation

[3]For greater accuracy in the correlation factors we can introduce our calculated probabilities in a KMC algorithm and obtain numerical estimates of f for all the cases, but given the disparities in activation barriers these level of accuracy is unnecessary

(3.9). These results as a function of both total vacancy and hydrogen concentration are summarized in Figure 3.6. and 3.7 for the self-diffusivity and hydrogen diffusivity respectively. Given the effective separation between Fe-H and Fe-C populations discussed in Section 3.1. and the fact that the Va_2C_4 clusters are essentially immobile [65], the total self-diffusivity for the full ternary alloy is determined primarily by the concentration of free vacancies, divacancy clusters, and H-V PDCs so our figures can easily be extended to other Fe-C-H alloys.

The migration results for the Va_1H_1 and Va_1H_2 clusters show that self-diffusion by the vacancy mechanism and hydrogen diffusion are hindered by binding. Hydrogen diffusion, driven primarily by the rapidly moving free hydrogen atoms in tetrahedral sites, increases monotonically when total hydrogen concentration is increased or total vacancy concentration is decreased. The hydrogen diffusion coefficient decreases through two regimes with different slopes (see inset in Figure 3.7). The inflection points occur as the system moves from region H_I to H_{II} (and higher vacancy content areas) in the PDC dominance diagram. As the dominant migrating PDC switches from H_{tet} to Va_1H_1 and Va_1H_2 the hydrogen diffusion coefficient decreases accordingly. At high vacancy concentrations, all hydrogen becomes bound in larger immobile $Va - H$ clusters and hydrogen diffusivity becomes negligible. Self diffusivity, driven primarily by free vacancy migration, decreases monotonically as total hydrogen concentration increases and increases as total vacancy concentration increases. The dependence in total vacancy concentration takes place in three distinct regimes (see inset in Figure 3.6) as the system switches from H_I to H_{II}/H_{III} to Va_I/Va_{II}. This results in a change in the main self-diffusion migration mechanism from being essentially negligible to driven by Va_1H_1 migration to Va_{free} and Va_2 migration after which we see a saturation effect.

The combination of these results and the PDC diagram in Figure 3.1 generates a more complete picture of the potential degradation mechanisms in Fe-H (and Fe-C-H). Expanding on the insight of Section 3.1, we propose four distinct types of H-Va behavior depending on the relative concentrations of hydrogen and vacancies. These types of behavior can be directly linked to proposed embrittlement mechanisms. As seen

in Figure 3.7, Zone H_I (high hydrogen, low vacancy concentration)is characterized by rapidly diffusing free hydrogen interstitials so the main degradation mechanism is associated with *diffusion of hydrogen*, e.g., corrosion cracking at stress concentrators. Zone H_{II} is characterized by the prevalence of the Va_1H_2 PDCs which are essentially immobile, so the primary degradation mechanism is driven by *accumulation of hydrogen*, e.g. formation of hydrogen atmospheres and hydrogen bubbles. Hydrogen diffusion, though greatly reduced, remains relevant due to the high mobility of the (few) hydrogen interstitials. Zones H_{III} and H_{IV}[4] have significant populations of free vacancies and Va_1H_1 PDCs. Therefore *self-diffusion by a vacancy mechanism* becomes a relevant kinetic process which could lead to degradation in the form of creep. Finally, the vacancy-rich regimes of Va_I and Va_{II} exhibit both self-diffusion and *accumulation of vacancies* which could, in principle, lead to void formation and growth. As discussed in the following section, these insights must be combined with a more complete analysis of PDC-line defect interactions in order to make definitive conclusions about embrittlement and long term degradation.

3.3 Hydrogen Effects on Time Dependent Degradation

The results described in the previous sections serve as the basis for larger scale models of hydrogen embrittlement in metals, particularly in steels in hydrogen-rich environments. By coarse graining the results and informing the larger length and time scales with the composition, structure, and diffusion calculations we can incorporate additional elements that are determinant of the alloys susceptibility to embrittlement. In particular, the essential element of deformation is missing from our calculations. In order to develop a predictive model of embrittlement we therefore need to consider the interactions of our PDCs with dislocations, grain boundaries, and cracks to capture

[4]Since we are not including Va_2H_1 defects this calculation is not completely accurate for the small H_{IV} region in the PDC dominance diagram, though the migration mechanisms of the other PDCs suggest that Va_2H_1 defects should not be very mobile in comparison to free vacancies, hydrogen interstitials, or $Va_1H)_1$.

the plastic and fracture behavior. This section summarizes the current experimental and theoretical knowledge in the area and suggests a multiscale methodology for connecting our results directly to degradation predictions.

The first to suggest that hydrogen-induced brittle failures were preceded by significant local plastic deformation was Beachem in 1971 [70], and evidence from fractographic studies [71, 72] seems to suggest that plastic tearing is indeed a major predecessor to HIC. Among many potential plasticity mechanisms which have been proposed to account for this "hydrogen softening" effect, two in particular have gained recent support in the literature: hydrogen enhanced localized plasticity (HELP) and a stress relaxation (creep) process induced by an increased vacancy concentration resulting from the strong interaction between vacancies and hydrogen. The HELP mechanism is much promoted by the Mechanical Engineering group at University of Illinois at Urbana-Campaign [45–47]. They have shown that the presence of hydrogen in the form of Cottrell atmospheres around the dislocation lines will "shield" the elastic stress field of dislocations, allowing dislocations of the same sign to closer approach each other in dislocation pile-ups at various obstacles. This in turn allows more dislocation glide to occur for a given loading situation, as compared to in the absence of hydrogen. In addition, studies based on ab initio calculations [73,74] have found evidence that hydrogen modifies the nature of chemical bonding in aluminum in ways which seem to lead to HELP. Experiments upon which the HELP mechanism is based rely on detailed understanding of the fracture mechanics by analyzing at sufficiently high resolution to resolve mechanistic details. High-resolution fractography of hydrogen embrittled metals, such as Ni and Fe, show extensive plastic deformation localized along fracture surfaces [43,75]. In addition, experiments using in situ TEM have also been performed in a variety of hydrogen embrittled systems [76] confirming that the fundamental character of the fracture processes involved in hydrogen embrittlement was the same and showing that hydrogen increased the dislocation mobility under conditions of constant stress. Specimens containing stress concentrators, such as notches and cracks, failed by ductile plastic processes at the front of the notch when stressed in vacuum. However when stressed under gaseous H_2, the

extent of the plasticity in the fracture mode was more confined to regions adjacent to the fracture surface. In relatively pure specimens the fracture tended to be along slip planes and the deformation accompanying the fracture was within $1\mu m$ of the active slip planes. In addition, cracks which had stopped propagating in vacuum under a constant external load could be started and continued to propagate by solely adding hydrogen gas to the environmental cell. Observations showed that this process was related to increased dislocation activity at the crack tip where the specimen was exposed to the gas further supporting the HELP mechanism. In 2000, Jagodzinski et al. [77] aimed at quantifying the HELP mechanism. They referred to a slow strain-rate test (imposed low strain-rate) of pure iron, tested at low temperature (200 K), without and in presence of hydrogen (electrolytic charging). Testing in absence of hydrogen led to a gradual stress build-up with increased strain, while a marked stress reduction (approximately 40%) occurred during periods when hydrogen was present. Jagodzinski and co-workers found that the stress relaxation effect observed was too large to be possible to explain by the HELP mechanism. Instead they concluded that the softening effect is more likely caused by the strong hydrogen-vacancy interaction leading to an increased vacancy concentration and hydrogen enhanced dislocation climb in dipole type dislocation pile-ups. This explains, for a given applied strain, the observed stress relaxation in the system.

In order to incorporate these effects we need to include extended defects in our model. One possibility is to develop hydrogen-iron and hydrogen-carbon interatomic potentials that accurately replicate the energy landscapes obtained from the DFT calculations given above. These potentials could be used to calculate the binding energies to larger defects such as dislocation cores, grain boundaries, and crack tips, as well as the dependence of migration energy barriers on the separation from those extended defects. These environment-dependent migration rates near extended defects can be then incorporated into kinetic Monte Carlo simulations of heterogeneous diffusion. By using spatially dependent barriers the model can explicitly include atomistic resolution of the interaction of PDCs with dislocation cores and could then, in principle, be used to model dislocation climb, glide, and macroscopic creep. A similar

KMC model capturing the interactions of vacancies with dislocation cores to describe dislocation climb has recently been developed by Kabir and collaborators [78]. Such a model could be generalized to include hydrogen and other alloying elements and used to model embrittlement as described. Additionally, the KMC formalism could be complemented with an ABC-MC hybrid step (Section 2.3.1) or with ABCD to model the fracture and plastic behavior at more realistic strain rates.

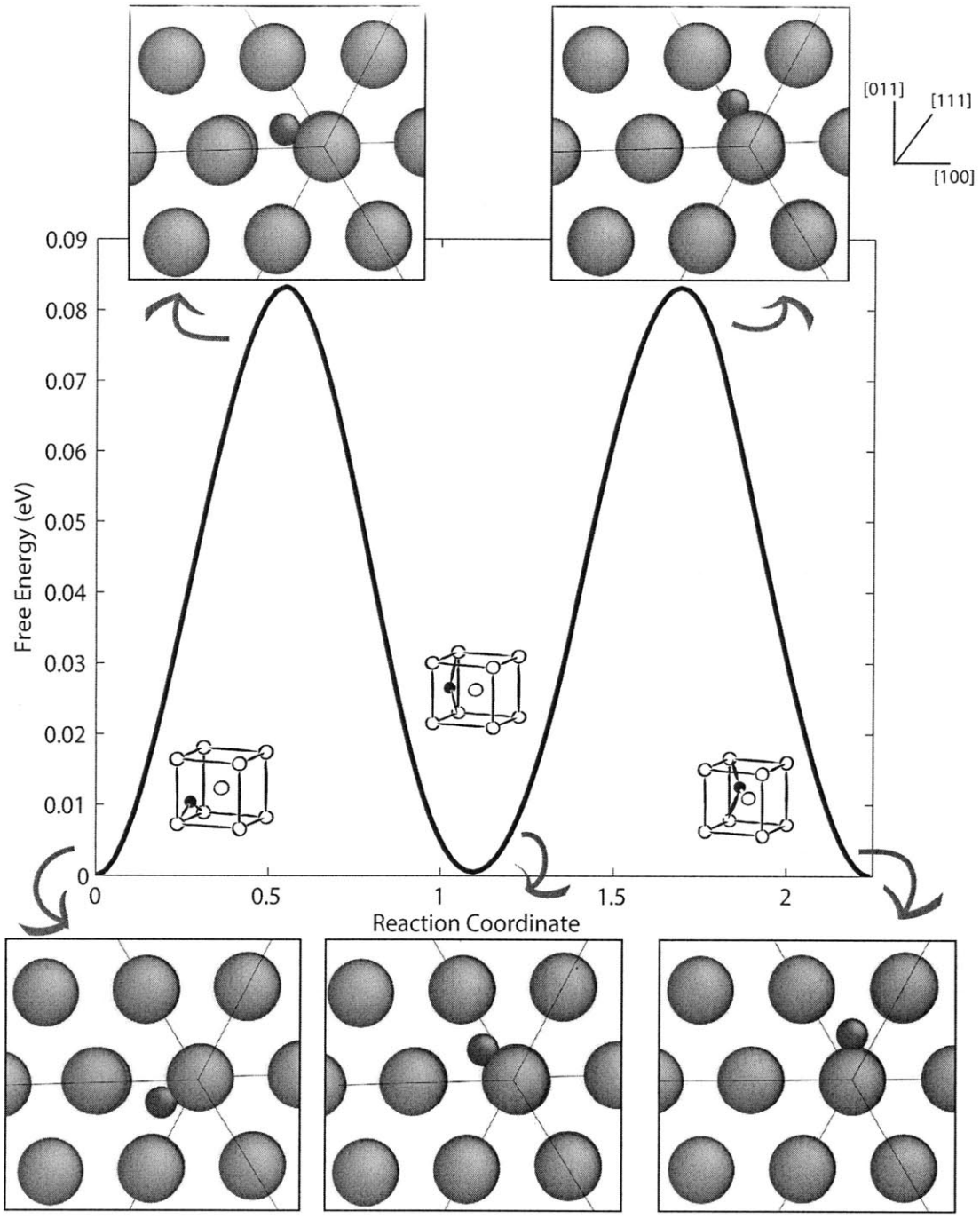

Figure 3-3: Favored migration mechanism for an interstitial hydrogen atom in bcc iron. The hydrogen atom (filled circle) migrates from its equilibrium tetrahedral site to a neighboring tetrahedral site with a saddle point at a trigonal site. Two such jumps are displayed, resulting in a rotation about the $\langle 1\bar{1}1 \rangle$ direction. The process has a migration energy barrier of $E_{migration} = 0.08$ eV. The distortions to the Fe lattice are minimal.

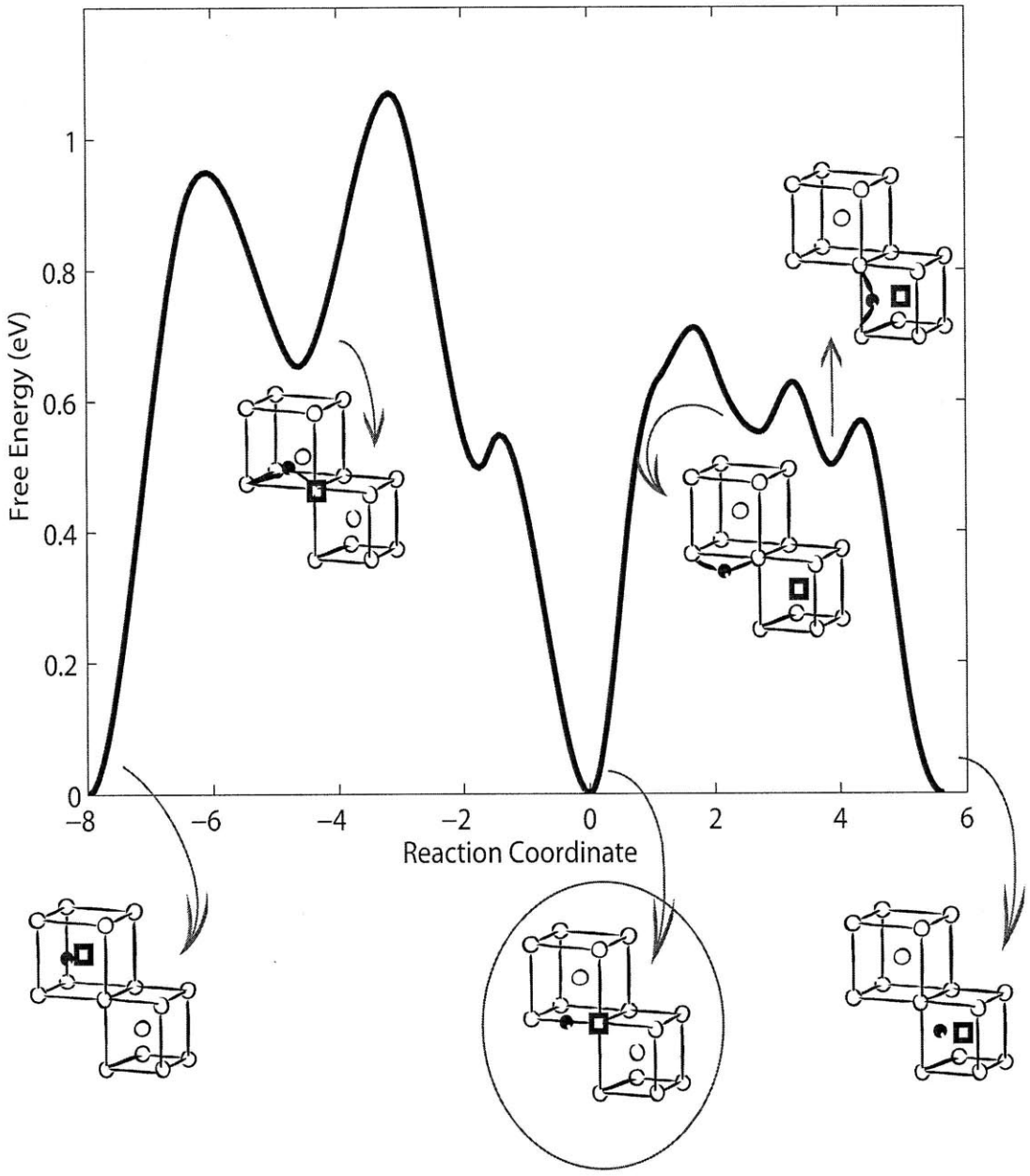

Figure 3-4: Migration mechanisms of Va_1H_1 in bcc iron. As shown to the right, starting from a dumbbell configuration (circled) in the $\langle 001 \rangle$ direction, the vacancy (open square) can migrate to a nearest neighbor configuration away from the hydrogen atom ($\langle 100 \rangle \rightarrow \langle 554 \rangle$, $E_m = 0.71$ eV) and is followed by rapid hydrogen (filled circle) migration, or, as shown to the left, the full dumbbell can translate while twisting about the $\langle 010 \rangle$ direction ($\langle 100 \rangle \rightarrow \langle 010 \rangle$, $E_m = 1.07$ eV).

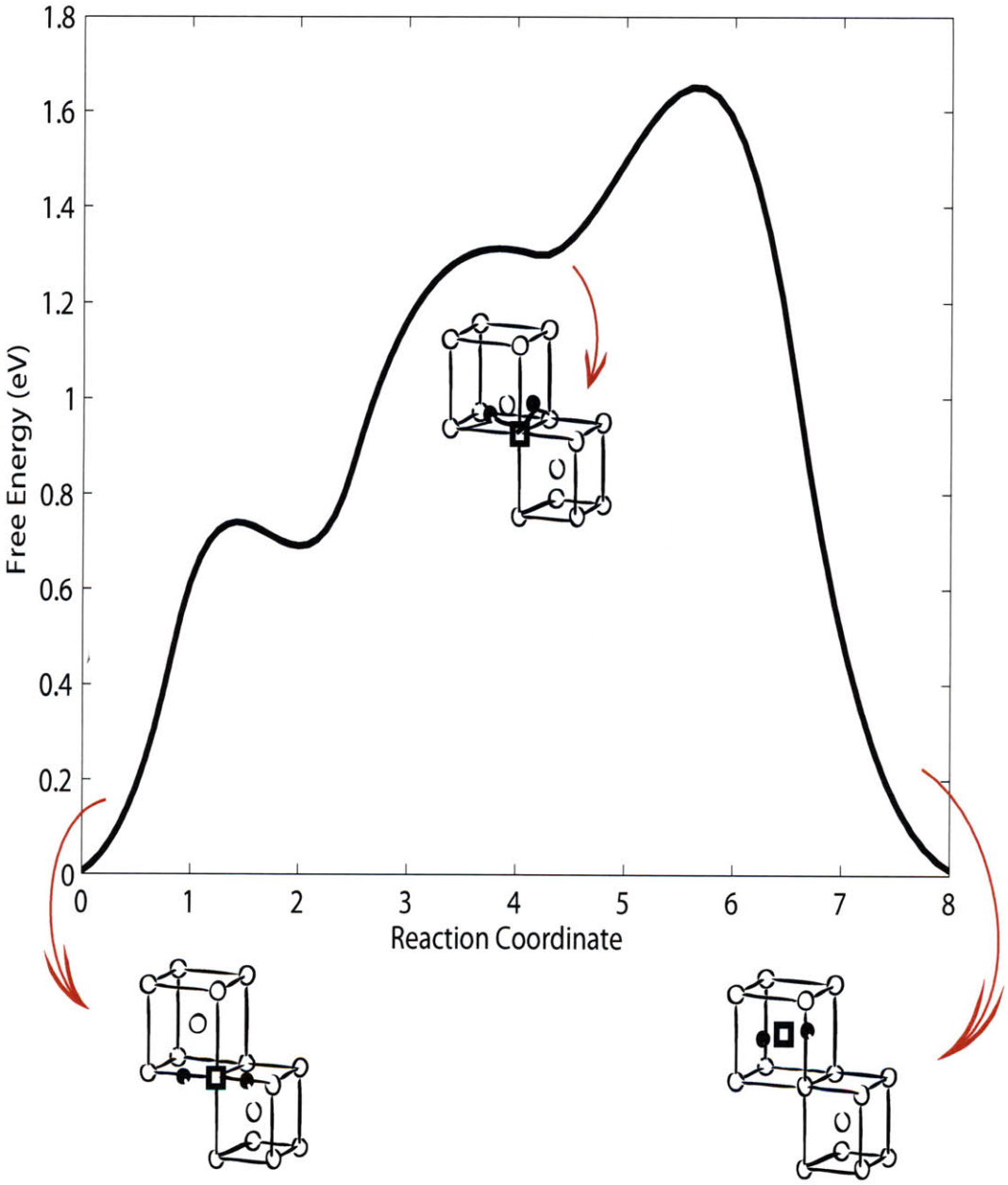

Figure 3-5: Migration mechanism of Va_1H_2 in bcc iron. Starting from a dumbbell configuration in the $\langle 001 \rangle$ direction, the Va_1H_2 PDC rotates about the $\langle 010 \rangle$ direction while its center of mass/vacancy translates to a first nearest neighbor site. The mechanism has an activation energy of $E_m = 1.63$ eV. Vacancies are represented by open squares and hydrogen interstitials by filled circles.

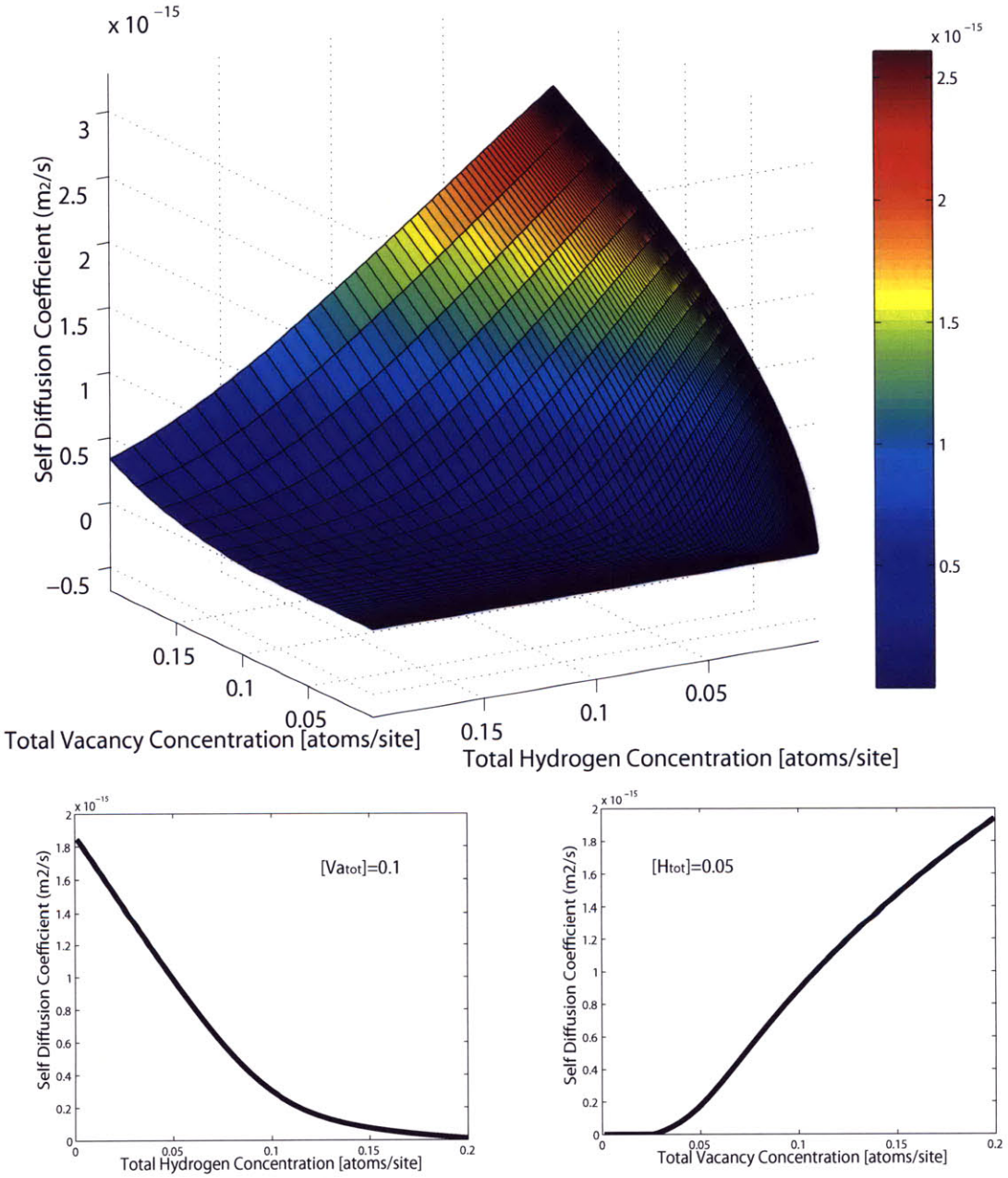

Figure 3-6: Self diffusion coefficient in Fe-H as a function of hydrogen and vacancy concentrations. The insets shows an example of the hydrogen diffusion coefficient at fixed total vacancy and total hydrogen concentrations

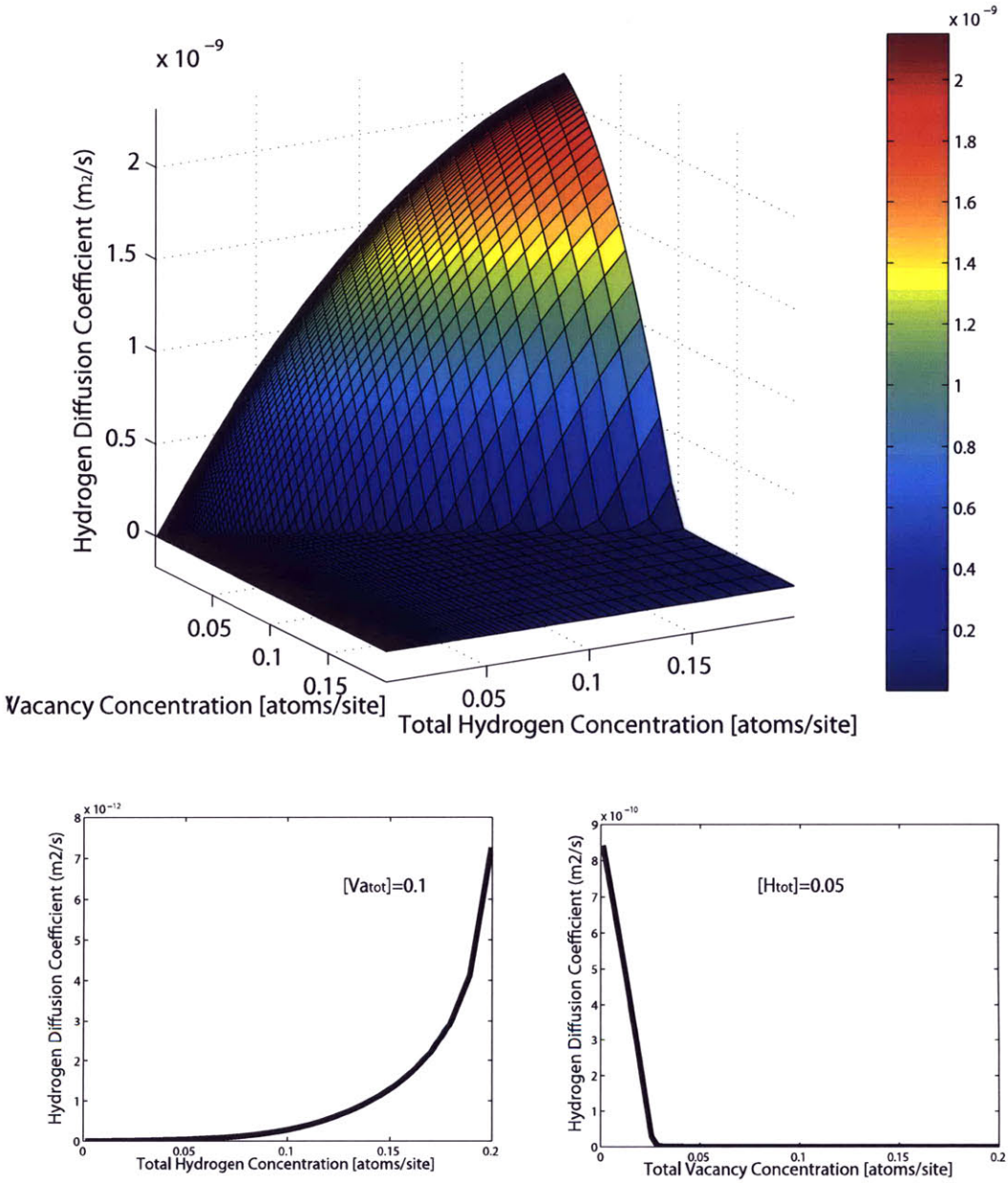

Figure 3-7: Hydrogen diffusion coefficient in Fe-H as a function of hydrogen and vacancy concentrations. The insets shows an example of the hydrogen diffusion coefficient at fixed total vacancy and total hydrogen concentrations.

Chapter 4

Radiation Induced Swelling in Metals

Our exploration of rough energy landscapes in defected condensed matter moves from the spatially ordered hydrogen-containing alloys of Chapter 3 to the much more defective and out of equilibrium microstructure observed in irradiated metals. While the problem of hydrogen embrittlement highlighted the complexity in the energy landscape resulting from the interactions between multiple point defect species and the hydrogen chemistry, the topological structure of the system was largely regular and long-range order was preserved. In particular, the behavior of the PDCs in Fe-C-H is characterized by a complex free energy landscape when determining the PDC structures, but a smoother, more predictable one for the migration of the PDCs themselves. This enabled us to determine the transition pathways during diffusion based on symmetry principles, and use the NEB method to study the time evolution of the system. As we will see in this chapter, the drastic increase in microstructural complexity resulting from radiation damage precludes us from using such methods. We must resort to a combination of non-equilibrium MD, ABC, and ABCD to analyze the long run evolution of the system. Nevertheless, increasing the complexity of the material and the power of our simulation methods comes at a cost. First, our computational demands increase significantly, so we can no longer model the system at the electronic structure level and instead rely on interatomic potentials to describe

the interactions. Second, even though our methods permit analysis and predictions at long time scales their accuracy is limited by the parameters associated with the ABC and ABCD methods as well as the inherent size limitations. Despite these two limitations, the methods prove to be powerful tools in generating new insight into the problem of radiation damage of materials.

4.1 Void Swelling in Metals and Alloys

Irradiation of metals leads to dramatic changes in the microstructure as a result of the displacement of lattice atoms and the deposition of energy via electronic and ionic excitations [79,80]. Of particular importance are dimensional instabilities which can be perceived at ordinary macroscopic length scales such as creep, growth, shrinkage, and swelling [79, 81]. Irradiation creep and growth are volume-conserving shape-modifying processes which occur as a result of applied stresses (creep) or inherent anisotropies (growth) and are enhanced by the irradiation induced microstructural changes. Shrinkage and swelling, on the other hand, involve decreases or increases of volume respectively. Swelling, in particular, can occur by the formation and growth of voids, the retention of lattice vacancies, or the development of less dense phases [79]. All of these processes can result from the formation and evolution of Frenkel pairs produced during displacement cascades and their subsequent interactions with the evolving metallic microstructure.

Irradiated crystalline metals are characterized by supersaturation of both vacancies and self-interstitial atoms (SIA) generated during displacement cascades. Though a large fraction of the defects generated during the cascade recombine after a few picoseconds, the concentrations of both vacancies and SIAs left is orders of magnitude higher than those for the unirradiated metal. Various sinks in the microstructure, such as cavities, surfaces, and grain boundaries trap both vacancies and SIAs in an unbiased manner and contribute to the recovery of the lattice. On the other hand, the stress fields of dislocations preferentially attract SIAs over vacancies [82]. As a result of this bias, approximately 20% more interstitials than vacancies are absorbed

by dislocations, leaving a slight excess of vacancies which first nucleate into and then grow voids (Figure 4.1). Voids can then be filled with gases such as hydrogen (Section 3.1) or helium and form pressurized bubbles inside the material.

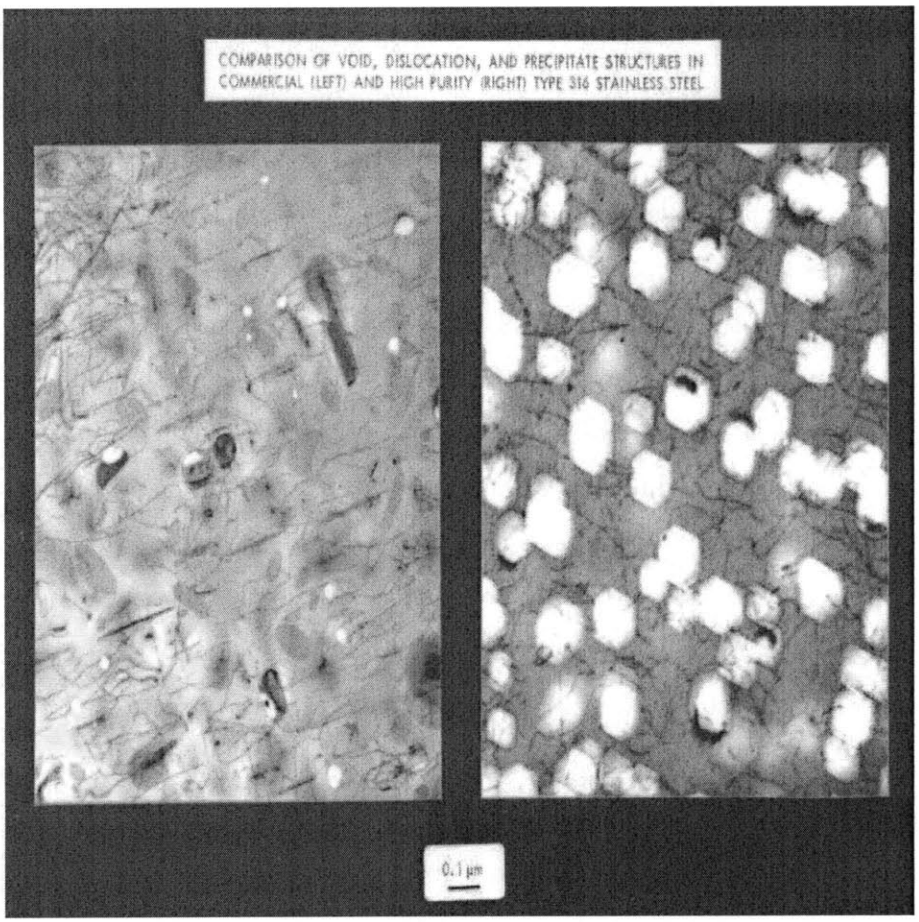

Figure 4-1: TEM comparison of void, dislocation, and precipitate structures in commercial (left) and high purity (right) type 316 stainless steel.

The formation and growth of these voids in many metals after high-dose irradiation at elevated temperatures has been the subject of extensive experimental and theoretical investigation [83–88]; primarily because of the importance of the resulting volume expansion in the design of fast reactor cores. Void growth and nucleation is strongly dependent on many variables including vacancy, precipitate, and dislocation concentrations, temperature, coherence of precipitated phases, and the crystalline structure of the material. For example, it is observed, experimentally, that voids

sometimes grow on precipitates, notably on $M_{23}C_6$ particles in type 316 steels [89], whereas in other materials, such as PE 16 steel, the precipitates apparently suppress void growth [90]. Vacancies have also been shown to contribute in the formation and growth of the precipitates themselves as the irradiated material ages [91]. It has been determined that void swelling develops in austenitic stainless steels over a range of temperatures starting at the onset of vacancy migration (about 300^oC for austenitic steels) to regions dominated by self-diffusion (about 650^oC). Both macroscopic void swelling and microscopic void nucleation possess initial incubation delays (Figure 4.2). For austenitic stainless steels the macroscopic incubation doses range from ~ 0.1 dpa to over 10 dpa after which the volume increases at a rate of 1%/dpa [92] which dramatically alters the engineering properties of the material. Thus, the incubation time effectively defines the useful lifetime of a component in a reactor. The complexity of the phenomenon and the roughness of the underlying energy landscape result on a strong dependence of the incubation period on the dose rate, i.e. that a lower irradiation dose rate requires a smaller cumulative fluence to complete the incubation process [92]. This behavior constrains the predictive power of extrapolated experiments at high dose rates as steady-state behavior is confused with the late stages of the transient period.

Additional open questions in the study of radiation swelling in metals are the strong relationship between creep and swelling [86], which in principle could be investigated by a combination of ABC, ABCD, and KMC as suggested for hydrogen embrittlement in Section 3.3, and the significant disparity between the swelling levels in ferritic and austenitic steels. Void swelling in ferritic steels is found to be significantly lower than in austenitic alloys but the cause of this difference is not yet clearly understood. Several theories have been proposed but no consensus has been established in the pertinent literature. The best accepted conjectures can be summarized as [93]:

- The point defect bias to dislocations is inherently lower in the bcc ferritic crystal structure.

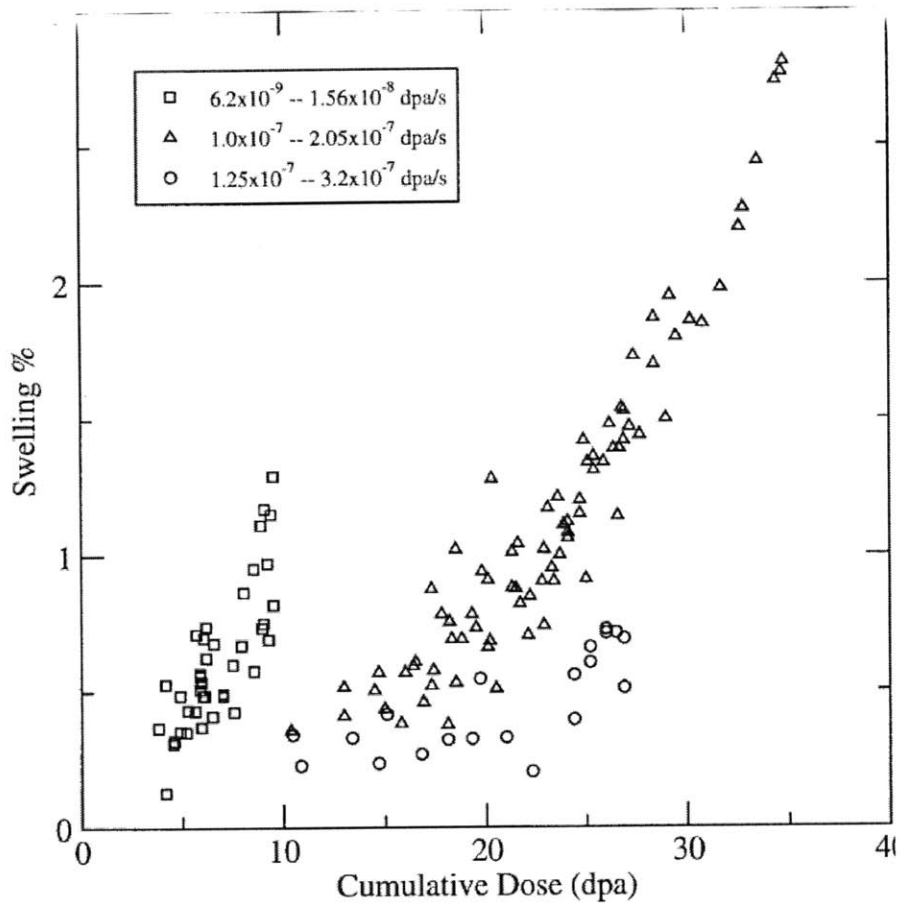

Figure 4-2: Void swelling in solution-annealed 304 stainless steel irradiated in the reflector and blanket regions of EBR-II. Data are grouped according to the dose rates indicated in the legend. The onset of irradiation triggers the formation of small defect clusters but causes very little volumetric expansion. This is followed by an incubation period consisting of void accumulation and growth and accelerating void swelling. This eventually reaches a steady-state swelling regime around 1%/dpa for austenitic steel [92].

- The presences of two competing dislocation Burgers vectors reduces vacancy accumulation at voids.
- Solute trapping of defects leads to increased recombination.
- The dislocation and void evolution produce populations that are not ideal for void swelling optimization in ferritic alloys

In addition to the experimental measurements there is a rich literature discussing

potential models and mechanisms for void swelling. The standard theoretical approach relies upon a combination of rate theories and atomistic, in particular KMC, simulations as exemplified by Surh's work [88, 92] and the references therein. Our calculations in the subsequent sections, although not directly concerned with void swelling, can inform the type of sinks and the interactions with point defects that are used as inputs for these models.

4.2 Effects of Self Interstitial Implantation

While the important role of vacancies and voids in the swelling process has been thoroughly studied, self-interstitial contributions to volumetric expansion are not yet well understood. At high dose rates, small doses, or low temperatures void nucleation and growth are unlikely to be responsible for dimensional changes in the material because the migration barrier for free vacancies is on the order of $0.5 - 0.6$ eV and the concentrations of point defects in the material are low. On the other hand SIAs are known to migrate rapidly and distort their local microstructure considerably. For example, amorphization of crystalline materials has been observed under electron and ion-beam bombardment [94, 95] and appropriately described by considering the self-interstitial driven disorder rather vacancy-mediated effects [96]. This amorphization phenomenon can in turn lead to low density disordered phases which then result in swelling enhancement at high irradiation doses. The formation of such disordered phases in a variety of lattice crystallographies is known to depend strongly on total irradiation dose and dose rate, with aggressive irradiation conditions necessary for full destabilization [95, 96]. Furthermore, the strong long-range interaction between SIAs [94] as well as low energy recoils [95, 97] are known to result in a strong driving force for athermic recrystallization which competes with the formation and growth of disordered phases, and hence also has important effects on macroscopic volumetric instabilities. Therefore dismissing the impact of SIAs in the preincubation region is not necessarily accurate for high dose rate applications.

Non-equilibrium MD simulations were performed in a 10x10x10 bcc Fe super-cell

(2000 atoms) with periodic boundary conditions. We use the recent Fe interatomic potential developed by Ackland et al. [98], which appropriately describes the properties of both crystalline and highly disordered phases essential in our study. The choice of a bcc, rather than fcc, phase of Fe is intentional, as experimental observations described in the previous section indicate that void swelling is significantly lower in ferritic steels, and therefore the effect of SIAs should be more relevant. All MD simulations are performed at a constant temperature of 400 K and zero external pressure. Irradiation conditions are simulated by randomly introducing one or more Fe atoms in octahedral or tetrahedral interstitial sites relative to existing atoms in the lattice. The atoms are introduced in a tetrahedral or octahedral site with equal probability after a fixed number of time steps. While this mechanism represents a significant simplification from the complex recombination dynamics which occur after a displacement cascade, and increases immediate distortion field of the SIA, it provides an adequate platform to study the specific effects of self-interstitial atoms and the resulting dimensional instabilities leading to swelling. Similar simulations of radiation induced amorphization [99] involving both vacancies and interstitials produced similar results to those using self-interstitial insertion only, but under higher total doses and dose rates due to the recombination effect. Each inserted atom is counted as a lattice displacement and therefore the corresponding dose associated to each such insertion is given by:

$$dpa_{insertion}(t) = \frac{n}{N(t)} \tag{4.1}$$

where $N(t)$ is the number of atoms in the simulation cell at the time t of insertion and n is the number of atoms inserted. The total dose is then obtained by adding the doses of all insertions, and the average dose rate is given by dividing the total dose by the time of irradiation. Irradiation conditions for all the simulation runs are given in table 4.1 below. The dose rates explored, ranging from 10^7 to 10^{10} dpa/s, while higher than those for any current reactor or ion beam application, provide insight into the fundamental physics, disorder and defect formation mechanisms associated

Table 4.1: Irradiation Conditions for MD Simulations of SIA-Induced Swelling in Fe.

Simulation Run	Total Number of Inserted Atoms	Irradiation Time (s)	Total Dose (mdpa)	Average Dose Rate (dpa/s)
1	75	7.60×10^{-10}	37.0	4.84×10^{7}
2	75	4.50×10^{-10}	37.0	8.18×10^{7}
3	75	2.25×10^{-10}	37.0	1.64×10^{8}
4	75	1.12×10^{-10}	37.0	3.27×10^{8}
5	75	2.25×10^{-11}	37.0	1.64×10^{9}
6	200	3.00×10^{-11}	95.0	3.18×10^{9}
7	200	1.50×10^{-11}	95.0	6.36×10^{9}

with SIA-induced damage and swelling.

In addition to the non-equilibrium MD simulations, we probed the evolution of the system at longer time scales post-irradiation by using the constant stress ABC method described in Section 2.3.1. In particular, given the nature of the structure, the cell shape relaxation is assumed to be fast relative to the slow relaxation of the atomic positions, and thus we use the formulation of Figure 2.6.a. This is confirmed from the results below. The ABC runs start immediately after irradiation was completed. Therefore since the number of particles in the simulation cells remained constant a static ABC formulation (at constant pressure) is sufficient.

For improved statistical accuracy, multiple MD simulations with different initial configurations for each of the conditions described in Table 4.1 were performed until the integral properties converged. Unless otherwise noted, the results presented below represent averages over these simulations. Post-irradiation microstructural evolution was examined by continuing all the MD simulations up to 2.25 ns.

4.2.1 Macroscopic Effects: Swelling

Figures 4.3 and 4.4 summarize the macroscopic effects of SIA insertion in a bcc Fe lattice for Runs 1 through 5, all with a total dose of 37 mdpa and varying dose rates. Since the number of lattice atoms in the system increases during irradiation, the volume of the material increases to accommodate the increased stresses. Figure 4.3 quantifies this swelling per atom by showing the normalized inverse density ($\nu_{normalized}$) obtained from MD simulations up to 2.25 ns. $\nu_{normalized}$ is defined as

follows:

$$\nu_{normalized}(t) = \frac{\frac{V(t)}{N(t)} - \frac{V(0)}{N(0)}}{\frac{V(t)}{N(t)}} \tag{4.2}$$

where $V(t)$ and $N(t)$ are the volume and number of atoms of the lattice at time t. Hence, $\nu_{normalized}$ represents a measure of swelling per atom as a results of the irradiation. Figure 4.4 summarizes the swelling behavior for the other runs, and Table 4.2 summarizes these swelling levels right after irradiation, and in the short (2.25 ns) and long runs for all the irradiation conditions given in Table 4.1.

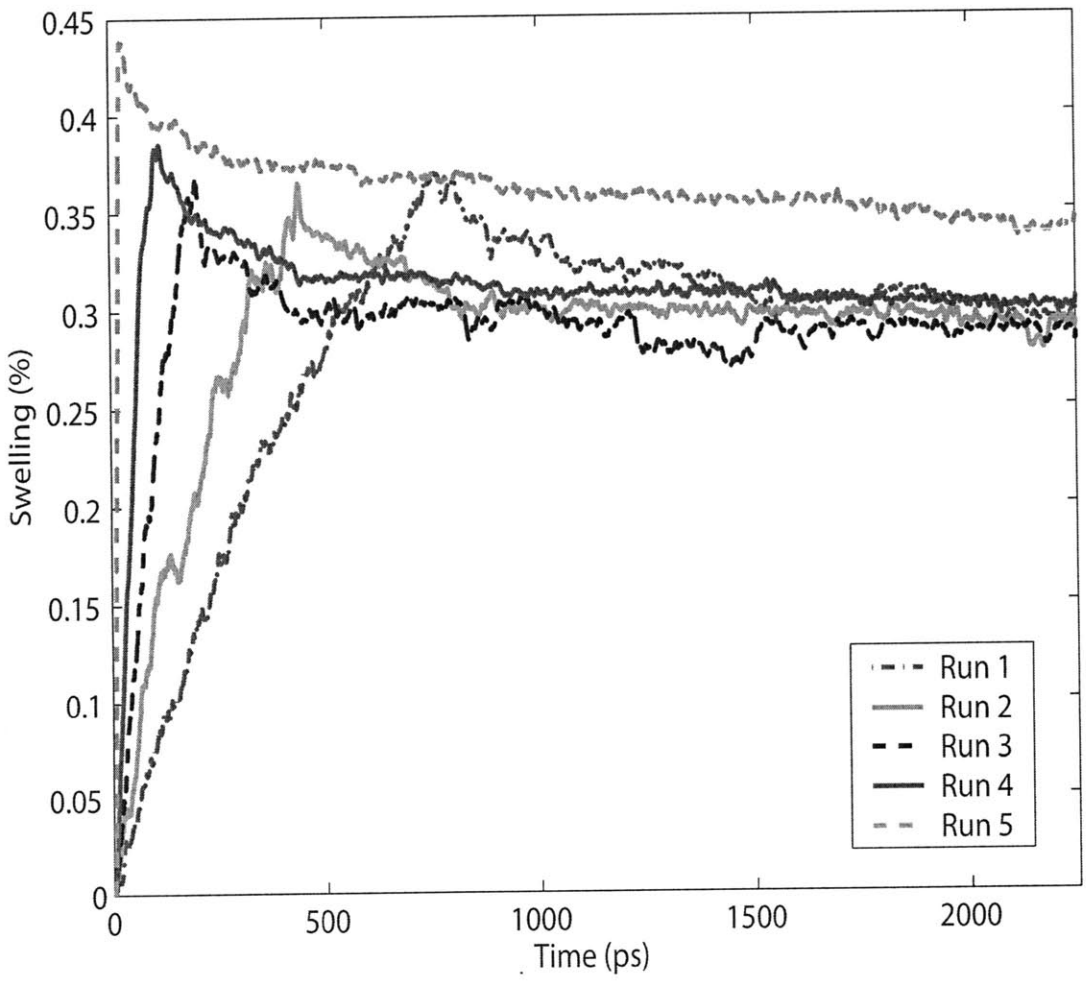

Figure 4-3: Swelling, as measured by the normalized inverse density, as a function of time for various dose rates (Runs 1-5). In all cases the total dose is 37 mdpa) and the total simulated time is 2.25 ns.

Figure 4.3 demonstrates that irradiation, under the aggressive conditions studied in this section, results in an overexpansion of the volume in addition to the relaxation required to accommodate the increased number of atoms in the lattice. At the end of our simulations (2.25 ns) this swelling, as measured by $\nu_{normalized}$, varies over a small range from 0.28% for Run 3 to 0.34% for Run 5 in the range of dose rates explored (at a total dose of 37 mdpa). This in turn corresponds to a swelling rate of approximately 7.7-8.7%/dpa, which is a factor of 8 larger than the $\approx$ 1.0%/dpa observed experimentally in nuclear reactor steels after incubation [92]. On the other hand, those reactor experiments are conducted under dose rates which are orders of magnitude lower and for higher doses than those in this study. As discussed in Section 4.1, in that regime the swelling behavior is believed to be dominated by vacancy-driven processes such as void nucleation and growth [86,88] and not by SIA-driven processes, so the evolution mechanism is different. Our calculations at high dose rates suggest important effects resulting from SIAs in the swelling process which would be relevant for more aggressive conditions such as ion implantation and in the pre-incubation period. In fact, experimental studies of focused ion beam implantation in MgO surfaces [100] are consistent with the features observed in our simulations by exhibiting both an increasing swelling stage followed by recovery as well as a complex defective microstructure including partial amorphization [94]. As discussed in section 4.2.2, such swelling behavior is precisely the result of the evolution of that disordered structure created during irradiation. Our mechanism is then in agreement with the subsurface defect accumulation suggested by Rota et al. [100].

As Figure 4.3 and Table 4.2 show, the effects of dose rate on the total swelling are significant in the short run for the range of conditions studied. Immediately after irradiation the variance is quite large with swelling levels with almost a factor of 2 difference resulting from an order of magnitude increase in the dose rate. This far-from-equilibrium effects are reduced rapidly as the lattice relaxes, and we see significant convergence during the first few nanoseconds. Despite the convergence, the swelling levels exhibit an important trend in which the minimum swelling levels occur at intermediate dose rates rather than at the maximum or minimum dose rates

Table 4.2: Short and long-term SIA-induced swelling at various dose and dose rates in Fe.

Simulation Run	Total Dose (mdpa)	Average Dose Rate (dpa/s)	Swelling After Irradiation (%)	Swelling at t=2.25 ns (%)	Long run swelling (%)
1	37.0	4.84×10^7	0.37	0.30	0.29
2	37.0	8.18×10^7	0.35	0.29	0.29
3	37.0	1.64×10^8	0.33	0.28	0.28
4	37.0	3.27×10^8	0.38	0.30	0.29
5	37.0	1.64×10^9	0.44	0.34	0.33
6	95.0	3.18×10^9	0.78	0.42	0.40
7	95.0	6.36×10^9	0.80	0.39	0.38

explored, i.e., the dependence of the total swelling (in the nanosecond scale) on dose rate is non-monotonic.

Figure 4.5 shows that for the irradiation conditions studied in our simulations, the swelling levels immediately after irradiation are primarily determined by the total dose. Significant recovery takes place within a few nanoseconds and the swelling at higher doses decreases sharply (over a 50% recovery of the swelling for the high doses within picoseconds). This is highly similar to the type of fast recovery observed during the introduction of displacement cascades, though in that instance the recovery is the result of recombination of the Frenkel pairs. In this case an alternative mechanism of recovery takes place as there are no vacancies in the material. This mechanism is described in detail in Section 4.2.2.

The microstructural evolution at long times, probed with ABC (constant pressure) simulations, does not show significant changes to the swelling levels. The system does lower its energy through collective motion and drastic recrystallization after a sufficient number of Gaussian penalty functions (see Figure 4.4 for an example corresponding to Run 2). However, this process requires activation barriers which, for all of the cases explored, surpass 4 eV. At 400 K, our temperature of interest, this relaxation never occurs in practice.

Therefore, most of the recrystallization of the original damage takes place within the first few nanoseconds that can be probed accurately with MD simulations. As

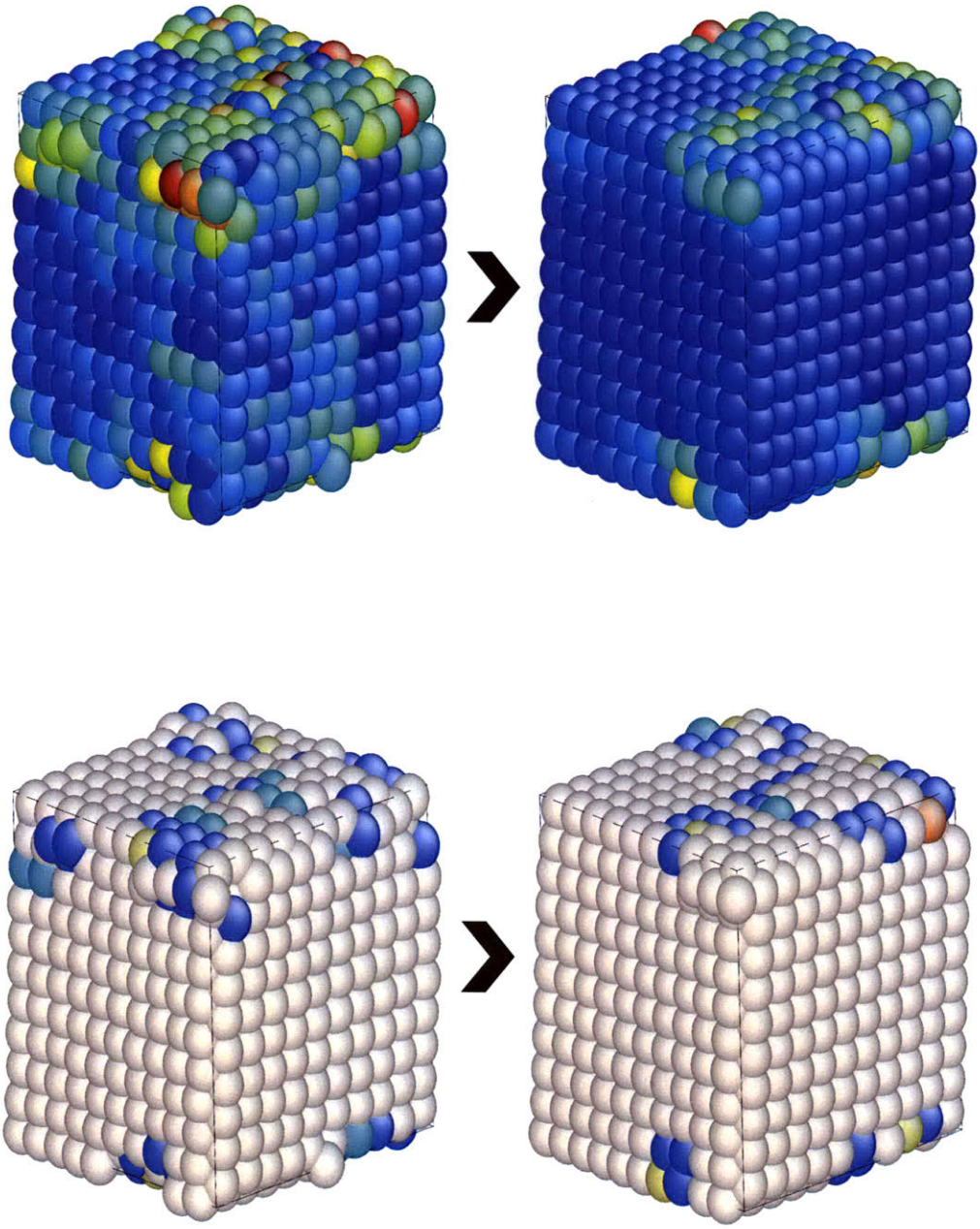

Figure 4-4: Recrystallization of the post-irradiation microstructure in Run 2 as $t \rightarrow \infty$ ($E_{barrier}$ = 5.6 eV). The colors denote local shear strain (top) and coordination number (bottom).

a result, the corrections for long run swelling (as determined by the swelling levels in the ABC runs before the large recrystallization step) are minimal. Additional, intermediate relaxation steps between the high-barrier large recrystallization and the MD-accessible processes could, in principle, be reached with ABC by decreasing the size of the penalty functions. This would enable us to probe processes with barriers lower than 0.5 eV - the size of the penalty functions in this study. The corrections resulting from such an adjustment would be negligible since processes with barriers of approximately $0.3 - 0.5$ eV encompass the migration of SIAs and SIA clusters in Fe (see Appendix D). Given the fact that these represent the primary defects which form during irradiation at the high doses explored in this study, the evolution corresponding to those time scales would be dominated by their diffusion which has negligible effects on swelling recovery.

4.2.2 Microscopic Effects: Disordered Phases and Amorphization

Unlike the void nucleation and growth mechanisms which are responsible for swelling at lower dose rates and high doses (Section 4.1), the mechanism responsible for the swelling observed in Figures 4.3-4.5 is associated with the formation and partial recovery of defected or disordered regions in the lattice. The early evolution of the microstructure during irradiation is dominated by the long-range athermic interactions between SIAs [94], which result in the rapid formation of SIA clusters and localized disorder areas. Figures 4.6-4.8 show the underlying defect cluster distribution and radial distribution function (averaged over both original and implanted iron atoms) for Runs 1 (low dose, low dose rate), 3 (low dose, medium dose rate), and 7 (high dose, high dose rate). A set of atoms if said to comprise a defect cluster if and only if each atom is nearest neighbor of at least one other atom in the group (connectedness) and each atom has a coordination number different than that of a perfect lattice (defectiveness). As can be seen in all three figures, the evolution of the macroscopic swelling under each of the irradiation conditions directly correlates

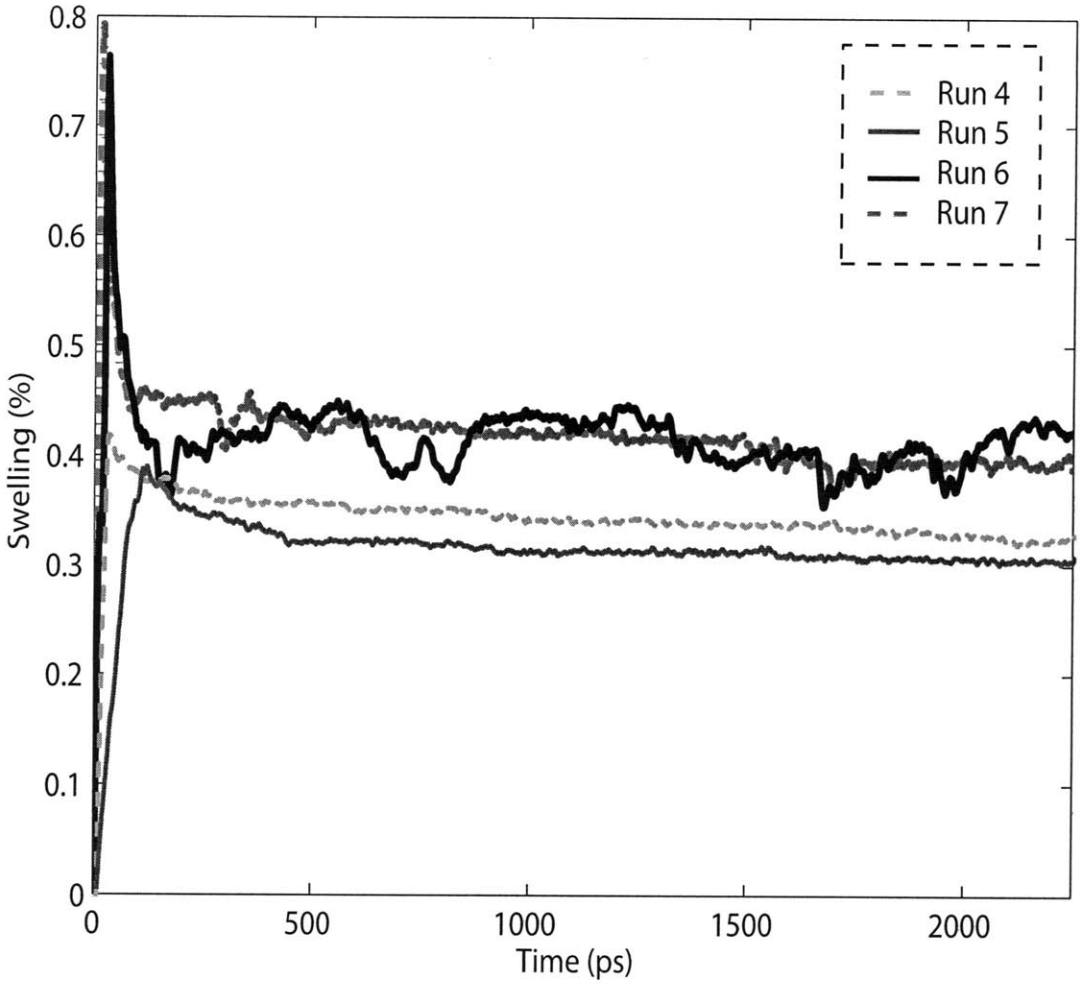

Figure 4-5: Swelling, as measured by the normalized inverse density, as a function of time for various irradiation conditions (Runs 4-7). The total simulated time is 2.25 ns.

with that of the number of miscoordinated atoms in the lattice and the size of the largest cluster. The overexpansion is directly related to the amount of disorder in the lattice; as high disorder regions create excessive local stresses, the lattice relaxes by expanding. The presence of these lower density defect zones destroys some of the short and long range order in the lattice (Figure 4.6-4.8b).

Two main driving forces determine the evolution during irradiation: first, as more atoms are introduced to the lattice the SIA clusters grow in size and complexity. As the lattice relaxes and the volume increases there is also strong driving force for re-

crystallization as the excess atoms in small SIA clusters rearrange themselves into new lattice planes. The competition between these two forces gives rise to a cycle of disorder creation (damage) and recovery which determines the irradiated microstructure and its evolution. The nature of the damage creation and recrystallization process can be observed in the changes in the radial distribution function of Figures 4.6-4.8b. As damage is introduced during the early stages of irradiation (Stage I) the system loses some of its long range order resulting in the disappearance of some of the higher order peaks as well as the reduction in height of the short range ones.

Even though the total amount of disorder added to the system is the main driver of macroscopic swelling (which is not strongly dependent on the dose rate), the recovery mechanism is strongly dependant on the precise irradiation and metallurgical conditions. Differences in the underlying microstructure and their interactions with the large amounts of SIAs give rise to the differences in the swelling levels described in the previous section.

In particular, under these high dose rate conditions, three types of distinct microstructural features characterize the defect populations:

- SIA clusters that relax to the $\langle 111 \rangle$ direction as dislocation loops,
- small (5-10 atoms) pockets of disorder that eventually relax into dislocation loops, and
- larger pockets of amorphous Fe.

Figure 4.9 shows examples of these types of defects as they form during the microstructural evolution of the lattices in Runs 1, 3, and 7. During Stage I, SIA clusters coalesce into small pockets of amorphous phases for all of the irradiation conditions explored. In this early irradiation regime the number and average size of defect clusters increases with the total dose. While the rate of increase is not directly proportional to the dose rate (as can be seen from the initial slopes of the curves in Figures 4.3 and 4.6-4.8), the divergence from this trend is small. This implies that, on average, the microstructure does not relax sufficiently fast during Stage I and therefore the effect of recovery is minor in comparison to damage creation. After irradiation finishes

a)

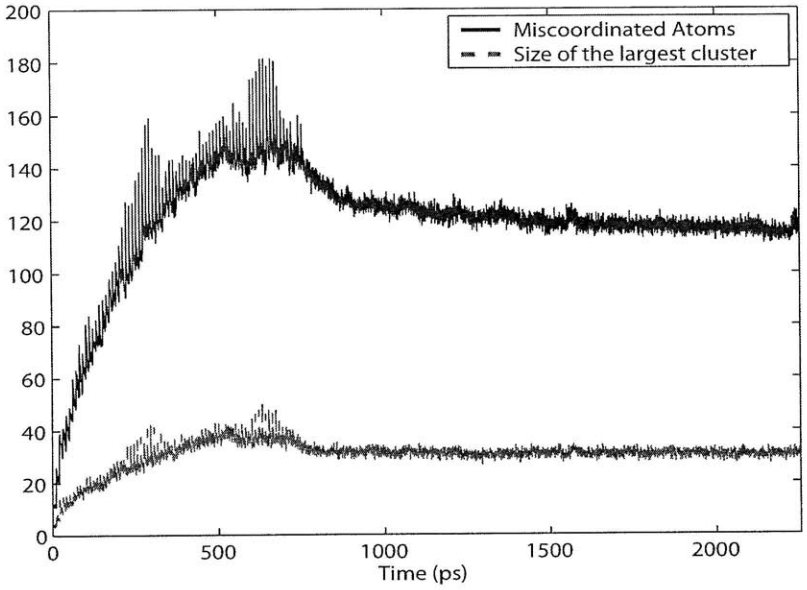

b)

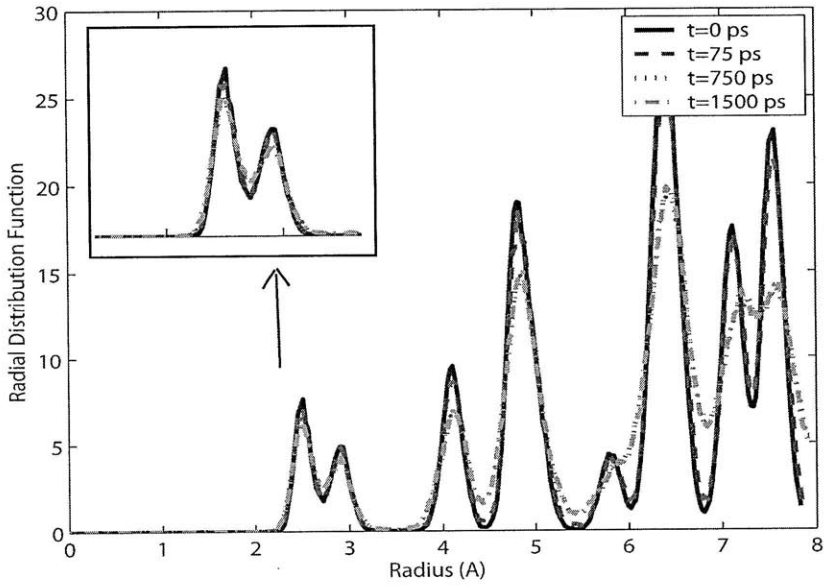

Figure 4-6: Microstructural evolution of SIA-implanted Fe (Run 1): (a) Total amount of disorder (number of miscoordinated atoms) and the size of the largest defect cluster. (b) Radial distribution function (averaged over all iron atoms) as a function of time.

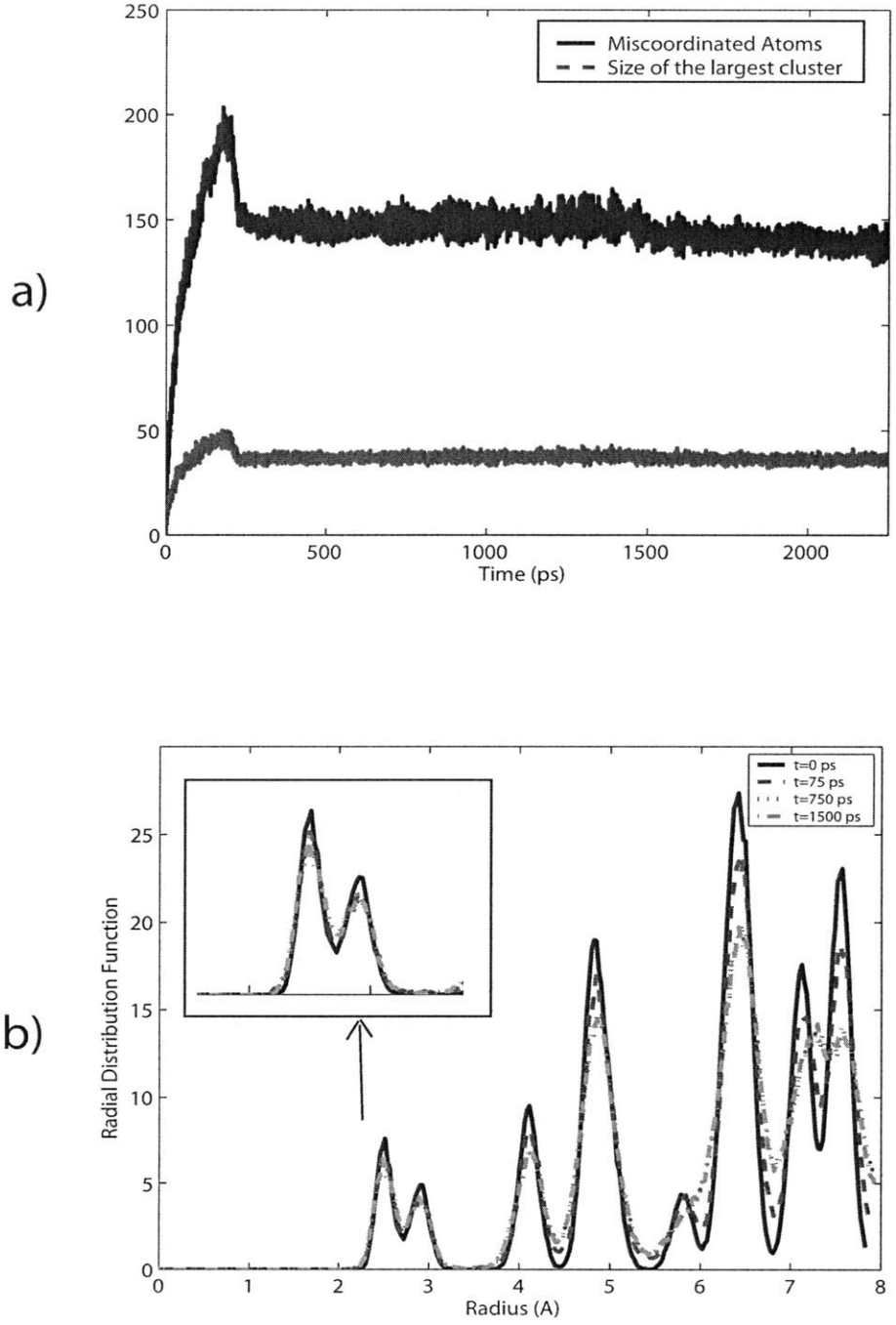

Figure 4-7: Microstructural evolution of SIA-implanted Fe (Run 3): (a) Total amount of disorder (number of miscoordinated atoms) and the size of the largest defect cluster. (b) Radial distribution function (averaged over all iron atoms) as a function of time.

a)

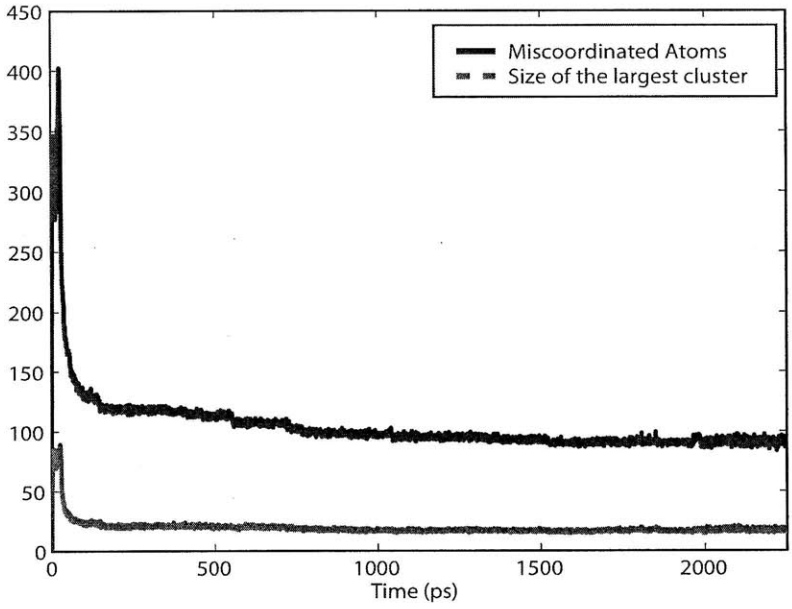

b)

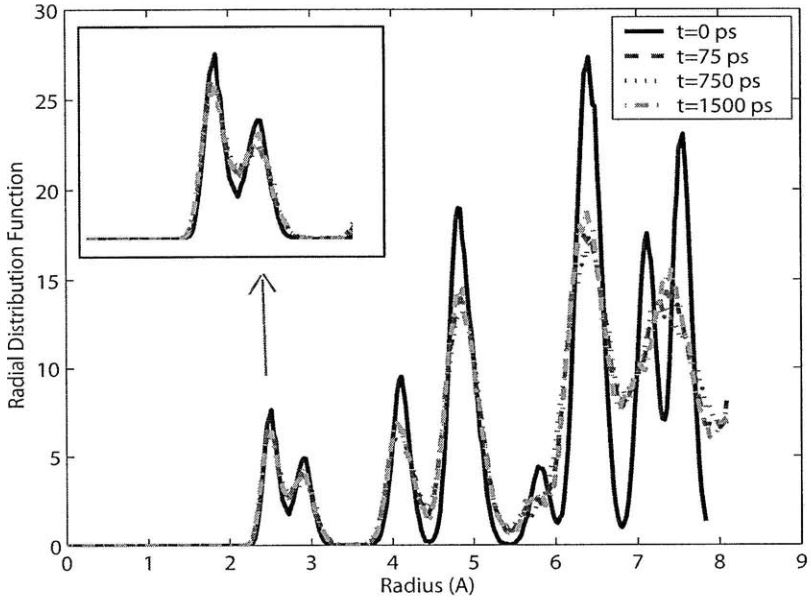

Figure 4-8: Microstructural evolution of SIA-implanted Fe (Run 7): (a) Total amount of disorder (number of miscoordinated atoms) and the size of the largest defect cluster. (b) Radial distribution function (averaged over all iron atoms) as a function of time.

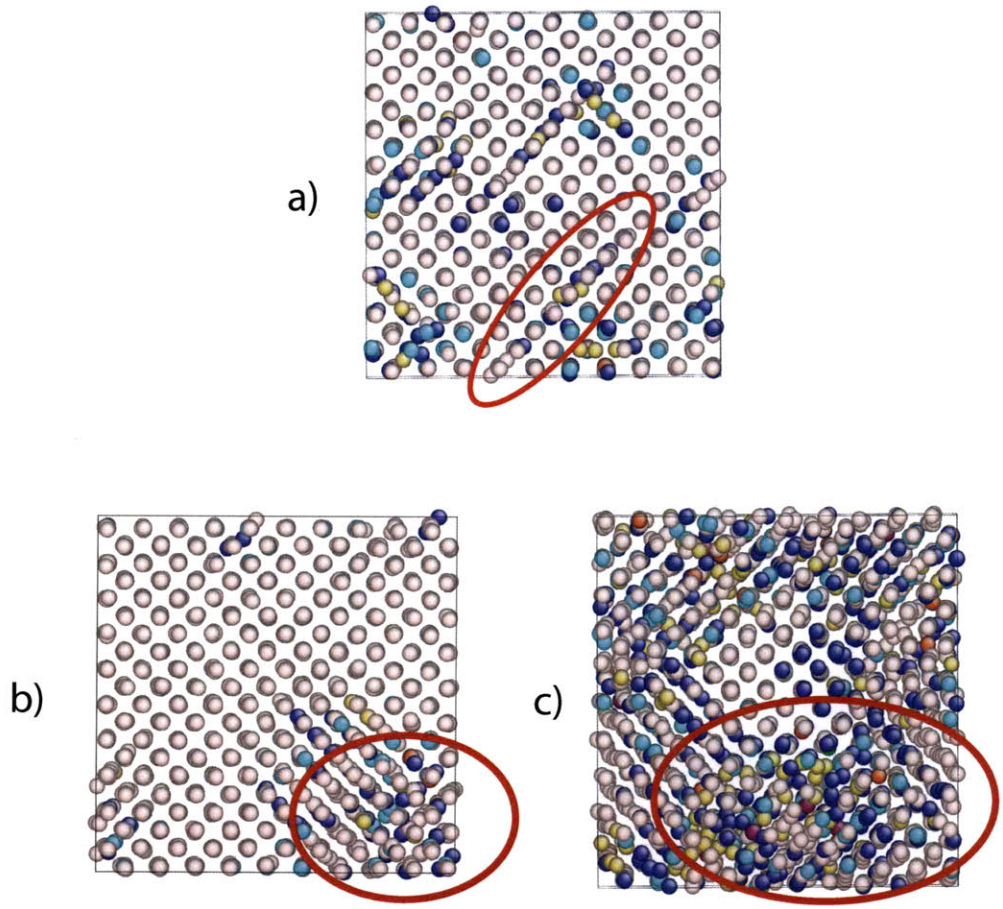

Figure 4-9: Three classes of defects in SIA-implanted Fe at high dose rates: (a) SIA clusters/prismatic dislocation loops (Run 1), (b) small clusters of disorder (Run 3), (c) large amorphous pockets (Run 7). The atoms are colored according to their coordination number.

(Stage II), the defect microstructure formed during irradiation commences to relax and recrystallize. SIA atoms and small clusters quickly coalesce during irradiation due to their low migration barriers. Furthermore, they rapidly transform into small prismatic dislocation loops (Figure 4.9a) which glide rapidly along lattice planes and are highly stable. On the other hand, small disorder pockets (Figure 4.9b) are very unstable and relax into small SIA clusters or simply recrystallize as the lattice expands to accommodate them. Finally, sufficiently large amorphous zones (Figure 4.9c) are also long-lived since they give rise to effective surfaces which need to be eliminated during recrystallization. However, despite being otherwise metastable, large amor-

phous regions are prone to recrystallization because SIAs binding to an amorphous phase (especially during the latter stages of stage I) can act as crystal nucleation sites inside the amorphous pockets.

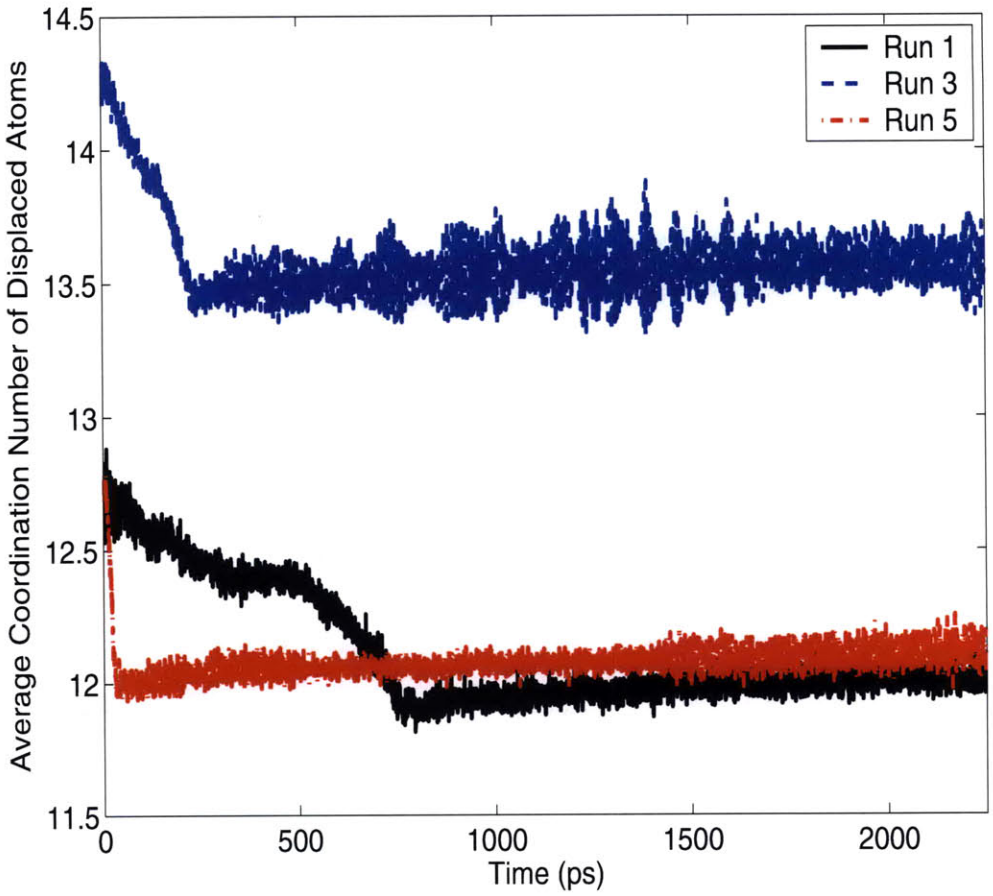

Figure 4-10: Average coordination number of the displaced atoms for Runs 1, 3, and 5 after the first 1 ps. Perfectly coordinated atoms have 14 first and second nearest neighbors.

Figure 4.10 shows the average coordination number (including first and second nearest neighbor shells) of the displaced atoms for Runs 1, 3, and 5. We notice that the intermediate dose rate (Run 3) is characterized by small changes in coordination (from a perfect coordination of 14 - 8 nearest neighbors and 6 second nearest neighbors - to ≈ 13.5), while at high and dose rates we observe more dramatic changes (a reduction of the coordination of the defected atoms to ≈ 12) which are preserved in time. At dose rates below 10^8 dpa/s, newly implanted SIAs can relax to dumbbell positions,

diffuse, and form clusters. These clusters relax to the equilibrium mobile configuration in the ⟨111⟩ direction in the form of small prismatic dislocation loops which migrate through the lattice. As these defects are stable there is little swelling recovery in the long run relative to that shortly after irradiation so the miscoordination is not only more drastic (as all of the dislocation loops have a similar low coordination configuration) but also more persistent.

In contrast, intermediate dose rates are characterized by a combination of SIA clusters and small pockets of disorder. As discussed earlier these configurations are highly unstable so they recrystallize quickly during both stage I and stage II and consequentially the average decrease in coordination is smaller and less persistent. This leads to a lower level of swelling for the same dose. At higher dose rates, the size of the disorder pockets grows until some of then become metastable regions of amorphous material. By reaching a critical size or turning into dislocation loops these large pockets lower the average coordination of the lattice sufficiently (Figure 4.10) to avoid complete recrystallization. At higher doses, newly implanted SIAs can act as nucleating sites inside amorphous regions and foster the recrystallization of the larger pockets, thus explaining the sharp recovery observed in the high dose case.

In summary, the SIA cluster/dislocation loop is the most stable of the defects and prevents full recrystallization. Large amorphous pockets come second because their critical size creates significant interfaces requiring additional energy to recrystallize, so these pockets remain disordered for longer times or transform into SIA clusters/dislocation loops. Finally, small regions of disorder are characterized by small changes to the average coordination (Figure 4.10) as opposed to the sharp decreases in coordination of the other defects. Hence they are highly unstable and rapidly recrystallize. Therefore, and as is characteristic of system with rough energy landscapes, the kinetics of the swelling process are driven by the interactions and stability of the three types of defects, giving rise to three regimes which depend on the total dose and dose rate.

4.3 Slow Dynamics of Radiation Damage

The previous section demonstrated how the introduction of a large number of defects in a perfect lattice gives rise to kinetic mechanisms that act in different time scales. In particular, the difference between the energy barriers for the relaxation and migration of each of the three types of primary defects (SIA clusters/dislocation loops, small disorder clusters, larger amorphous pockets) manifested itself macroscopically in the non-monotonic dependency of swelling on the dose rate.

We also noted that the recrystallization dynamics associated with SIA-implantation and recovery are very similar in both nature and characteristic time scales to the recombination dynamics of a displacement cascade. Furthermore, and as shown in Appendix E, the ABCD method provides a platform for the simulation of systems which traverse time-dependent rough energy landscapes such as those corresponding to materials under irradiation (in which the number of particles in the system varies stochastically and slowly). The combination of these two observation suggests a combined methodology for the simulation of more realistic materials under irradiation, specifically in the case of displacement cascade aging.

Cascade aging represents one of the major challenges in the modeling of slowly evolving systems. The physics that determine the primary production of radiation damage occur when a primary knock-on atom (PKA) produces a displacement cascade upon impact. The cascade a large number of Frenkel pairs. However, within the first few picoseconds most of the damage is healed by recombination and only a fraction of the debris is left. Predicting the evolution of the remaining SIAs and vacancies as well as that of the microstructure with which they interact over time scales of seconds, hours, or even years is the main challenge of modeling cascade aging using atomistic simulations. In practice, these type of simulations are carried out non-rigorously using ad-hoc parameters introduced in a KMC model in which the majority of the short-time physics are treated phenomenologically [91, 101, 102].

As an alternative, we propose a coupled MD/ABCD (constant stress, constant temperature) approach to modeling such materials as follows:

- Starting from some initial configuration begin the irradiation (assuming a realistic dose of rate of $10^{-11} - 10^{-5}$ dpa/s).
- Evolve the system using MD for the first few picoseconds of the cascade to obtain accurate recombination dynamics.
- Start ABCD (constant stress, constant temperature) after the fast relaxation has taken place in order to evolve the system over longer time scales [1].
- Once the time horizon has advanced sufficiently introduce more cascades.
- Iterate.

The main limitation of this approach is the size of the system. While very large MD simulations are possible for a few picoseconds [10], ABC-based methods scale poorly with size. A parallel implementation of ABCD (which would, in principle, require a synchronous algorithm such as the one described in Appendix A for KMC) would be necessary in order to use this approach for sufficiently large systems and model the formation and growth of microstructural features during aging.

[1]The efficacy of ABCD is dependent on the size of the system because of averaging effects over a larger number of atoms. That is, fluctuation effects are, in principle, reduced as the size of the system grows and we average over various quenched runs. Additionally, the accuracy of ABCD is dependent the magnitude of the dose rate, because this determines the speed at which the energy landscape evolves as described in Equation (2.54). These effects are discussed in more detail in Appendix E.

Chapter 5

A Model of Chemomechanical Hardening: Toward Cement Setting

The last physical systems under consideration in this thesis are colloidal suspensions of various densities. Unlike the solid state systems analyzed in Chapters 3 and 4, colloidal suspensions do not have long range crystalline order. Their microstructure transforms from fluid-like at high temperatures, high driving forces, and low densities to glass-like at low temperatures, low driving forces, and high densities, in the neighborhood of the so-called jamming transition. The high level of disorder and heterogeneity in these materials, representing a drastic increase in microstructural complexity from the partially amorphous metals of Chapter 4, gives rise to very rough energy landscapes which in turn result in kinetic behavior which spans a vast range of time scales.

Colloidal suspensions share many features with granular materials and glass forming liquids. In all of these systems the dynamics slow down dramatically to the point in which the system becomes rigid when the temperature is lowered, the driving forces are reduced, or the density of particles is increased. This general phenomenon is known, when temperature is the main driver, as the glass transition, and, when density or perturbations are the key variable, as the jamming transition [103, 104].

Systems exhibiting one or both of these types of behavior are usually characterized by spatially heterogeneous dynamics (SHD) [105] which, on approach to the transition, include correlations in which the particles assemble into one-dimensional strings [106] or aggregate into clusters. Due to this microscopic heterogeneity, particles in a dense colloidal flow have stresses which tend to be unevenly distributed [104], strongly fluctuating, and ill-defined as bulk properties [107]. In particular it has been found that jammed and yielded colloidal and granular materials differ on the statistics of their force networks [108] as do systems under compression and shear forces [109] demonstrating that the boundary conditions on strongly confined colloidal or granular matter have direct effects on the SHD and, in turn, on the puzzling macroscopic properties of the system. Within the context of energy landscapes, a jammed system is trapped in very deep wells in the energy landscape and requires high energy collective motions to relax. While the problem of jamming in both colloidal and granular matter is a very active area of research, and presents many interesting applications to our generalized ABC methods, we only introduce it because of its inherent connection with another problem regarding the mechanics of colloidal suspensions: the problem of setting.

During setting, the microstructure of a colloidal suspension evolves from that of a low viscosity liquid-like suspension to a rigid structures with dynamics similar to those of a solid. This hardening occurs by a combination of jamming and chemical bonding. This *chemomechanical hardening* process, coupling chemical reactions with mechanical behavior on equal footing, poses new challenges not yet addressed my multiscale materials modeling and thus serves as an exacting test of the power and scope of our methodology.

This process of chemomechanical hardening as a function of time is particularly relevant in understanding the mechanisms of cement hydration and setting. Cement slurries represent a unique case study for the understanding of slow dynamics in soft, non-crystalline matter. First, they have tremendous technological importance as they constitute the highest volume man-made material on Earth and form the basis of most modern infrastructure. Second, they possess the type of highly defected

complex microstructure that is difficult to investigate with standard theoretical and computational techniques but amenable to those developed in this thesis.

As described in latter sections the basic phenomena underlying the transformation of liquid cement slurries into solid concrete is a prime example of the interactions between chemistry and mechanics and captures many of the themes of this thesis: very rough energy landscapes, complex evolving microstructures, and slow relaxation times.

5.1 Review: Hydration, Setting, and Hardening of C_3S and C-S-H

In the context of cement science, hydration is a chemical process which leads to the formation of hydrates from an anhydrous material through several reactions. This phenomenon has thermodynamic, kinetic, and structural features which depend on chemical and physical parameters [110]. Furthermore, this process is deeply connected with the phenomenon of setting which transforms the cementitious material from a soft, pourable, and ductile paste to a hard, no longer pourable, and fragile structure. The true microstructure of Portland cement is composed of several mineral phases, the most abundant being an impure tricalcium silicate $3CaO \cdot SiO_2 = C_3S$ (alite) and its dicalcium equivalent $2CaO \cdot SiO_2 = C_2S$ (belite) (See reference [111] for cement chemistry notation). Hence it is common in the literature to refer to simpler model systems, e.g. the C_3S phase only, to gain insight into the mechanisms that drive the microstructural evolution.

Hydration proceeds through three successive reactions which become gradually simultaneous [112]: the dissolution of C_3S providing calcium, silicate, and hydroxide ions in solution; as soon as the supersaturation maximum with respect to C-S-H (see Appendix C for an atomistic model) is reached, it precipitates from silicate ions and a fraction of the calcium and hydroxide ions (the C/S ratio is dependent on the lime concentration in the solution); and as soon as the lime concentration

reaches its supersaturation maximum with respect to calcium hydroxide (portlandite), it precipitates.

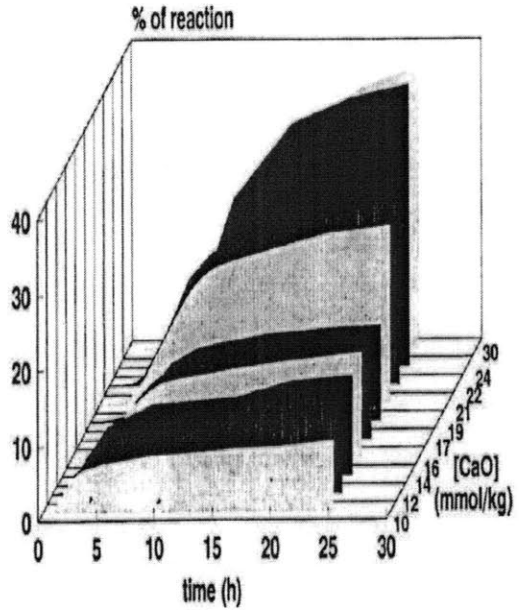

Figure 5-1: Evolution with time of the percentage of hydration of C_3S when the lime concentration in solution is kept constant at different values [110].

Of these three reactions, portlandite precipitation does not appear to be a rate determining process. In fact, the kinetics of hydration are not strongly dependent on the water to cement ratio, and it is even possible to hydrate C_3S completely without any portlandite precipitation. As shown in Figure 5.1. advancement of hydration of C_3S when the lime concentration is fixed at different values follows a sigmoidal shape, which includes an induction period (in which C-S-H presumably nucleates), and a C-S-H growth period, which can be subdivided into an accelerated period, a decelerated picture, and a period with a slow and quasi-constant rate. The nucleation period is very short, lasting only a few minutes at low lime concentrations, and grows longer as the lime concentration in the solution increases. Experimental observations show

that the induction/nucleation period depends essentially on the number of nuclei of C-S-H that are precipitated from the solution in its state of maximum supersaturation with respect to C-S-H. The lower the lime concentration, the greater is the number of nuclei, and the shorter the nucleation period [113]. The rates of hydration during the accelerated and decelerated periods depend little on lime concentration. On the other hand, the percentages of hydration corresponding to the inflection point and the end of the decelerated period are strongly dependent on the lime concentration due to changes in the growing mode of C-S-H on the C_3S surface. The rate of the quasi-content rate period, the longest one, does not appear to depend much on the lime concentration. The reaction rate in this case is limited by diffusion of reactants through the C-S-H layers on the surface of clinker globules and the migration of the C-S-H particles.

The kinetics of hardening are also characterized by a sigmoidal shape in which three clear regimes are observed (Figure 5.2.). The rheological behavior of the material (encompassing both increases in viscosity and shear moduli) comprises two important mechanical events. The first is a simple gelation of the slurry, due to the high ionic strength of the aqueous phase [115–117]. It takes place almost immediately after mixing the cement with water, at almost zero hydration. This coagulated network displays a measurable yield stress for flow, but has a poor mechanical strength overall. The second event is setting which starts a few hours after coagulation. The period between coagulation and setting is called the dormant or inductive period. It is during this stage that the process of C-S-H nucleation and growth by hydration described in the preceding paragraph occurs. A continuous, diffusion controlled reinforcement process occurs at contact areas leading to eventual percolation which increases the shear modulus of the mixture to the GPa range. Further hydration and long term redistribution of matter and voids leads to further hardening over periods of weeks, months, or years [114].

The coagulation/gelation stage is due to attractive forces between particles. These forces may result from interactions of various origins: van der Waals, electrostatic, or solvation forces, though the exact nature of the mechanism for coagulation is not yet

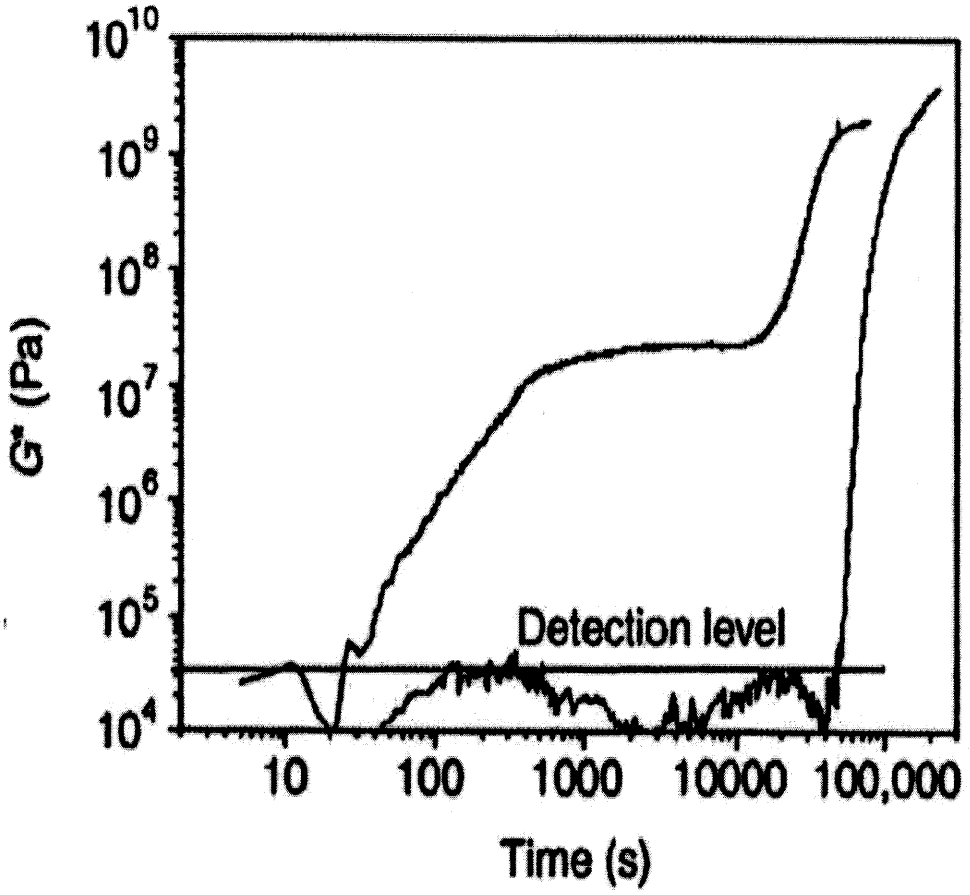

Figure 5-2: Setting and hardening: time evolution of the complex shear modulus of a cement slurry prepared at water/cement=0.80 w/w, without and with addition (0.18% w/w SP/cement) of acrylic superplasticizer (upper and lower curve, respectively). The horizontal line indicates the minimum significant detection level [114].

well understood. This stage is a clear illustration of the sensitivity of cement slurries to the non-contact surface forces important for colloids, leading to shear thinning. As the lime concentration reaches about 10 mmol/l, hardening starts. At this threshold value the solubility of C-S-H in solution becomes very low and it starts to precipitate on the surface of anhydrous grains to bridge particles. Theories about the incubation stage [114, 118] suggest that the after C-S-H starts to precipitate the process becomes transport/diffusion driven giving rise to the slow time scales observed. Finally the clinker phases percolate and the paste hardens.

5.2 Viscoelasticity in Lennard-Jones Colloids

The deformation response of a material to stress depends strongly on the microstructure. The majority of solids exhibit elastic behavior at small stresses and permanent plastic deformation once the stresses surpass a certain threshold or yield stress. In the elastic regime, strain responds immediately and reversibly to applied stress. On the other hand, viscous materials resist shear flow and strain linearly with time (for low shear rates) when a stress is applied. Viscoelastic materials have elements of both of these properties and, as such, exhibit time dependent strain. Whereas elasticity is usually the result of bond stretching along crystallographic planes in an ordered solid, viscosity is the result of the diffusion of atoms or molecules inside an amorphous material

During a short time, known as the *Maxwell relaxation time* [119], after the presence of a shear rate, liquids exhibit solid-like behavior. The system needs this characteristic time to traverse through the modified energy landscape and relax to a flowing equilibrium. In colloidal suspensions, as the system approaches the jamming transition the dynamics of the flow slow down and the Maxwell relaxation time grows, so the system appears solid (in the direction of the flow) at macroscopic time scales. Furthermore, prior to full jamming the system exhibits viscoelasticity over measurable time scales. In parallel to jamming, interacting colloids can manifest setting behavior, in which the microstructural evolution of the colloidal suspension results in a drastic increase of the elastic moduli and (for perfect hardening) the divergence of the Maxwell relaxation time.

Viscosity and elastic moduli are therefore deeply intertwined, and particularly so in colloidal materials that exhibit viscoelastic behavior for appreciable times. More precisely we can formulate Maxwell's insight as follows: basic fluid mechanics shows that at low frequencies the shear stress of a liquid is generated by the Navier-Stokes constitutive relation for a Newtonian fluid [120]. In the case of a fluid undergoing planar Couette flow the flow is defined by a shear strain γ (we assume the colloid flows in the x-direction). This in turn implies that the stress tensor $\mathbf{S}$ must be given

by:

$$\mathbf{S}(\mathbf{r},t) = \begin{pmatrix} p & -\eta\gamma & 0 \\ -\eta\gamma & p & 0 \\ 0 & 0 & 0 \end{pmatrix} \tag{5.1}$$

where η is the shear viscosity and p is the pressure. Therefore we have:

$$S_{xy}(t) = -\eta\gamma(t) \tag{5.2}$$

or in frequency domain:

$$\tilde{S}_{xy}(\omega) = -\eta\tilde{\gamma}(\omega) \tag{5.3}$$

where we use the notation:

$$\tilde{A}(\omega) = \int_0^\infty dt e^{-i\omega t} A(t) \tag{5.4}$$

On the other hand at very high frequencies the material falls within the Maxwell relaxation time, so we have:

$$\tilde{S}_{xy}(\omega) = -G\frac{\partial\tilde{\epsilon}_x}{\partial y} \tag{5.5}$$

where G is the infinite frequency shear modulus. However by definition we have:

$$\frac{d\nabla\epsilon}{dt} = \nabla\mathbf{u} \tag{5.6}$$

where $\mathbf{u}$ is the velocity profile for the flow $\mathbf{u}(\mathbf{r},t) = (u_x, u_y, u_z) = (\gamma y, 0, 0)$. Therefore from Equation (5.5) we have:

$$\tilde{S}_{xy}(\omega) = -\frac{G}{i\omega}\frac{\partial\tilde{u}_x}{\partial y} = \frac{G}{i\omega}\tilde{\gamma}(\omega) \tag{5.7}$$

and combining with Equation (5.3) we find Maxwell's model of viscoelasticity by summing the low and high frequency expressions for the compliances (a general expression

in three dimensions is given in Appendix F):

$$\tilde{\gamma}(\omega) = -(\frac{i\omega}{G} + \frac{1}{\eta})\tilde{S}_{xy}(\omega) \tag{5.8}$$

Therefore in viscoelastic materials strain lags stress by a phase in between 0 and $\pi/2$.

This relationship shows that viscosity and elastic moduli are manifestations of the same "complex modulus", where G represents the amount of energy stored by the perturbed system and ν the loss dissipated via fluctuations (heat). In that sense viscoelasticity is an example of the relationship between externally driven and thermal transport coefficients discussed in Section 2.1.2. In this case the elastic moduli could be interpreted as the correlation factor associated with a stress field while the viscosity represents a dissipative effect that obeys Onsager's hypothesis. A more general theory of linear viscoelasticity in three dimensions is discussed in Appendix F.

5.2.1 Viscosity: Shear Thinning and Thickening

The time-independent relaxation of a viscoelastic material beyond its Maxwell relaxation time is determined by its viscosity (shear and bulk). This behavior falls into three general classes: (1) shear stress is proportional to shear rate (Newtonian fluids), (2) shear stress decreases with shear rate (shear thinning or pseudoplastic fluids), or (3) shear stress increases with shear rate (shear thickening or dilatant fluids). For example, low molecular weight liquids, like water etc. are usually Newtonian. Water borne latex paints are shear thinning, and as discussed earlier wet concrete (during the coagulation stage) is an example of a shear thickening fluid.

The discussion in the previous section suggests several ways to determine the viscosity of these fluids, both through experiments and atomistic simulations. Experimentally, and for suspensions with little inherent elasticity, i.e. short Maxwell relaxation times, it is possible to probe the viscosity by resorting to Equation (5.2) and measuring the velocity profile with a rotating rheometer or another viscometer. However, for materials with significant viscoelastic behavior which relax in very slow time scales the use of a vibrating viscometer for dynamic analysis is more effective

and determines the full complex moduli of Equation (5.8).

The connection between shear relaxation in various regimes and viscosity becomes more apparent from a computational standpoint. In this case we can consider, at least, three different ways for calculating viscosity. Though these methods appear distinct, they are manifestations of the same physical behavior at different time scales.

First, and paralleling the rotating rheometer measurements in Newtonian fluids, we can simulate a system under a constant strain rate via atomistic simulations by imposing the appropriate boundary conditions (e.g., by using pinning points that slide as a function of time - see Section 5.3.1). After reaching a local steady state, this gives rise to a velocity profile in the fluid as well as a steady state shear stress level. Then the ratio between that stress and the shear rate gives us the viscosity η, which we will denote by η_{linear}. This approach is limited by several factors. First, the magnitude of shear rates that can be imposed with standard MD simulations, which is essentially the inverse of the maximum total time that can be simulated imposes a bound on the accessible strain rates higher than $\sim 10^7 s^{-1}$. These strain rates are extreme for most macroscopic applications, and therefore extrapolating the viscosity from such conditions is only valid if the fluid is almost Newtonian (so that the viscosity is independent of shear rate). Second, the stress relaxation time needs to be small enough so that an equilibrium Couette or laminar flow is reached during the MD simulation. Third, the Maxwell relaxation time must be small enough to allow probing of the system's viscosity without the elastic contributions.

When the material exhibits significant viscoelastic behavior violating the third assumption, we can resort to dynamic analysis to estimate the complex modulus of Equation (5.8) by altering the linear strain (i.e. constant strain rate conditions) and instead imposing a sinusoidal strain at the boundaries. This can be achieved by modifying the evolution of the pinning points (described in detail in Section 5.3) to:

$$\mathbf{R}_j(t) = \mathbf{R}_j(0) + L\epsilon \sin(\omega_0 t) e_x \tag{5.9}$$

where ω_0 is a given frequency, and, without loss of generality, we have chosen a

sinusoidal wave in the x-direction. By taking the Fourier-Laplace transform this corresponds to a shear strain at the boundary that satisfies:

$$\tilde{\epsilon}_{xz}(\omega) = \epsilon i\pi(\delta(\omega + \omega_0) - \delta(\omega - \omega_0)) \tag{5.10}$$

We can then consider a fit to the stress response of the system of the form (to first order in the Fourier expansion):

$$\sigma_{xz}(t) = \sigma \sin(\omega_0(t - t_0)) \tag{5.11}$$

or in frequency space:

$$\tilde{\sigma_{xz}}(\omega) = \sigma\pi i e^{-i\omega t_0}(\delta(\omega + \omega_0) - \delta(\omega - \omega_0)) \tag{5.12}$$

and therefore:

$$\tilde{\eta}(\omega) = \frac{\sigma}{\epsilon} e^{-i\omega t_0} \tag{5.13}$$

so:

$$\frac{1}{\tilde{\eta}(\omega)} = \frac{\epsilon}{\sigma}(\cos(\omega t_0) + i \sin(\omega t_0)) \tag{5.14}$$

which is a generalization of Equation (5.8), therefore at low frequencies we find that the delayed response, i.e. imaginary part gives rise to a viscosity of

$$\eta_{oscillatory} = \frac{\sigma}{\epsilon t_0} \tag{5.15}$$

to a first approximation.

While this approach addresses the issue of relevant elastic behavior, at least methodologically, it is only a refinement of the previous approach. The low frequency limit of Equation (5.15) is analogous to the linear estimate for viscosity. It does not address the issues of slow relaxation to steady states or the fact that the rates (in this case, ω_0) which can be used in MD simulations are limited.

The final approach essentially can be considered as taking the dynamic boundary

conditions to the limit of infinitesimal frequency that can no longer be simulated in an MD simulation. In that case the effective strain is given by the thermal fluctuations rather than by the (infinitely slowly changing) field. Roughly speaking $\epsilon t_0 \approx kT$. More precisely we can invoke Onsager's hypothesis for the microstructural relaxation. Then the Green-Kubo fluctuation-dissipation theorem of Equation (2.48), allows us to compute the viscosity from the correlation in the stress field as:

$$\eta_{GK}(T) = \frac{V}{kT}\int_0^\infty d\tau \langle \sigma(t)\sigma(t+\tau)\rangle \tag{5.16}$$

This approach to calculating viscosity has proven very powerful when coupled with activated state dynamic methods such as those described in Chapter 2 [121], especially for extremely long relaxing systems which for which the other methods are not applicable. The only issue with the Green-Kubo approach is that it is difficult to use it to capture changes in the viscosity as a function of shear rate as those emanate from changes in the microstructure of the material rather than from fluctuations. [1]

We use these three approaches to calculate the viscosity of a Lennard-Jones (LJ) colloid. This serves as a benchmark for the methods used for probing viscoelastic behavior in colloids with more complex interactions. Table 5.1. lists the calculated values for the viscosity for both a simple and binary mixture ($c = 0.05$, see Section 5.3 for details), with parameters given in Table 5.2 (See Equation (5.18) in the following section for more details). The viscosity is given in LJ units of $\sqrt{m_A \epsilon_{AA}^{LJ}}(\sigma_{AA}^{LJ})^{-2}$. Additionally the time step is given by $d\tau = 10^{-4}\sigma_{AA}\sqrt{\frac{m_A}{\epsilon_{AA}}}$. As expected the three methods show good agreement in the prediction of viscosity of the simple LJ fluid which is very closely Newtonian, but differ greatly in the dense, binary mixture due to the high strain rates involved in the first two methods and the fact that the binary colloid, with the chosen interactions, is non-Newtonian. Figure 5.3. emphasizes this point by showing both shear thinning and thickening behavior in the binary Lennard Jones colloid, as measured with the linear approach.

[1] Though not addressed in this thesis, this could,in principle, be examined by combining ABCD (changing cell shape) with Li et al.'s Green Kubo network formalism [121].

Table 5.1: Three different calculations of the viscosity of Lennard-Jones colloids

Method	Viscosity (Simple)	Viscosity (Binary)	Notes
Linear	0.13	0.24	$\dot{\gamma} = 10^{-4}/d\tau$
Oscillatory	0.11	0.30	$\omega_0 = 2\pi \times 10^{-4} d\tau$
Green-Kubo	0.12	0.29	

Table 5.2: Parameters for binary Lennard-Jones colloidal model. The simple model uses only the (A) parameters. The temperature (T) and volume fraction (ϕ) are also given.

Parameter X	X_{AA}	X_{AB}	X_{BA}	X_{BB}
ϵ_{LJ}	1.0	0.5	0.5	1.0
σ_{LJ}	2.0	3.0	3.0	2.8
$m_A/m_B = (\sigma_{AA}^{LJ}/\sigma_{BB}^{LJ})^2$	$n_1 = 12$	$n_2 = 6$	$T = 3.0$	$\phi = 1.0$

5.2.2 Shear Modulus

As is the case for viscosity, we can estimate the shear modulus in a variety of ways from experiments, theory, and atomistic simulations. The experimental techniques are similar to those used for the measurement of viscosity: static and dynamic mechanical analysis. Static analysis relies on the engineering definition of stress which is valid at macroscopic scales and, for practical purposes, for solids only. In this case the elastic response of the system is estimated by static loading which gives rise to a strain-stress curve from which we can calculate an effective G as the slope of the elastic regime. The dynamic approach is identical to that described in the previous section in which effective elastic moduli appear as the real part of the complex moduli.

When relying on atomistic simulations the approaches to calculate the elastic moduli in viscoelastic materials, the approaches are similar. Imposing the same constant shear rate boundary conditions discussed above (and explained in more detail in the following section) we can calculate a stress-strain curve from the inception of shear. Rather than measuring the stress after a Couette flow profile is reached we worry precisely about the opposite, that is, the response of the system before the material starts flowing. This approach is only valid if Maxwell relaxation times is long enough and the strain rate low enough that there is an appreciable elastic regime

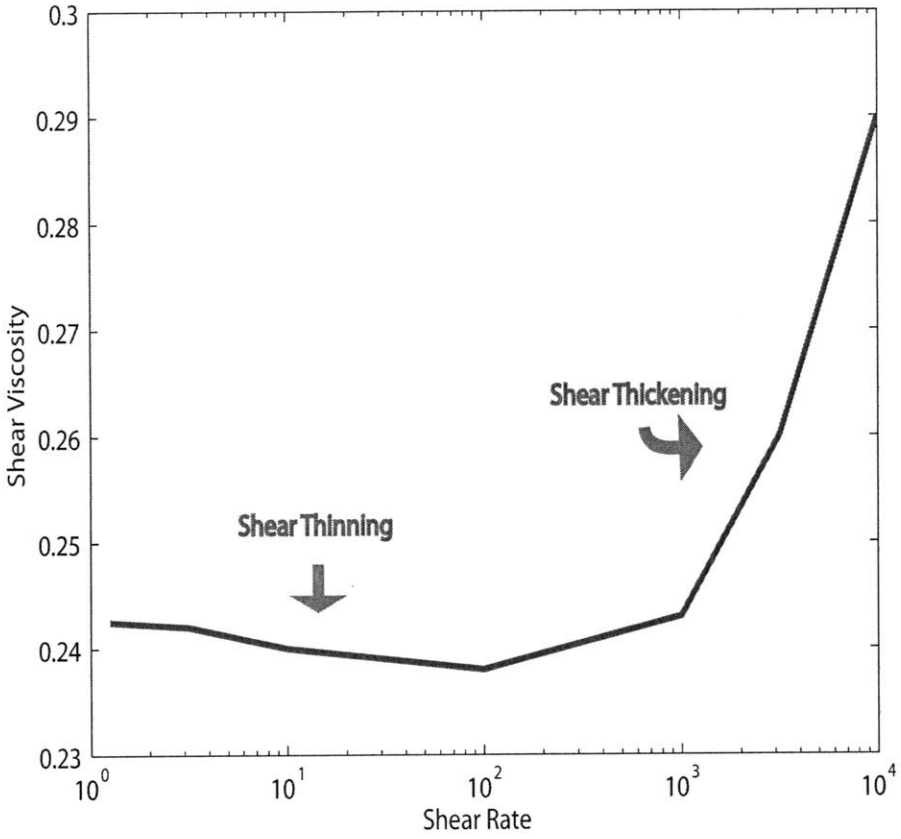

Figure 5-3: Shear viscosity as a function of shear rate for a dense binary colloid. We can observe both shear thinning and thickening behavior.

before viscosity effects dominate. As a result pure viscous fluids are not amenable for such an approach (just as solids are not amenable to viscosity calculations). Colloidal suspensions, on the other hand have measurable Maxwell relaxation times due to their highly viscoelastic nature and can produce stress-strain curves from which we measure the shear modulus as the slope G_{linear}. For aging colloidal suspensions such as the ones we are concerned with in this chapter, the system's stress response can "move in the viscoelastic space" by increasing the elastic contributions at the expense of the viscous dissipative effects. It is precisely this phenomena what we call setting and hardening. For an aging material we allow the microstructure to evolve without external stresses. At each time t we take a snapshot of the aged configuration and

relax until the temperature equilibrates. We then calculate the shear moduli as $G(t)$ by repeating the procedure described above - constructing an effective stress/strain response curve until flow. In this way we generate effective stress/strain curves at each time t from which we can then calculate effective shear moduli. [2].

The second approach to calculating the shear rate is by taking the real part of Equation (5.14) under the same oscillatory boundary conditions. However in order to probe the elastic regime we look at the high frequency limit. In practice, this reduces to observing the response of very small oscillatory shear on the stress. However, if the frequency is high we can assume that t_0, i.e. the lag, is small by comparison, so to first order the infinite shear modulus is simply given by:

$$G(\omega \to \infty) = \frac{\sigma \sin(\omega_0(t - t_0))}{\epsilon \sin(\omega_0 t)} \approx \frac{\sigma}{\epsilon} \tag{5.17}$$

which results in the same linear estimate as that in the stress strain curve if the Maxwell relaxation time is sufficiently long.

A Green-Kubo approach to calculating shear moduli is not possible since by definition the elastic moduli correspond to the high frequency modes of the stress response, while the Green-Kubo fluctuation-dissipation theorem results from Onsager's hypothesis of low frequency modes. A perturbative approach based on the interpretation of the shear as a rapidly changing, small field, and within the context of the externally driven transport coefficients of Equation (2.59), is possible since the corresponding fluctuation-dissipation theorem does not invoke the Onsager assumption. In this case (taking $X = \sigma_{xy}$ as stress and $F = \epsilon_{xy}$ as strain, and all the other changes as negligible), Equation (2.52) becomes:

$$\mathcal{H} = \mathcal{H}_0 + H_{\epsilon\sigma}\sigma_{xy}\epsilon_{xy} \tag{5.18}$$

[2]It is important to note that there are two characteristic time scales when determining elastic moduli of aging viscoelastic materials. First, there is an inherent relaxation time associated with the microstructural evolution as the material ages. In addition, there is the Maxwell relaxation time which determines the system's characteristic relaxation time as it relaxes under stress by first behaving elastically and then viscously. Experimental and theoretical approaches to calculating effective stress relaxation coefficients make the assumption that the aging relaxation time is much larger than the Maxwell relaxation time to ensure that the measurements are consistent with a local equilibrium microstructure.

Under this simple interpretation Equation (2.59) then reduces to:

$$G \propto H_{\epsilon\sigma} \tag{5.19}$$

which is simply a reformulation of the very basic fact that the elastic moduli can be computed from the second derivatives of the Hamiltonian near an equilibrium. In the infinite frequency limit, this approach is therefore also equivalent to the two previous formalisms.

For the calculations that follow we use the linear approach to calculating the shear modulus, i.e. as the linear response of stress to strain before the Maxwell relaxation time or the slope of the stress-strain curves in which we ensure the microstructure relaxation is slower than the Maxwell relaxation time so our calculations have a precise physical interpretations. Under the conditions that we explore in the following section this approach is consistent with other experimental and theoretical ways of estimating the shear moduli in aging viscoelastic materials at the infinity frequency limit in which we can objectively compare the physical meaning of the stress response. While non-linear effects play an important role in viscoelastic materials, and characterizing such systems by a single transport coefficient may not be appropriate, at the infinite frequency limit we can objectively ignore the non-linear aspect of the response and rely on the approaches described in this and the previous section as well as theory of linear viscoelasticity discussed in Appendix E.

5.3 Dynamics of Colloidal Setting

Unlike glasses, which are widely considered solids for most applications, the concept of rigidity is traditionally explored in colloidal systems only in the neighborhood of the jamming transition and not when the system dynamics remain less frustrated. Nonetheless, for many colloidal systems (most notably cement slurries) the system evolution is such that shear moduli can be measured rigorously even when the system is not in a jammed state [114]. In these cases the colloidal suspension can be modeled

as a viscoelastic material and the deformation responses to stress can be calculated using the methods described in the previous section.

In this section we construct an interacting binary colloidal model that exhibits such chemomechanical hardening and can be probed with atomistic simulations. This model simulates an aging viscoelastic material which, naturally, evolves slowly. In order to probe its viscoelastic behavior with MD simulations we increase the temperatures to overcome the rate limitations. However, this occurs at the expense of a fully detailed microstructural picture of the low temperature evolution. At the end of the section we discuss how we can investigate the model under more realistic conditions by relying on ABC.

5.3.1 Binary Sticky Colloidal Model

Our model is informed from the experimental observations of Section 5.1 which suggest that three essential kinetic mechanisms must be captured: gelation, transport, and percolation. With this physical perspective as background we develop a simple model of the statistical mechanics of setting as follows:

The model consists of a binary mixture with sticky interactions similar to those proposed by Emanuela Del Gado [122] for network forming colloids. Instead of incorporating the full chemical effects associated with the cement grain microstructure we drastically coarse grain the system by assuming that the systems interact via short range potential functions [3] given by:

$$V_{\alpha\beta}(r_{ij}) = V_{\alpha\beta}^{LJ}(r_{ij}) + V_{\alpha\beta}^{D}(r_{ij}) \tag{5.20}$$

[3]The assumption of a short-range potential to model an (at least partially) ionic system such as cement is a strong one, and could have an important effect in the type of transport phenomena observed in addition to the strengthening of the chemical bonds between particles at short range. Our assumption is equivalent to assuming that the dielectric constant of the solvent is extremely high and screens the long range nature of the interactions. Exploring the effects of this assumption will be a topic for future studies.

Table 5.3: Parameters for "sticky" binary colloidal model

Parameter X	X_{AA}	X_{AB}	X_{BA}	X_{BB}
ϵ_{LJ}	1.0	0.5	0.5	2.5
σ_{LJ}	2.0	3.2	3.2	2.8
ϵ_D	0.0	0.1	0.1	0.5
σ_D	0.4	0.6	0.6	1.0
d	0.43	0.43	0.43	0.53
	$n_1 = 18$	$n_2 = 10$	$n_3 = 12$	$n_4 = 8$

where:

$$V_{\alpha\beta}^{LJ}(r_{ij}) = \epsilon_{\alpha\beta}^{LJ}((\frac{\sigma_{\alpha\beta}^{LJ}}{r_{ij}})^{n_1} - (\frac{\sigma_{\alpha\beta}^{LJ}}{r_{ij}})^{n_2}) \tag{5.21}$$

$$V_{\alpha\beta}^{D}(r_{ij}) = \epsilon_{\alpha\beta}^{D}(\frac{\sigma_{\alpha\beta}^{D}}{r_{ij}})^{n_3}[(\sum_{p}(1 - \frac{1}{1 + f(\mathbf{r}_i - \mathbf{r}_{jp})}) - 11) + (\sum_{p'}(1 - \frac{1}{1 + f(\mathbf{r}_j - \mathbf{r}_{ip'})}) - 11)] \tag{5.22}$$

with

$$f(\mathbf{r}_i - \mathbf{r}_{jp}) = (\frac{|\mathbf{r}_i - \mathbf{r}_{jp}|^2}{d_{\alpha\beta}^2})^{n_4} \tag{5.23}$$

where $\mathbf{r}_i$ is the position of i, $\mathbf{r}_{ip}$ is the position of the point p corresponding to particle i which is a vertex of the icosahedron circumscribed in a sphere with center $\mathbf{r}_i$ and radius $\sigma_{\alpha\beta}^D$, and the sum over p goes over all twelve vertices of that icosahedron. α and β denote the type of particle for i and j respectively, i.e. solvent (A) or solute (B) particles. All the parameters used in the model are given in Table 5.1 below, and the Lennard-Jones part of the potential is truncated at a radius of $2.5\sigma_{\alpha\beta}$ in all cases. With this construction, if any of the vertices on the icosahedron corresponding to particle j is within a distance from the center of i small relative to $d_{\alpha\beta}$ then $V_{\alpha\beta}^D = 0$ and the sticky soft sphere repulsion has no contribution. In case the distance is larger, we have $V_{\alpha\beta}^D = 2\epsilon_{\alpha\beta}^D(\frac{\sigma_{\alpha\beta}^D}{r_{ij}})^{n_3}$ which reduces the attraction from the Lennard-Jones potential.

Our simulations are performed starting with a random mixture of small A and

large B particles such that, on average, the composition of the larger particles is equal to $c < 1$. That is, the type of each particle is chosen stochastically such that:

$$\mathbb{E}[\frac{N_B}{N_A + N_B}] = c \tag{5.24}$$

The masses for the particles are chosen such that $m_A/m_B = 2(\sigma_{AA}^{LJ}/\sigma_{BB}^{LJ})^3$. The

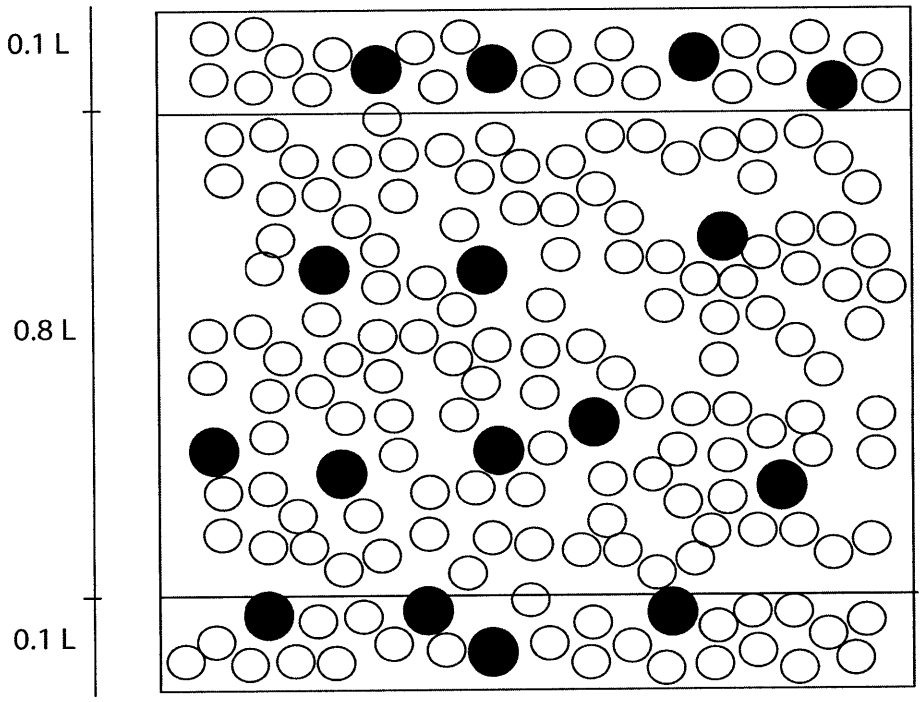

Figure 5-4: Schematic of the boundary conditions for the sheared colloidal flow MD simulations. B particles (dark) are suspended in a fluid of A particles (light).

system is then equilibrated at low temperature and divided into three regions: two boundary layers and a bulk region as shown in Figure 5.4. A shear rate is imposed on the system by using the fluid boundary conditions given by Shiba [123] attaching the particles in the boundary layers to chosen pining points via the spring potential,

$$u_j(\mathbf{r}_j - \mathbf{R}_j) = \frac{1}{2}K|\mathbf{r}_j - \mathbf{R}_j|^2 \tag{5.25}$$

where the spring constant is given by $K = 0.10\epsilon_{AA}^{LJ}(\sigma_{AA}^{LJ})^{-1}$. The boundary particles interact with the bulk particles through the potential described previously but expe-

rience an additional force as a result of the spring potential. The pinning points are given by:

$$\mathbf{R}_j(t) = \mathbf{R}_j(0) \pm \frac{1}{2} L\dot{\gamma} t \mathbf{e}_x \tag{5.26}$$

where the sign depends on whether we are in the top or bottom layer, and $\mathbf{R}_j(0)$ are the positions of the boundary particles after the low temperature equilibration. With these conditions we effectively drag the atoms in the top layer in the x-direction with velocity $\frac{1}{2}L\dot{\gamma}$ and those in the bottom layer with velocity $-\frac{1}{2}L\dot{\gamma}$, which imposes a shear flow of rate $\dot{\gamma}$. These type of boundary conditions represent an intermediate point between a completely rigid boundary ($K = \infty$) and no boundary drag ($K = 0$). Other alternatives for the boundary conditions, which provide better accuracy for very high shear rates, are the DOLLS [124] or SLLOD [125] fluid boundaries in which fictitious forces are introduced to the equations of motion of the particles producing either a laminar or Couette flow profile. However, in the regime of shear rates explored the system remains close to local equilibria and therefore any errors introduced by the Shiba boundary conditions can be neglected. The particles are attached to a Nosé-Hoover [24] thermostat with relaxation time $\tau_{NH} = 0.02\tau$, where $\tau = \sigma_{AA}^{LJ}\sqrt{m_A/\epsilon_{AA}^{LJ}}$ is the characteristic LJ time. The integration time step is given by 0.001τ. Hereafter, we measure all properties in Lennard-Jones units, that is in units of σ_{AA}^{LJ} for length, τ for time, τ^{-1} for shear rate, ϵ_{AA}^{LJ} for energy, $\epsilon_{AA}^{LJ}(\sigma_{AA}^{LJ})^{-3}$ for shear stress, $\sqrt{m_A\epsilon_{AA}^{LJ}}(\sigma_{AA}^{LJ})^{-2}$ for viscosity, and $\epsilon(\sigma_{AA}^{LJ})^{-4}$ for shear modulus.

Our MD simulations are started at a low volume fraction of $\phi = 0.45$ and temperature $T = 1.5$, the volume is then allowed to relax at zero pressure up to a volume fraction of $\phi \sim 0.6$, after which we continue the simulation at a fixed volume. We calculate the shear modulus at various stages in the evolution of the system by using the linear procedure described in the previous section, that is, by fitting the slope of a stress-strain curve in the elastic regime realized by shearing the system at a rate of $\dot{\gamma} = 1$ with the boundary conditions described above. The simulations are performed at high temperature to artificially accelerate the kinetics of setting. A more realistic approach, briefly explored in the last section of this chapter, resorts to the ABC

method to study the slow evolution at lower temperatures.

5.3.2 Colloidal Setting

The results of our setting simulations are summarized in Figure 5.5. Our simple binary colloidal model is able to replicate the sigmoid, three-regime behavior observed during cement setting. The evolution at the atomistic scale can be observed in Figure 5.6. In addition, Figure 5.7 shows the evolution of the connectedness of the B particles as a function of time (determined using the same definition as for the SIA clusters in Section 4.2.2) as well as the evolution of the radial distribution function (RDF) during the first stage.

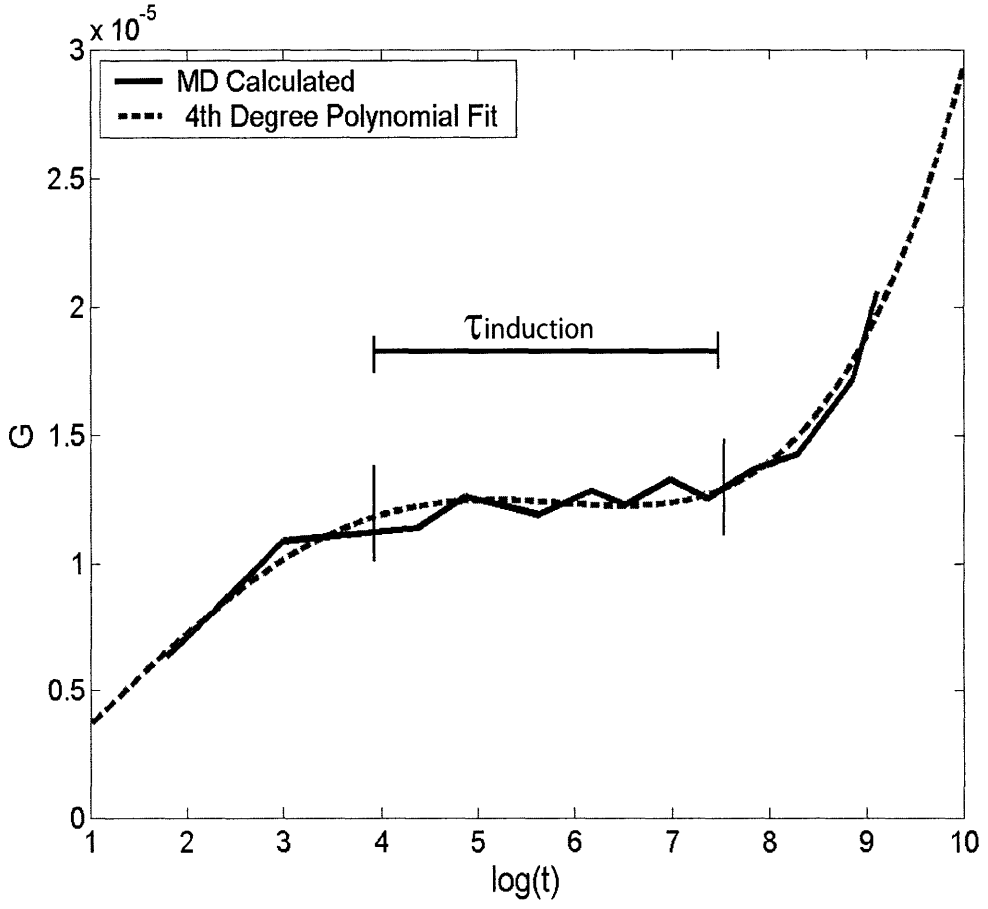

Figure 5-5: Colloidal setting: shear modulus as a function of time in our binary colloidal suspension. $\tau_{induction}$ denotes the length of the induction or incubation stage.

During the initial stage of solidification the A particles, greatly outnumbering the larger and significantly heavier B particles, rapidly bind into a connected colloidal suspension or soft gel, defined as a substantially dilute linked system which exhibits no flow at steady-state, (Figure 5.6.a-b). This is evidenced by the increase in density of the system due to the attractive AA interactions and the associated increase of short range order as evidenced by the growth in the first peak of the RDF around $r = 2.0$ (Figure 5.7a), which is the characteristic separation of the A particles. The gelation or coagulation stage results in an initial increase of the shear modulus of the system. After this stage - dominated by the short range attraction between A particles - concludes, the system microstructure does not show any appreciable changes, and enters the so-called incubation or induction stage. The rate limiting process is then the diffusion of the B particles, which favor clustering together, through the soft gel formed by the A particles (Figure 5.6c-d and Figure 5.7b). Many parameters control the length of the induction stage $\tau_{induction}$ (which we define by fitting a fourth-order polynomial to our setting curve and taking the inflection points as the endpoints of the induction period) including the concentration and mass of B particles, the system temperature, and the relative strength of the AB and BB bonds. This stage of solidification is characterized by a relatively invariant shear modulus as no new rigid structures form while the B particles diffuse through the A-gel. Finally, after a sufficient number of B particles cluster together, they percolate as indicated by the rapid increase in the size of the connected B particle network, a necessary condition, (Figure 5.7b) and the fact that this B particle network goes from side to side in the unit cell (Figure 5.6e). The material then hardens rapidly due to formation of the strong BB bonds.

The transition from a gelation-driven to a transport-driven to a percolation-driven kinetic mechanism highlights the complexity of the associated energy landscape in the setting problem. In this case the system transitions from regions with differently sized barriers which give rise to the separation of time scales. In particular we can interpret the gelation stage as an initial period of relaxation in an area of shallow energy wells. After some of the local minima have been sampled and the B particles diffuse the

macrostate migrates to rougher areas of the energy landscape until a large barrier for collective motion, giving rise to percolation, is overcome. In this sense the problem clearly exhibits the connection between energy landscapes and multiple time scales in a simple physical system. Furthermore, a single phase system (i.e. only A or only B particles) gives rise to only the initial gelation stage after which the system reaches a steady state with a fixed shear modulus rather than the three regime behavior, highlighting the important effect of the two phases and their interactions.

Based on the microstructural evolution mechanism proposed above we associate, to a first order approximation, the A solvent particles with the water-ion/nucleating C-S-H mixture which forms shortly after the dissolution of the cement powder, and the B particles with the larger C-S-H coated clinker phases which nucleate during the hydration process, grow, and bind together. This is similar to Jennings' colloidal models (for the C-S-H clinker phase rather than the full cement paste) in which large globules of C-S-H (with, perhaps, a metastable layer surrounding them) diffuse in a solvent of ions and smaller C-S-H particles [126–128]. With this postulate, we can compare some experimental observation in cement pastes with the predictions of our coarse grained model.

First, we analyze the effects of the relative concentration of B on the induction time. Figure 5.8 summarizes our results. We notice a dramatic decrease in the induction time with increasing B concentration. This is intuitive and follows from our proposed hardening mechanism. Since the rate limiting step during the induction stage is the diffusion of B particles toward each other, the induction time is proportional to the average distance between particles. This distance is given by:

$$\langle d_{BB} \rangle = (\frac{V}{N_B})^{1/3} = (\frac{V}{cN})^{1/3} = (\frac{1}{\phi}((\sigma_{BB}^{LJ})^3 + (\frac{1}{c} - 1)(\sigma_{AA}^{LJ})^3))^{1/3} \tag{5.27}$$

Therefore as c increases, d_{BB} decreases, as does the induction time $\tau_{induction}$. Given the correspondence between our model and cement slurries, in which the B particles can be identified as surrogates for C-S-H, these results becomes consistent with experimental observations by Nonat summarized in Section 5.1 [110] and by Alizadeh [129]

in which the induction time decreases with increased C-S-H concentration in the slurry.

The mass and size of the B particles affect the induction time in the opposite direction as their concentration (Figure 5.9). A higher mass (or size, since we keep the density of the particles constant in the model) results in slower particle diffusivity, because the frequency of jumps in the energy landscape (ν in Section 2.1.1) decreases. This in turn extends the induction time needed for percolation as long as the average separation between particles is kept constant. This does not hold true if we increase the size of the B particles but not their mass, making them less dense, in this case the diffusivity remains unchanged to first order (there are small size effects associated with neighbor relaxation but they are small at high temperatures), but as we keep the volume fraction constant it would increase the average separation of the particles and lengthen the induction stage. This final point is not of major concern since the assumption of constant volume fraction can be relaxed with no repercussion to our other conclusions, in which case the increase in size (even without an associated increase in mass) reduces the diffusivity, the average separation between particle remains constant, and the induction time increases. In this case the comparison with experiments is more difficult since our simple model does not account for the formation of a metastable porous layer around already percolated clusters which hinders the diffusion of additional agents, but it suggests additional experimental avenues of research.

5.3.3 Cement Setting and Stress Corrosion Cracking: An Analogy

The binary sticky model of cement setting described in the previous section gives rise to the characteristic three-regime behavior from very simple interactions. The fact that such a simple model with short-range Lennard-Jones interactions enhanced with a directional sticky term is able to capture the cement setting curve with little information on chemistry reveals that the basic processes leading to chemomechanical

hardening require, at least, a two phase heterogeneous mixture.

The precise nature of chemomechanical hardening is certainly dependent on the specific chemistry and the exact interactions of the particles. In the case of a more realistic model of cement, these interactions are highly complex and must be derived from fundamental studies of the electronic and atomistic structure of the slurry such as Pellenq's model discussed in Appendix C [131]. While our current model does not capture any such chemistry, a discussion of possible refinements to our model is given at the end of the next section. Nonetheless, the qualitative behavior of coagulation/gelation, transport, and percolation is a testament to the universality of the setting behavior and how the coupling of chemical interactions with mechanics gives rise to complex behavior even at a very coarse grained scale.

Moreover, we encounter the same three regime behavior in a variety of problems which are, at least superficially, quite distinct from cement setting, such as polymerization of monomers [132] and the gelation of organic compounds [133]. Another such instance is the well documented case of stress corrosion cracking (SCC). Figure 5.9 [130] shows an schematic of the velocity of a crack tip during a SCC event in a glass as a function of applied external stresses. The resemblance with Figure 5.2 in this, seemingly, completely unrelated problem is striking. However, we can use the framework from our model to aide us in interpreting the three kinetic stages in the SCC problem. At low stresses, the kinetics of the system are governed by the interaction of corroding agents with the crack tip which give rise to the initial stage of propagation. Shortly after the corroding agents are exhausted at the tip as they bind to the forming surfaces (possibly forming a protective layer for some materials). The system then enters a transport driven stage in which the corroding agents need time to diffuse to the tip of the crack from the solution, this process is slightly dependent on stress as the solid state diffusion is minorly enhanced. Once the stress at the crack tip reaches a critical level, the mechanical forces dominate the chemical ones and the crack tip propagates by stress driven bond breaking.

From the perspective of our model we can once again consider the three basic SCC processes (chemical attack at the tip, diffusion of corroding agents, and stress driven

bond breaking) from the perspective of interactions between two types of (virtual) particles: the A particles are the corroding agents in the neighborhood of the crack tip, and the B particles serve as a coarse-graining of two distinct elements corroding agents in solution and vacancies in the material bulk [4]. As before the first stage is driven by A particles which, in this case, chemically attack the bonds in their neighborhood. After a sufficient amount of stress is applied, the crack grows and the A particles (corroding agents) at the tip are exhausted [5]. The transport stage during which B particles must diffuse to the crack (either from solution or the bulk) then begins. The kinetics of propagation are then limited by the rate of diffusion to the crack tip so increases in stress have little effect. Finally as the stress reaches a critical value the diffusion of vacancies into the crack tip from the bulk is sufficiently high for the crack to propagate without any corroding agents.

This analogy between cement setting and SCC has predictive limitations, especially given the level of coarse-graining used in the interpretation which results in a non-rigorous concept of a (virtual/surface) vacancy. Nonetheless, the analogy provides a platform for understanding the kinetics of both of these processes, as well as those in other physical systems, by abstracting the fundamental statistical mechanics and allowing the knowledge from one (when sufficiently coarse grained) to be transferred to the other. More importantly from an atomistic modeling perspective, we can leverage this analogy to transfer elements and refinements from a model of one phenomenon to the other one. As an example, the concept of a nucleating layer that slows down transport during cement setting is a refinement to our binary colloidal model with a direct physical analog in the SCC case, in particular for metals. In a

[4]Rigorously speaking the propagation of the crack at high stresses takes place because the added energy is sufficient to overcome the energy barrier to create a new surface. This surface energy can also be interpreted as the necessary energy to nucleate a "surface" vacancy or to have a vacancy from the bulk migrate to the crack tip. The correspondence between a massive particle (or massless vacancy) and an energy packet can be justified, at a fundamental level, by Einstein's mass/energy duality. While it would be more precise to say that the B particles account for any of these virtual particles we use the concept of a (virtual) vacancy in the bulk as a simple abstraction for simplicity of argument.

[5]It is interesting to note that the reaction between the corroding agents (A particles) and the crack tip surfaces could give rise to a layer that limits diffusion and further crack grow. This is, in principle, analogous to the formation of a metastable C-S-H layer around large C-S-H globules during hydration.

sense establishing these connections is the spirit of this thesis: taking distinct problems and coarse graining their interactions away while focusing on the mechanics of the associated energy landscapes.

5.3.4 ABC Modeling of Colloidal Setting

As discussed in Section 5.1, cement hydration is a process that takes days, months, and sometimes, even years to complete. Therefore any realistic model of cement setting able to capture not only qualitative but quantitative information is not amenable to analysis using MD simulations.

Even though our model represents a significant coarse graining of the true physics of setting we resorted to high temperatures ($T = 1.5$) in order to observe the evolution shown in Figure 5.5 within the simulation time. This increase in temperature has, at least, two obvious effects on the microstructural evolution: (1) all the bonds between particles are effectively weaker, particularly so for the A particles ($\epsilon_{AA}^{LJ} = 1.0$), and (2) the induction time becomes less sensitive to the local microstructure.

Fortunately this is not a major limitation and we can use the ABC method to describe the structure under somewhat more realistic conditions. The approach is straightforward and represents a trivial adaptation of the algorithm of Section 2.3. We allow our reference colloidal model to relax and then evaluate the shear modulus after a new minimum in the energy landscape is found. The time coordinate is chosen according to the approach described in Section 2.3.1, where we assume $\nu = 1$ in LJ units for all processes (effectively rescaling the time axis) rather than rigorously calculating it from the vibrational frequencies around each local minimum. The setting curve resulting from this simple calculation at a temperature of $T = 0.8$ is shown in Figure 5.11. The only significant differences from Figure 5.5 are the lengthening of the induction time as well as the increase of the slope at the end tails. These effects are intuitive and result from the decrease in temperature as discussed previously.

Simulating the system at lower temperatures, and consequently at more realistic time scales, represents the first refinement to our reference colloidal model to approach

more realistic conditions. In particular, we could have lengthened the induction time ($\tau_{induction}$) further by increasing the mass of the B particles at the same temperature. However this example highlights the possibilities of combining the reference model with the methodology of Chapter 2.

The final objective of this approach is to provide a top-down perspective to cement setting to complement the bottom-up cement chemistry approach. Ultimately we must combine elements of the two approaches to develop a predictive model of cement setting. Additional refinements that will be explored in the future, in addition to the application of ABC and ABCD to simulate realistic temperatures and shear rates, include: (1) the incorporation of layers around globules of B particles to simulate the metastable C-S-H coatings observed experimentally, (2) more accurate interaction potentials derived from fundamental studies of cement microtexture - including long range interactions, (3) variable concentrations and nucleation of new species, and (4) expanding from a binary to a trinary system to account for the effects of lime. These improvements, while beyond the scope of this thesis, will hopefully lead to a more complete model of the statistical mechanics of cement setting.

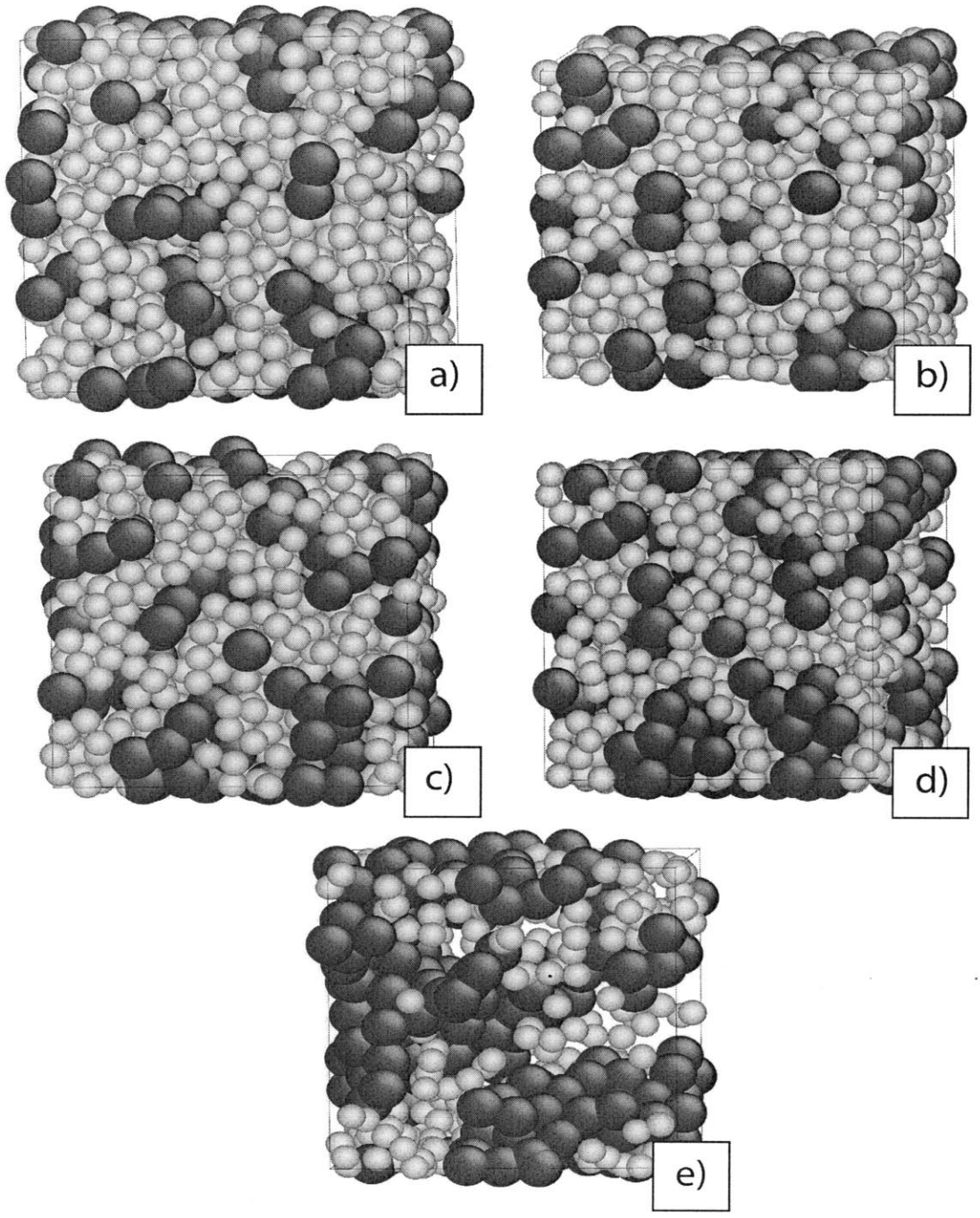

Figure 5-6: Microstructural evolution of the reference colloidal model ($c = 0.2$) during setting: a) The system starts at a low density configuration. b) Rapidly the system densifies and a gel of A particles (white) form. c) B particles (blue) start migrating and clustering together. d)A percolated network of B clusters forms. e) The B network rigidifies the structure. Some of the A particles have been made invisible in (e) to facilitate the visualization of the percolated network.

a)

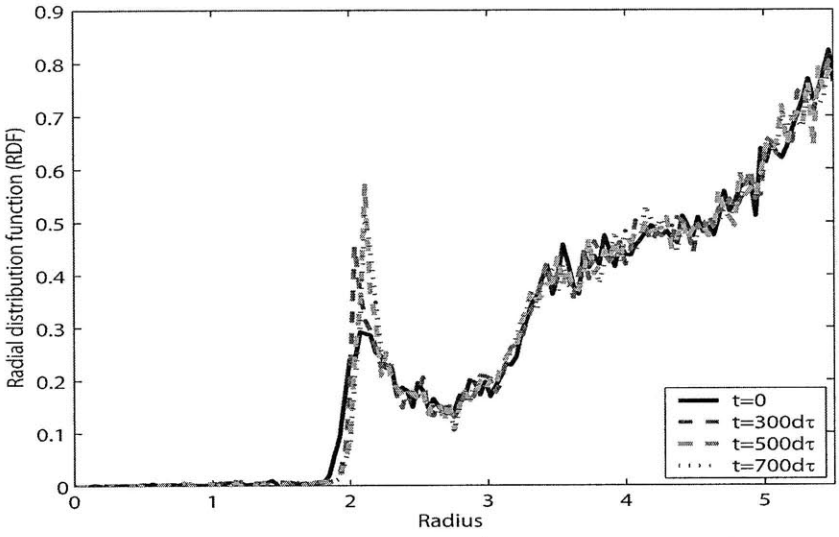

b)

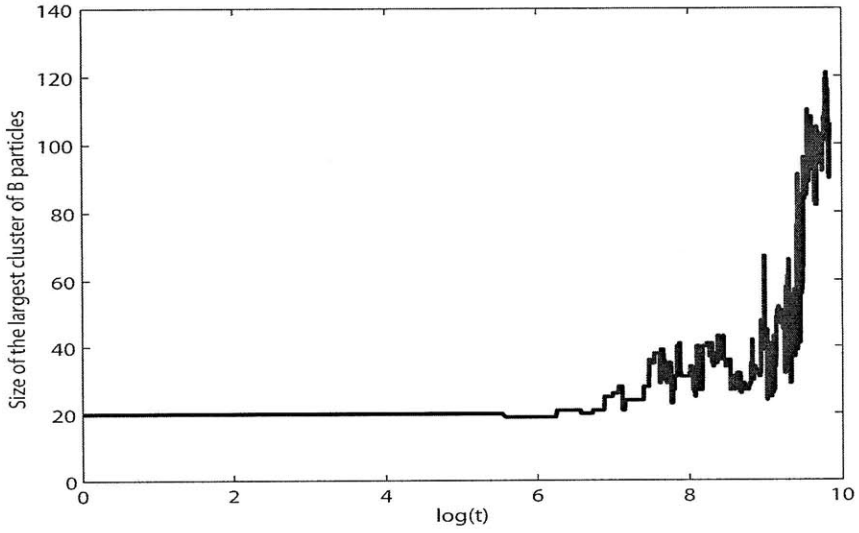

Figure 5-7: Microstructural evolution of the reference colloidal model ($c = 0.2$) during setting: a) Radial distribution function evolution during gelation. b)Size of the B particle connected network. At a critical point the size of the network grows to encompass a majority of the B atoms which, together with Figure 5.6, demonstrate percolation.

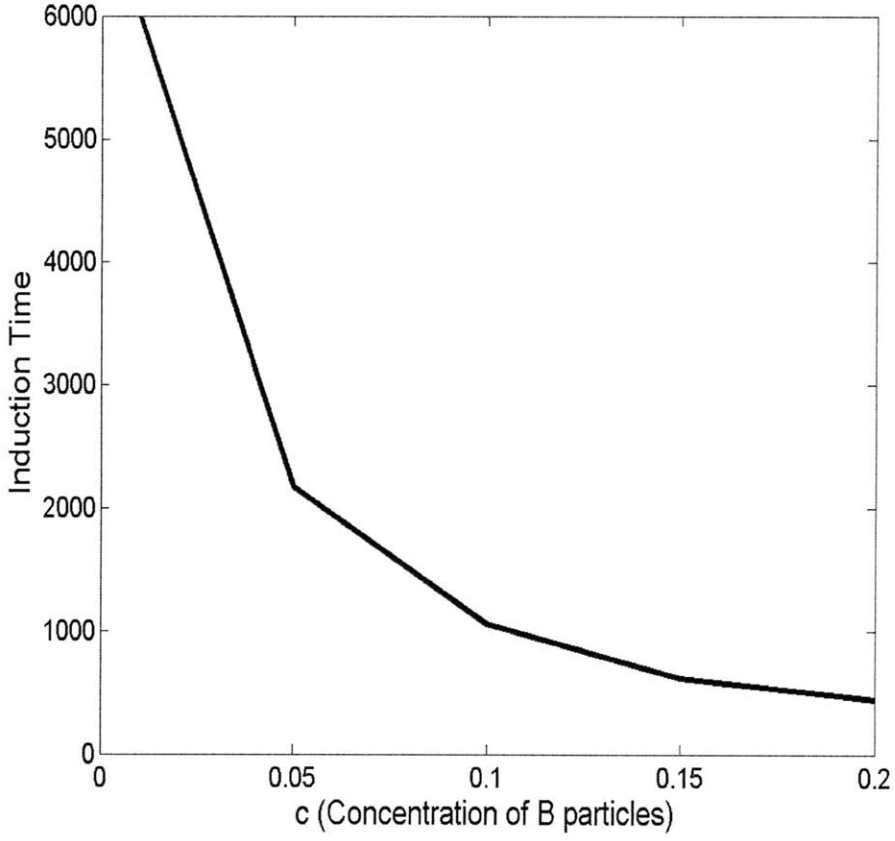

Figure 5-8: Induction time as a function of B particle concentration in the reference colloidal model.

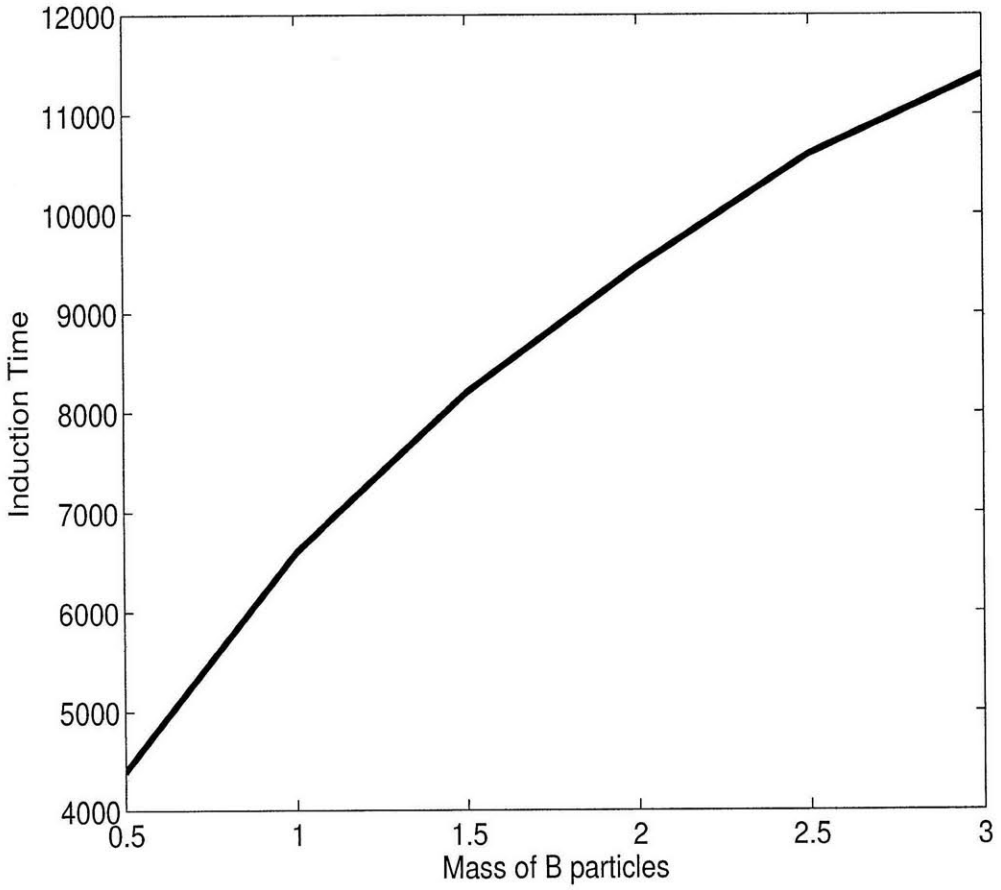

Figure 5-9: Induction time as a function of B particle mass in the reference colloidal model.

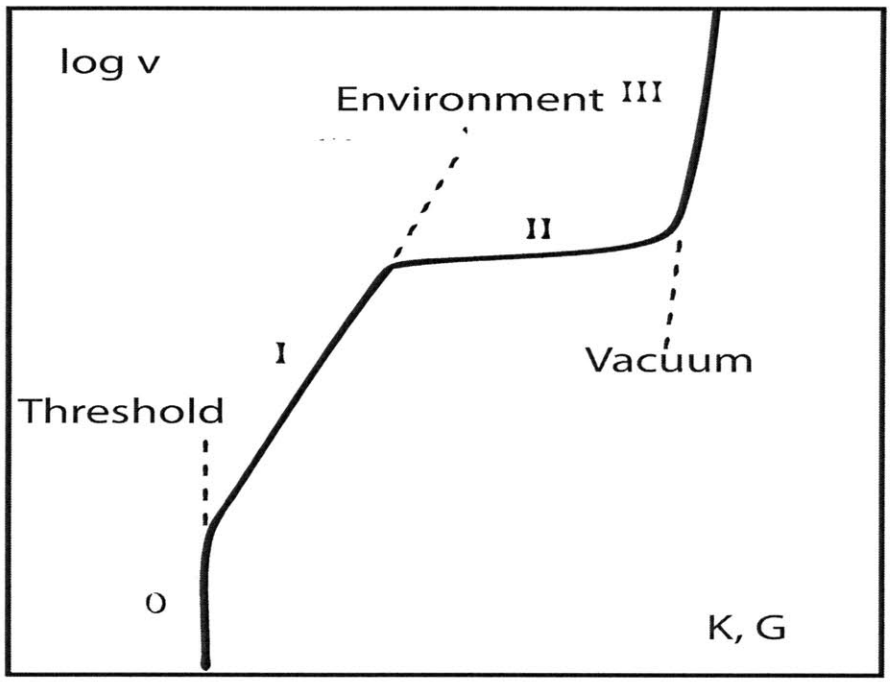

Figure 5-10: Stress corrosion cracking: Crack tip propagation speed as a function of stress concentration [130].

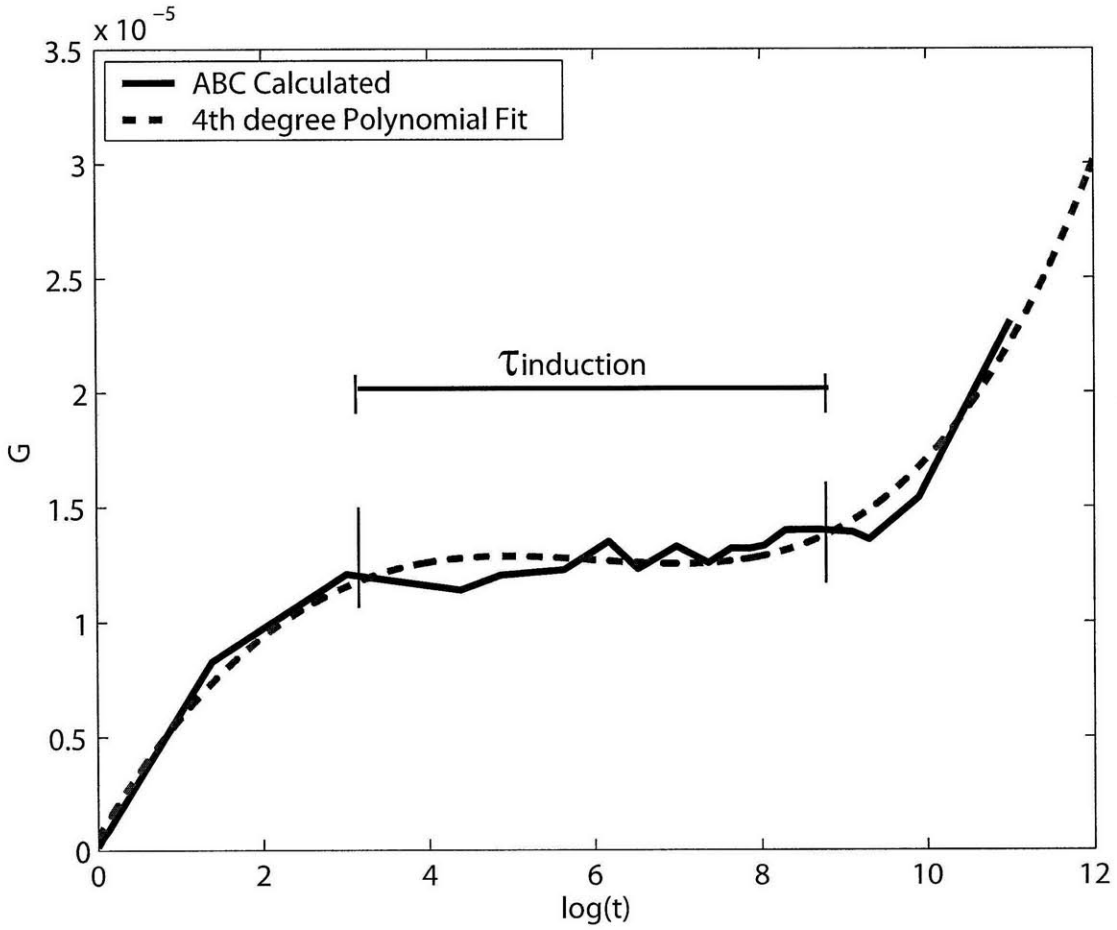

Figure 5-11: Colloidal setting: shear modulus as a function of time in our binary colloidal suspension at $T = 0.6$ as calculated using canonical ABC. $\tau_{induction}$ denotes the length of the induction or incubation stage.

Chapter 6

Summary and Outlook

The three problems tackled in this thesis - hydrogen embrittlement of metals, radiation swelling, and cement setting - are of great technological and scientific importance. This is specially true when focusing on the development of sustainable energy solutions in which concerns related to hydrogen storage, new generation nuclear technologies, and low emissions concrete are pivotal. These problems continue to be very active research areas in materials science and condensed matter physics due to the complex nature of the interactions, microstructures, and kinetic mechanisms that govern the macroscopic behavior, which have not yet been elucidated.

Atomistic modeling can provide insight on the physics of these problems at a fundamental level by showing mechanistic details of particle and defect interaction, migration, and collective motion. In this thesis, we exploit a powerful complementary concept outside of this paradigm: the energy landscape. By analyzing how condensed matter systems traverse through their associated energy landscapes, we can unify seemingly distinct phenomena into fundamental questions of activation barriers, energy basin topology, and microstructural complexity.

There are important challenges associated with the study of complex condensed matter at the atomistic scale. First, materials with high levels of microstructural complexity - in the form of disorder or interplay between chemistry and mechanics - are characterized by behavior which cuts across many length and time scales. Second, these complex materials systems give rise to rough energy landscapes which in turn

are associated with multiple kinetic mechanisms. Both of these issues limit the applicability of standard simulation techniques and require the use of innovative strategies. In dealing with such rough energy landscapes and multiple kinetic mechanisms we have developed a multiscale framework, rooted on transition state theory and the ABC method, which shows promise in simulating general complex condensed matter. Our methodology demonstrated its power in providing specific physical insights into the problems of hydrogen embrittlement, radiation swelling, and cement setting.

Based on both theoretical and experimental evidence of the importance of point defects in the problem of hydrogen embrittlement, we focused on their interactions. Our multiscale approach - combining ab initio calculations, statistical mechanics, and activated state dynamics in the NEB method - demonstrated the crucial role of vacancies in mediating the binding and migration of the PDCs in the alloy. This resulted in a tremendous simplifying assumption for the modeling at larger scales as the trinary alloy Fe-C-H could effectively be decoupled into Fe-C and Fe-H for the purposes of determining the relevant PDCs. Our calculations also suggested the conditions under which continuum models of embrittlement, involving hydrogen atmospheres interacting with line defects, could be valid. In particular our results suggest that for high vacancy concentrations the mechanism of degradation is due to hydrogen accumulation while at low vacancy concentrations diffusion of hydrogen is more important. This understanding of the migration behavior in Fe-C-H at various concentrations can directly inform higher-scale models of creep and delayed degradation. The problem of hydrogen embrittlement also illustrated the tradeoffs involved in modeling complex condensed matter at the atomistic scale when we handle chemistry and mechanics on equal footing. Since the nature of hydrogen chemistry is highly affected by quantum phenomena, the complexity associated with the atomic interactions is essential in explaining macroscopic phenomena. Therefore we required ab initio calculations to obtain the desired accuracy and this, in turn, limited our simulations not only in size, as is standard, but also in the level of microstructural complexity. We therefore only analyzed crystalline systems with a small concentration of PDCs, which exhibit a finite and small number of possible migration pathways and are thus amenable to

analysis with NEB.

For the radiation swelling problem, in which the chemistry of the individual atoms is less important than their collective interactions, we increased the microstructural complexity by including a large amount of highly distorting SIAs in a perfect Fe lattice described by an embedded atom method interatomic potential. As a result of the increase in disorder and complexity the underlying energy landscape for the problem is rougher and gives rise to various modes of long run relaxation. This led to our first application of the ABC method under constant stress, as well as the ABCD generalization to dynamic landscapes. The combination of these methods resulted in a characterization of the morphology of the defects underlying swelling at high dose rates. We showed that under such conditions the metal swells due to the nucleation and growth of disordered phases: dislocation loops and amorphous pockets, paralleling the void nucleation and growth mechanisms responsible for swelling at lower dose rates and high doses. These insights are important for understanding the microstructural evolution before the incubation period in void swelling, as well as the lattice distortions occurring during ion beam implantation of surfaces and nanostructures. Our approach also indicates that the coupling of non-equilibrium MD, ABC, and ABCD represent a powerful toolbox for the study of irradiated materials at long time scales and suggest its application for the study of cascade aging.

Lastly, we developed a reference colloidal model of chemomechanical hardening of cement. Our colloidal model makes use of short-range potential functions describing the effective interactions among the C-H/nucleating C-S-H solvent (species A) and the C-S-H coated clinker particles (species B). The A-A, B-B, and A-B interactions have isotropic (central) repulsive and attractive components characterized by depth and range. In addition the B-B interactions have a directional component to describe preferential bonding which is realized by considering the particles as soft spheres with sticky points on their surfaces. Our results show that the colloidal model is able to capture qualitatively the three-stage kinetic behavior, with stage I corresponding to the gel formation of species A, stage II to the diffusion of species B for the nucleation and growth of B clusters, and stage III to the percolation of B clusters. This coarse

grained approach to cement setting indicates that, at least, a two-phase heterogenous system is required to replicate the three-regime behavior. With the establishment of the reference colloidal model we have determined that the incubation time decreases with the concentration of B species as the mean diffusion time before B particles bind decreases. This is in turn consistent with experimental observations suggesting that the incubation time is negatively correlated with the C-S-H concentration.

Now, at the end of this thesis focused on the atomistic modeling of rough energy landscapes, we can speculate on the potential of the methodology and anticipate some of the future developments in the field. On a broad level, the coupling of phenomena which operate at different scales, such as chemistry and mechanics, represents a new frontier rich with problems exhibiting the behavior discussed in this work. Expanding the materials modeler toolbox to include ABC in all of its flavors, and developing additional adaptations to model the Grand Canonical ensemble and rapidly changing landscapes, are obvious topics for further research. More specifically, our observations of important role of point defects in both the hydrogen embrittlement and radiation swelling problems strongly encourage additional work in understanding interactions among point- and other topological defects over larger length and time scales. With appropriate parallelization, ABC and ABCD could be used to simulate the interaction of PDCs and the type of macroscopic features of relevance for engineering applications. In addition, our PDC dominance diagram representation as well as our characterization of defective structures should be generalized to other alloys and environmental conditions. For the problem of cement setting, our binary colloidal model needs to be refined to introduce the long range ionic interactions emanating from cement microtexture studies. In addition, extensive simulations of the slow evolution should be carried out using ABC to calculate the viscosity of the more realistic structure, and the setting kinetics of the refined model. In all cases, the inclusion of more distorted, dirty microstructures, time-dependent external forces, and strong chemical interactions represent increases in realism. These highly complex condensed matter systems represent the next frontier for our methodology.

Appendix A

Synchronous Parallel Kinetic Monte Carlo

As explained in Section 2.2.2, Kinetic Monte Carlo (KMC) has proven an efficient and powerful tool to study non-equilibrium processes, and it is used in fields as different as population dynamics, irradiation damage, or crystal growth [27, 91, 134]. KMC is generally capable of advancing the time scale significantly faster than direct, time-driven methods, such as MD, but it may suffer from numerical limitations such as stiffness [135]. In addition, and as highlighted earlier, KMC relies on a priori knowledge of a given set of transition rates characterizing the simulated processes, which are assumed to obey Poisson statistics. As a result KMC is, by construction, entirely biased towards those processes which are chosen a priori, and does not necessarily sample the entirety of the energy landscape. This is especially important for the types of rough landscapes discussed in this thesis and is the reason why ABC and its generalizations are favored.

Despite its shortcomings, KMC remains a very useful tool for the study of complex condensed matter systems and their long run evolution, especially when coupled with other methods such as ABC. Due to this versatility in the modeling of Markov processes, a number of parallelization schemes for KMC have been proposed. However, the difficulty of parallelizing KMC lies in the intrinsic time discreticity underlying event-driven simulations, which are sequential in character, and do not lend

themselves to trivial parallel implementations [136]. Various algorithms have been proposed, including rigorous and semi-rigorous approaches based on asynchronous kinetics [137–139]. These methods rely on cumbersome roll-back procedures to avoid causality errors, i.e. event time incompatibilities associated with processor communications. For this reason, most applications of interest are studied using approximate schemes (non-rigorous) for computational convenience. In spite of this, asynchronous parallel KMC has been applied successfully to the field of crystal growth [140].

An alternative algorithm has recently been developed [136, 141] based on a synchronous time decomposition of the master equation. This parallel kinetic Monte Carlo (pKMC) method, eliminates time conflicts by recourse to null events that advance the internal clock of each processor in a synchronized fashion without altering the stochastic trajectory of the system. The basic algorithm works as follows. First, the entire configurational space is partitioned into K subdomains Ω_k. [1]

1. A frequency line is constructed for each Ω_k as the aggregate of the individual rates, r_{ik}, of all the walkers located within each subdomain:

$$R_k = \sum_i^{n_k} r_{ik} \tag{A.1}$$

where n_k and R_k are, respectively, the number of objects and the total rate in each domain k. Here $R_{tot} = \sum_k R_k$ and $N = \sum_k n_k$ is the total number of objects in the system.

2. We define a maximum rate R_{max}, subject to:

$$R_{max} \geq \max_{k=1,\cdots,K} R_k \tag{A.2}$$

this value is then communicated globally to all processors.

3. We assign a null event with rate r_{0k} to each frequency line in each subdomain

[1] Note that, in principle, the decomposition need not be spatial (although this is the most common one). Partitions based on another kind of load balancing can be adopted equally well. However, without loss of generality, we assume that the system is spatially partitioned for our derivations.

k such that:

$$r_{0k} = R_{max} - R_k \tag{A.3}$$

where, in general, the r_{0k} will all be different. The condition of maximum efficiency [136] is that step 2 becomes strictly an equality such that:

$$\exists \Omega_\alpha, \alpha \in 1, ..., K, | R_\alpha \equiv R_{max} \Rightarrow r_{0\alpha} = 0 \tag{A.4}$$

where there is no possibility of null events in Ω_α. However, in principle, each subdomain can have arbitrary r_{0k} as long as all the frequency lines in each Ω_k sum to the same global value. This flexibility furnished by the algorithm may be useful to study the kinetics of certain systems.

4. In each Ω_k an event is chosen with probability $p_{ik} = r_{ik}/R_{max}$, including null events chosen with $p_{0k} = r_{0k}/R_{max}$. For this step we must ensure that independent sequences of random numbers be produced for each Ω_k, using appropriate parallel pseudo random number generators.

5. As in standard BKL KMC, a time increment is sampled from an exponential distribution:

$$\delta t_p = -\frac{\ln(\zeta)}{R_{max}} \tag{A.5}$$

where ζ is a suitable random number between 0 and 1. As described in Section 2.2. this guarantees that by virtue of Poisson statistics δt_p becomes the global time step for all the parallel processes.

6. Communicate boundary events. This may require global or local calls, depending on the problem at hand.

This algorithm solves the master equation exactly for non-interacting particles such as in continuous diffusion [136]. When particles are allowed to interact across domain boundaries, suitable corrections must be implemented to avoid boundary conflicts [141]. For lattice based kinetics with short range interaction this can be achieved by methods based on a chessboard sublattice technique. The minimum number of sublattices to ensure non-interacting adjacent domains depends on a number of fac-

tors, most notable dimensionality. [2] In 3D, the chessboard requires a subdivision into a minimum of eight sublattices. The implementation of the sublattice algorithm to solve boundary errors replaces Step 4 in the algorithm above by:

4a. A given sublattice is chosen for all subdomains. This choice may be performed in several ways such as fully random or using some type of permutation that ensures every sublattice is visited in each KMC cycle. Restricting each processor's sampling to only one lattice, however, while avoiding boundary conficts, results in a systematically correlated error [141].

4b. An event is chosen in the selected sublattice with the appropriate probability, including null events. The global communication of R_{max} in step 2 may become a considerable bottleneck in terms of parallel efficiency. When the rate changes in each Ω_k after a KMC cycle are unpredictable, a global communication call is unavoidable. However this limitation can be circumvented in certain cases (such as Ising systems for example) by considering the maximum theoretical aggregate rates, e.g. R'_{max} for an ensemble of Ising spins with:

$$R'_{max} = \lambda n_k [\frac{\exp(-\Delta E_{max})}{1 + \exp(-\Delta E_{max})}] \tag{A.6}$$

where E_{max} is the theoretical maximum energy increment due to a single spin change:

$$\Delta E_{max} = -2(n_b|J| - |H|) \tag{A.7}$$

where the Ising Hamiltonian is given by:

$$\mathcal{H}(\sigma) = -J \sum_{(i,j)} \sigma_i \sigma_j - H \sum_i \sigma_i \tag{A.8}$$

Alternatively a self-learning process can be performed to optimize R'_{max}. In this case the upper estimate of R_{max} is refined by recording the history of rate changes over the course of the PKMC simulation. Details on the performance and limitations of

[2] In 2D, four sublattices are sufficient for any arbitrary partition, as established by the solution to the 'four color problem'.

the algorithm can be found in references [136] and [141].

Appendix B

Linear Response Theory

The first part of these derivations, regarding thermal transport coefficients, follow from Appendix B of Ju Li's thesis [142] which in turn summarizes previous results on the linear response theory of transport. The second part, regarding externally driven transport coefficients represents a consistent adaption of separate perturbative results [120].

From statistical mechanics we know that the entropy of a system is defined by the amount of phase space volume gained from an energy change. That is:

$$d\Gamma = e^{S/k} dE \tag{B.1}$$

The second law of thermodynamics then implies that an isolated system looks to increase its entropy by exploring phase space, i.e. traversing the energy landscape, until it eventually relaxes to the largest patch of phase volume, the *global equilibrium*, and fluctuates. In the case of non-isolated systems the direction of the relaxation can be equally explained by relying on the Helmholtz or Gibbs free energies rather than the system's entropy, and the macrostate follows a similar direction in the corresponding (not necessarily potential) energy landscapes toward the global equilibrium. The motion of this macrostate can be impeded by roughness in the landscape and activation energy barriers that must be surmounted, which give rise to local equilibria in which the system can settle and fluctuate temporarily. These local equilibria can be

characterized by a subset of macroscopic variables which remain effectively constant for a (potentially) long time.

Consider a microcanonical macrostate traversing a rough energy landscape toward the global equilibrium and characterized by the variables $X, Y, Z, ...$ Without loss of generality we can label the global equilibrium by $X = Y = Z = ... = 0$. When the macrostate is at this point entropy is maximized, therefore the total phase volume of the system can be approximated by that of the neighborhood of the global equilibrium and the equilibrium entropy S_E. Alternatively, the system can fluctuate at a local equilibrium, and then the entropy has additional dependencies on the variables $X, Y, Z, ...$ as follows:

$$d\Gamma \equiv \frac{d\mathbf{p}^N d\mathbf{q}^N}{h^{3N}} = \exp(\frac{S}{k})\frac{dE}{g_E} \cdot \frac{dX}{g_X}\frac{dY}{g_Y} \cdots \tag{B.2}$$

where $g_E, g_X, g_Y, ...$ are the appropriate coarse-graining scales on the order of the spontaneous fluctuations at the global equilibrium. With this description it can be shown that:

$$S_E(E, N, V) = S(X = 0, Y = 0, Z = 0, ...|E, N, V) \tag{B.3}$$

Since increasing the entropy in this microcanonical system is the driving force for traversing the energy landscape, we can calculate the effect on entropy of a perturbation to the state variables as:

$$\delta S \equiv \frac{\partial S}{\partial X}\delta X + \frac{\partial S}{\partial Y}\delta Y + \frac{\partial S}{\partial Z}\delta Z + \cdots \tag{B.4}$$

and we can define the forces driving the evolution of the macrostate as:

$$F_X \equiv \frac{\partial S}{\partial X}, F_Y = \frac{\partial S}{\partial Y}, \cdots \tag{B.5}$$

so at the global equilibrium we have:

$$F_X = F_Y = F_Z = \cdots = 0 \tag{B.6}$$

Now near a local equilibrium the changes in the state properties are small, that is $\dot{X}, \dot{Y}, \dot{Z}, ... << 1$ and we can use a linear approximation giving:

$$\dot{X} \equiv L_{XX}F_X + L_{XY}F_Y + L_{XZ}F_Z + \cdots \tag{B.7}$$

$$\dot{Y} \equiv L_{YX}F_X + L_{YY}F_Y + L_{YZ}F_Z + \cdots \tag{B.8}$$

$$\dot{Z} \equiv L_{ZX}F_X + L_{ZY}F_Y + L_{ZZ}F_Z + \cdots \tag{B.9}$$

$$\vdots$$

Or letting $X_1 = X$, $X_2 = Y$, ..., be the n non-zero gross state variables we can summarize as:

$$F_i \equiv \frac{\partial S}{\partial X_i} \equiv -\sum_{j=1}^{n} S_{ij}X_j \tag{B.10}$$

$$\dot{X}_i = \sum_{j=1}^{n} L_{ij}F_j \tag{B.11}$$

Now we can calculate the statistical averages of the rates of evolution in response to a driving force as follows:

$$\langle \dot{X}_i(t) \rangle = \sum_{j=1}^{n} L_{ij}\langle F_j(t) \rangle = -\sum_{j=1}^{n} L_{ij} \sum_{k=1}^{n} S_{jk}\langle X_k(t) \rangle \tag{B.12}$$

Now if this is true for $t >> \tau_M$ where τ_M is the molecular correlation time (e.g. integration time step for MD simulations, on the order of ps). and we choose t such that $\tau_M << t << |(\mathbf{LS})^{-1}|$ (which can be done since by Onsager's hypothesis $|(\mathbf{LS})^{-1}|$ is macroscopic) then:

$$\langle \dot{X}_i(t) \rangle X_l(0) = -\sum_{j=1}^{n} L_{ij} \sum_{k=1}^{n} S_{jk}\langle X_k(t) \rangle X_l(0) \tag{B.13}$$

now averaging over the distribution of initial $\mathbf{X}(0)$ from the equilibrium ensemble we find:

$$\langle \langle \dot{X}_i(t) \rangle X_l(0) \rangle_{\mathbf{X}(0)} = -\sum_{j=1}^{n} L_{ij} \sum_{k=1}^{n} S_{jk}\langle \langle X_k(t) \rangle X_l(0) \rangle_{\mathbf{X}(0)} \tag{B.14}$$

However, since $t << |(\mathbf{LS})^{-1}|$, then on a macroscopic scale $\langle X_k(t)\rangle$ is very close to $\langle X_k(0)\rangle \equiv X_k(0)$ since we assume that the correlation time of a slow variable is much longer than that of its fluctuations. Then:

$$\langle\langle X_k(t)\rangle X_l(0)\rangle_{\mathbf{X}(0)} \approx \langle X_k(0)X_l(0)\rangle_{\mathbf{X}(0)} \tag{B.15}$$

In addition, for any properly defined sub-ensemble we have:

$$\langle\langle A(t)B(0)\rangle_{B(0)} = \langle A(t)B(0)\rangle \tag{B.16}$$

where

$$\langle A(t)B(0)\rangle = \langle A(\mathbf{p}^N(t),\mathbf{q}^N(t)|\mathbf{p}^N(0),\mathbf{q}^N(0))B(\mathbf{p}^N(0),\mathbf{q}^N(0))\rangle \tag{B.17}$$

Thus Equation (B.14) becomes:

$$\langle \dot{X}_i(t)X_l(0)\rangle = -\sum_{j=1}^{n} L_{ij}\sum_{k=1}^{n} S_{jk}\langle X_k(t)X_l(0)\rangle \tag{B.18}$$

But from Equation (B.2) we can expand:

$$S \approx S_E - \sum_{i=1}^{n}\sum_{j=1}^{n} S_{ij}X_iX_j/2 \tag{B.19}$$

so we have:

$$\langle X_k(0)X_l(0)\rangle = S_{kl}^{-1}k \tag{B.20}$$

so:

$$-\sum_{j=1}^{n} L_{ij}\sum_{k=1}^{n} S_{jk}\langle X_k(t)X_l(0)\rangle = -\sum_{j=1}^{n} L_{ij}\sum_{k=1}^{n} S_{jk}S_{kl}^{-1}k = -\sum_{j=1}^{n} L_{ij}\delta_{jl}k = -kL_{il} \tag{B.21}$$

so from Equation (B.18) we have:

$$\langle \dot{X}_i(t)X_l(0)\rangle = -kL_{il} \tag{B.22}$$

on the other hand we can write:

$$\begin{aligned}\langle \dot{X}_i(t) X_l(0)\rangle &= \langle (\dot{X}_i(0) + \int_0^t d\tau \ddot{X}_i(\tau)) X_l(0)\rangle \\ &= \int_0^t d\tau \langle \ddot{X}_i(\tau) X_l(0)\rangle + \langle \dot{X}_i(0) X_l(0)\rangle \end{aligned} \tag{B.23}$$

but in the presence of $\mathbf{p} \rightleftharpoons -\mathbf{p}$ symmetry we have:

$$\langle A(t)B(0)\rangle = \langle A(0)B(-t)\rangle = \langle A(0)B(t)\rangle \tag{B.24}$$

furthermore:

$$0 = \frac{d}{dt}\langle A(t)B(t)\rangle|_{t=0} = \langle \dot{A}(0)B(0)\rangle + \langle A(0)\dot{B}(0)\rangle \Rightarrow \langle \dot{A}(0)B(0)\rangle = 0 \tag{B.25}$$

hence from Equation (B.23) we have:

$$\langle \dot{X}_i(t) X_l(0)\rangle = \int_0^\infty d\tau \langle \ddot{X}_i(\tau) X_l(0)\rangle \tag{B.26}$$

plugging in Equation (B.24) and integrating by parts we arrive at the Green-Kubo fluctuation dissipation theorem for $t/\tau_M \rightarrow \infty$:

$$L_{ij} = \frac{1}{k}\int_0^\infty d\tau \langle \dot{X}_i(\tau)\dot{X}_j(0)\rangle \tag{B.27}$$

This result can therefore be used to compute thermal transport coefficients from equilibrium ensemble properties. As will be demonstrated in the applications, this approach can be coupled with energy landscape sampling to provide a rigorous estimate for these type of transport coefficients.

Externally driven transport coefficients can be calculated in a similar fashion. In this case the forces driving the evolution the macrostate are not the thermal forces of Equation (2.26) but external forces, such as those from an electric field:

$$F_X = F_X^e, F_Y = F_Y^e, \cdots \tag{B.28}$$

If the external force is small we can proceed with a linear perturbative approach resulting in an expression identical to Equation (B.11).

$$\dot{X}_i = \sum_{j=1}^{n} L_{ij} F_j \tag{B.29}$$

Now the perturbation also modifies the underlying Hamiltonian which describes the system dynamics from $\mathcal{H}_0$ to $\mathcal{H}$. Now the canonical distribution for this new Hamiltonian is given by:

$$W(\mathbf{X}, 0) = \frac{\exp(-\frac{1}{kT}\mathcal{H}(\mathbf{X}))}{\mathcal{Z}} \tag{B.30}$$

where $\mathcal{Z}$ is the partition function $\int \exp(-\frac{1}{kT}\mathcal{H})(\mathbf{X}))d\mathbf{X}$. That is $d\Gamma = W(\mathbf{X}, 0)d\mathbf{X}$. Now, in general, the field couples with each of the gross macroscopic variables and the perturbation in the Hamiltonian is small, so we can expand linearly to find:

$$\mathcal{H} = \mathcal{H}_0 + \sum_{i=1}^{N}\sum_{j=1}^{N} H_{ij} X_i F_j \tag{B.31}$$

so perturbatively we can write Equation (B.30) as:

$$W(\mathbf{X}, 0) = W_0(\mathbf{X})(1 - \frac{1}{kT}\sum_{i=1}^{N}\sum_{j=1}^{N} H_{ij} X_i F_j) \tag{B.32}$$

where W_0 is the non-perturbed canonical distribution. Then, just as in Equation (B.20) we find that the average is given by:

$$\langle X_k(0) X_l(0) \rangle = H_{kl}^{-1} kT \tag{B.33}$$

and in addition, averaging over the ensemble given by $W(\mathbf{X}, 0)$ we find:

$$\langle \dot{X}_k(t) \rangle = \langle \dot{X}_k(0) \rangle - \frac{1}{kT}\sum_{i=1}^{N}\sum_{j=1}^{N} H_{ij} \langle \dot{X}_k(t) X_i(0) \rangle \langle F_j(t) \rangle \tag{B.34}$$

Now the first term in the right hand side obviously vanishes since fluctuations around

equilibrium at time $t = 0$ cancel each other. So from Equation (B.29) we have:

$$\sum_{j=1}^{n} L_{kj}\langle F_j(t)\rangle = -\frac{1}{kT}\sum_{i=1}^{N}\sum_{j=1}^{N} H_{ij}\langle \dot{X}_k(t)X_i(0)\rangle\langle F_j(t)\rangle \tag{B.35}$$

and since this must hold for any external field $\mathbf{F}$ this implies:

$$L_{kj} = -\frac{1}{kT}\sum_{i=1}^{N} H_{ij}\langle \dot{X}_k(t)X_i(0)\rangle \tag{B.36}$$

Which from Equation (B.33) implies that:

$$L_{kj} = -\frac{1}{kT}\int_0^t d\tau \sum_{i=1}^{N} H_{ij}\langle \dot{X}_k(\tau)\dot{X}_i(0)\rangle \tag{B.37}$$

Now letting $J_j(t) = \frac{1}{T}\sum_{i=1}^{N} H_{ij}\dot{X}_i$, be the dissipative flux (scaled by temperature in this case), i.e. the rate of change of internal energy (in units of temperature) as a result of the external field, we can rewrite Equation (B.37) as:

$$L_{kj} = -\frac{1}{k}\int_0^t d\tau\langle \dot{X}_k(\tau)J_j(0)\rangle \tag{B.38}$$

which is the fluctuation dissipation theorem for externally driven transport coefficients.

The close similarity between the fluctuation expressions for both types of transport coefficients is not coincidental. In fact, the non-equilibrium boundary conditions for a thermal transport can be mathematically transformed into a mechanical field which performs work on the system, and this work is converted into heat. Therefore the two representations of the system are congruent [120].

Appendix C

Atomistic Description of C-S-H

The model for the atomistic description of C-S-H described in this appendix is the result of work by Pellenq and his collaborators and is described in detail in reference [131]. It is summarized here for the benefit of our readers in relation to the binary colloidal model for cement setting discussed in Section 5.3. It represents the basis for the development of more realistic microtexture interatomic potentials to refine our colloidal model.

The most basic models of C-S-H arise from structural comparisons with crystalline calcium silicate hydrates, based on H. F. W Taylor's postulate that real C-S-H was a structurally imperfect layered hybrid of two natural mineral analogs [143]: tobermorite of 14$\mathring{A}$ interlayer spacing [$Ca_5Si_6O_{16}(OH)_2.7H_20$] [144], and jennite [$Ca_9(Si_6O_{18})(OH)_6 \cdot 8H_2O$] [145]. While this suggestion is plausible in morphological terms, this model is incompatible with two basic characteristics of real C-S-H; specifically the calcium-to-silicon ratio (C/S) and the density. Recently, small-angle neutron scattering measurements have fixed the C/S ratio at 1.7 and the density at 2.6 g/cm^3 [146], values that clearly cannot be obtained from either tobermorite ($C/S = 0.83$, 2.18 g/cm^3) or jennite ($C/S = 1.5$ and 2.27 g/cm^3). From the standpoint of constructing a molecular model of C-S-H, this means that these crystalline minerals are not strict structural analogs.

With this insight in mind, Pellenq et al. developed an atomistic-level structural model for C-S-H, developed from a bottom-up perspective and validated against sev-

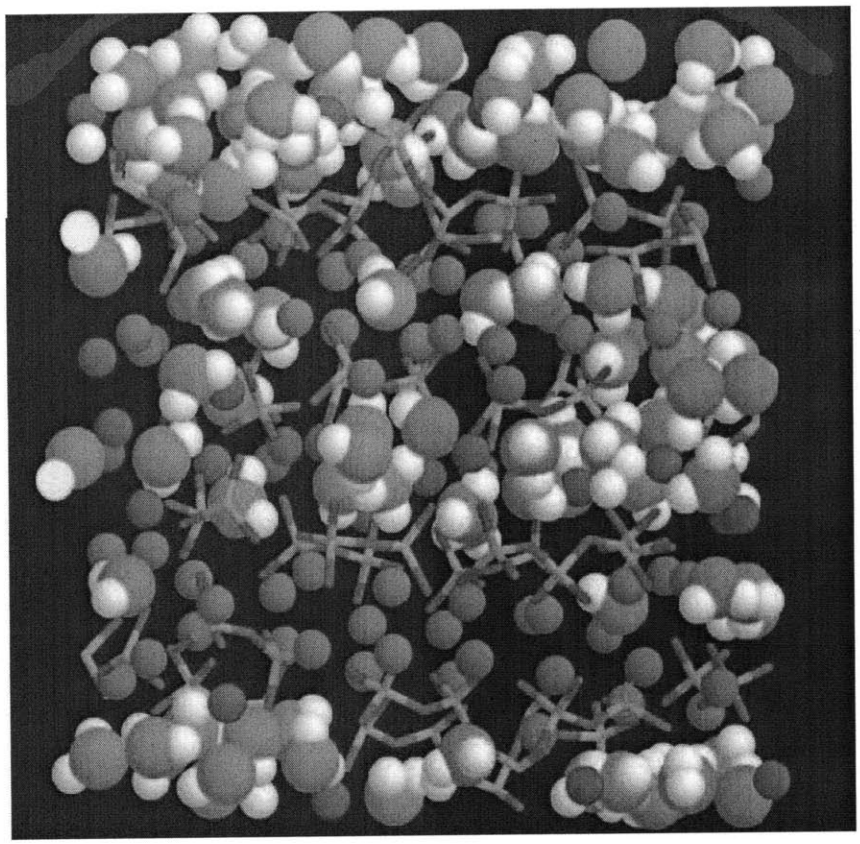

Figure C-1: Molecular model of C-S-H. Blue and white spheres are oxygen and hydrogen atoms of water molecules, respectively. Green and gray spheres are inter and intra-layer calcium ions, respectively. Yellow and red sticks are silicon and oxygen atoms in silica tetrahedra [131].

eral experimental analyses of structure and properties which captures the correct C/S ratio and density. The model is constructed from a monoclinic periodic computational cell of dry tobermorite of interlayer spacing of approximately $11\mathring{A}$, with 4, 2, and 1 units along axes a, b, and c with a unit cell chemical formula of $Ca_6Si_6O_{16}$. SiO_2 (neutral) groups are removed from silica tetrahedra guided by NMR results that show Q_0 10%, Q_1 67%, and Q_2 23%. The final configuration has Q_0 13%, Q_1 67%, and Q_2 20% and a C/S ratio of 1.65. The dry cell is then relaxed to a density of 2.12 g/cm^3, and water is added via Grand Canonical Monte Carlo simulations. At equilibrium the adsorbed water increases the density to 2.56 g/cm^3, though it decreases by 4% after additional relaxation. The molecular configuration of the C-S-H structure,

with chemical composition $(CaO)_{1.65}(SiO_2)(H_2O)_{1.75}$, is shown in Figure C.1. and details on the parameters are listed in the supplemental information of reference [131].

Appendix D

Benchmarking of Constant Stress ABC

In this appendix we benchmark the constant stress ABC generalization to a few simple problems. For simplicity we consider problems with a constant hydrostatic pressure rather than a full non-diagonal external stress tensor.

As a first example we consider the calculation of the migration energy barrier for SIA migration in Fe as a function of external pressure. A Fe atom is inserted in a tetrahedral site of a 10x10x10 bcc Fe lattice and allowed to relax to a $\langle 110 \rangle$ dumbbell configuration and migrate, all of this at constant pressure. The relaxation and subsequent migration are investigated in two ways: by MD simulations with increasing temperature and by the constant stress (pressure) ABC method.

From the MD calculations we calculate diffusion coefficients at a various temperatures and fit to an Arrhenius curve to obtain the effective activation barrier. We repeat this process at different pressure to estimate the pressure dependence of the SIA migration barrier. These results are then compared with the barriers calculated using the first version of ABC at constant stress (Figure 2.6.a). The results are reported in Figure D.1.

We notice excellent agreement between our ABC constant pressure calculations and the MD estimates within the errors associated with the fit of the diffusion coefficients as well as the resolution (σ) used for the ABC simulations.

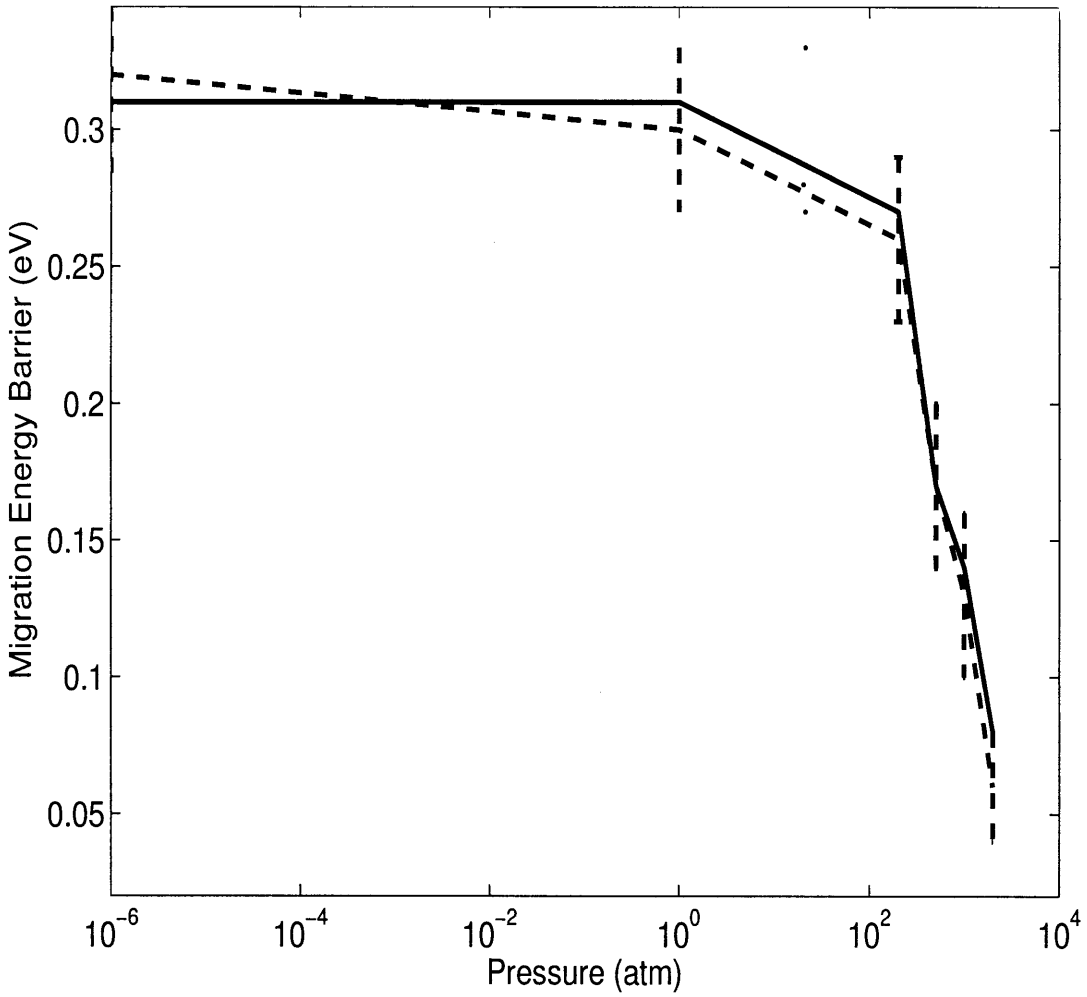

Figure D-1: SIA ($\langle 110 \rangle$ dumbbell) migration energy barrier as a function of pressure in bcc Fe as calculated from MD simulations (dashed line) and constant pressure ABC (solid line).

The second example looks at the relaxation of a 5x5x5 Fe bcc lattice with 15 SIAs at constant zero pressure as simulated by isobaric MD and ABC. The results of this benchmarking are illustrated in Figures D.2 and D.3. The first figure shows that the agreement in the volumetric expansion is excellent for the ABC at constant pressure and MD methods. However, the ABC method recovers additional relaxations at longer time scales no captured by the MD simulation. The second figure shows qualitative agreement in the strain fields of the microstructure, with the simulated structure after 3 million MD steps matching that from the constant pressure ABC

results after 83 Gaussian penalties with $W = 0.05$ eV and $\sigma = 0.05\mathring{A}$. Figure D.3. also shows a more relaxed configuration found by ABC after an additional 15 ABC metasteps.

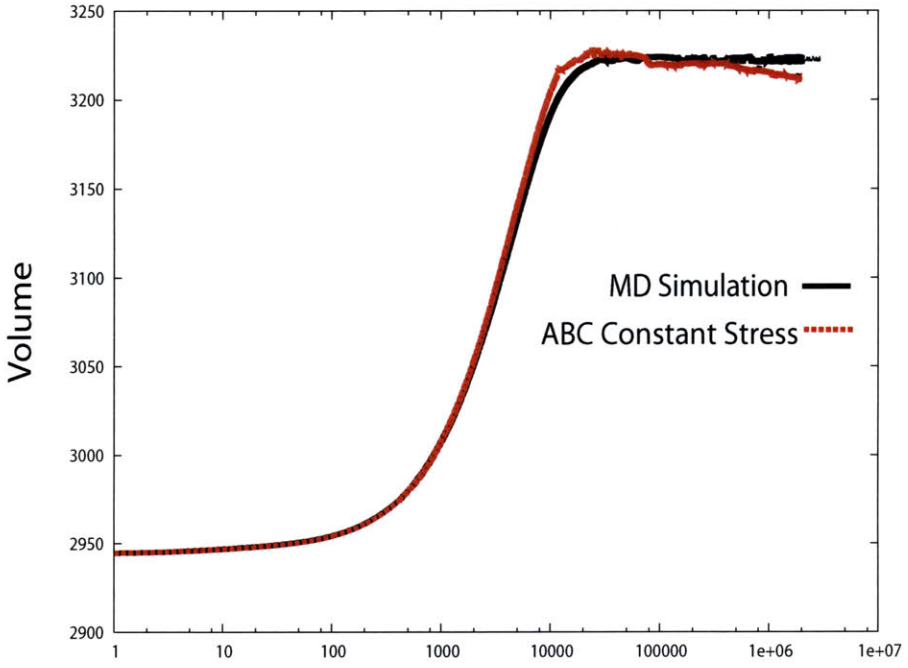

Figure D-2: Volumetric expansion of a damaged 5x5x5 bcc Fe lattice with 15 SIAs at zero pressure. The x-axis denotes the time steps for the MD simulation as well as the cell relaxation portion of the ABC simulation (the ABC metasteps are not included).

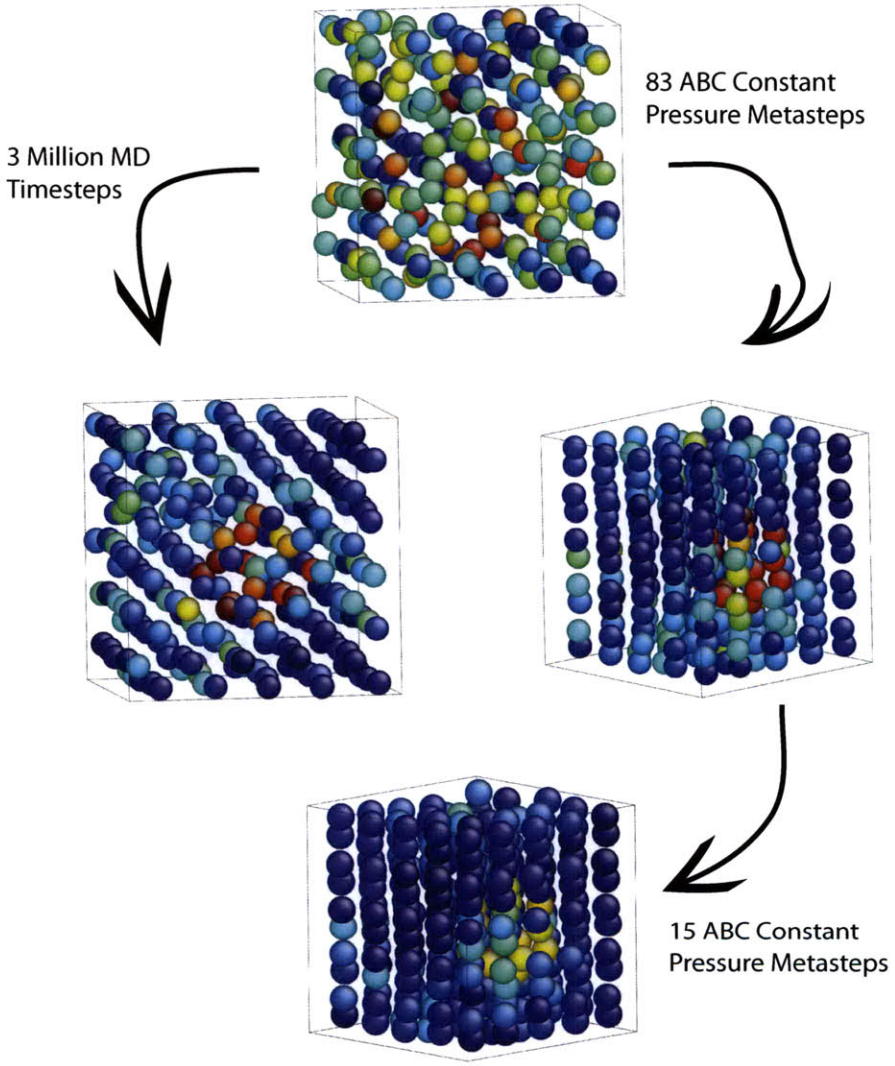

Figure D-3: Illustration of the evolution of the microstructure of a damaged 5x5x5 bcc Fe lattice with 15 SIAs at zero pressure. The colors indicate the local Von Mises shear strain invariant. Starting from the same initial configuration the MD simulations (left) lead to a partially relaxed structure. The constant pressure ABC simulation qualitatively reproduces the behavior and generates a more relaxed configuration.

Appendix E

Benchmarking of ABCD

In this appendix we benchmark the ABCD method in a problem of a slowly changing number of particles.

For this problem, analogous in spirit to the one which we discuss in Chapter 4, we consider a 5x5x5 bcc unit cell of Fe that is irradiated (as described in Section 4.2) at a rate of 1.33×10^{11} SIA insertions/s for 50 ps. The cell starts with one Frenkel pair (vacancy and SIA) separated far enough that recombination is not immediate. The initial migration energy barrier for the SIA is on the order of 0.3 eV, so at high enough temperatures the relaxation of the system is sufficiently fast to ensure that the assumptions required by ABCD hold, even at such a high dose rate. We analyze the evolution of the system with both ABCD and MD at 1000 K. The choice of high temperature is to "slow down" ABCD as well as speed up the MD simulation. Since ABCD is designed for very slowly varying landscapes the time coordinate moves forward quite rapidly if the temperature under consideration is low (see Section 2.4). This is precisely the advantage of the method over MD since it moves the time horizon forward rapidly, however it makes direct comparisons difficult due to the large gap in timescales. A choice of high temperature thus reduces the average ABCD time steps and makes comparison with MD simulations possible.

Snapshots of the microstructural evolution of the clusters are given below in Figures E.1 (for ABCD) and E.2 (for MD) showing excellent qualitative agreement. The kinetics, as described by both methods, show that the initial SIA does not migrate

rapidly enough and therefore the vacancy does not recombine until the first SIA is inserted, after which the SIAs proceed to cluster, relax into a dislocation loop, and diffuse. Due to the stochastic nature of the time variable in ABCD as well as the temperature randomness in MD only partial quantitative agreement can be expected. For a larger unit cell and slower changes in the landscape (i.e., dose rate in this case) we expect the statistical averaging to be sufficient to ensure that rigorous quantitative comparisons are possible. However, even in this case, the qualitative agreement for this example is on the level of accuracy expected of methods such as KMC.

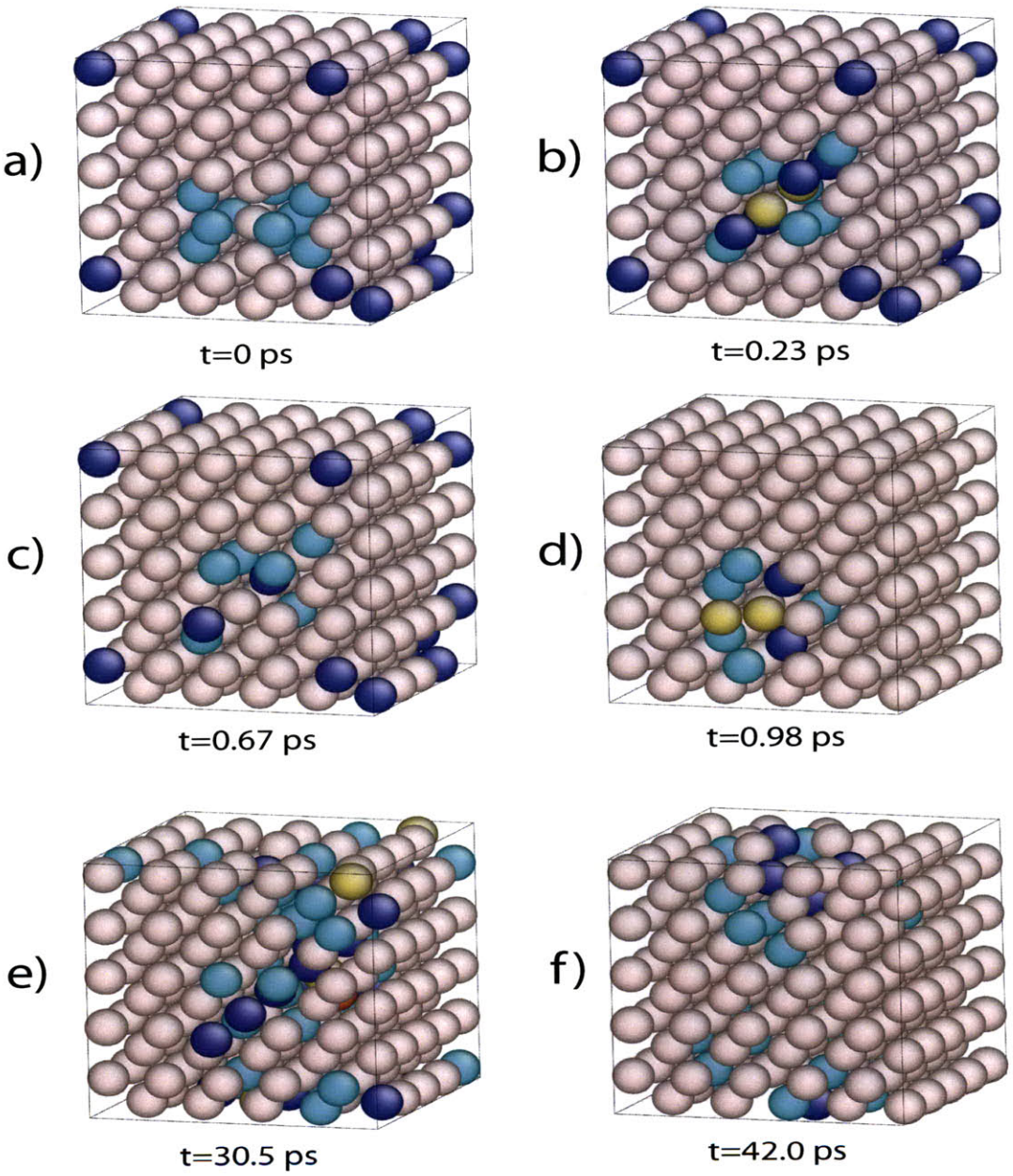

Figure E-1: Evolution of an irradiated Fe cell at $T = 1000$ K followed using ABCD. The atoms are colored according to their coordination number. a) The initial configuration is a separated Frenkel pair, b)the SIA relaxes to a $\langle 111 \rangle$ dumbbell, c) the initial SIA starts migrating, d) another SIA is introduced annihilating the vacancy, e)the SIA diffuses several times and three more SIAs are introduced, f)the SIAs cluster and diffuse. The time scale is generated stochastically as described in Section 2.4.

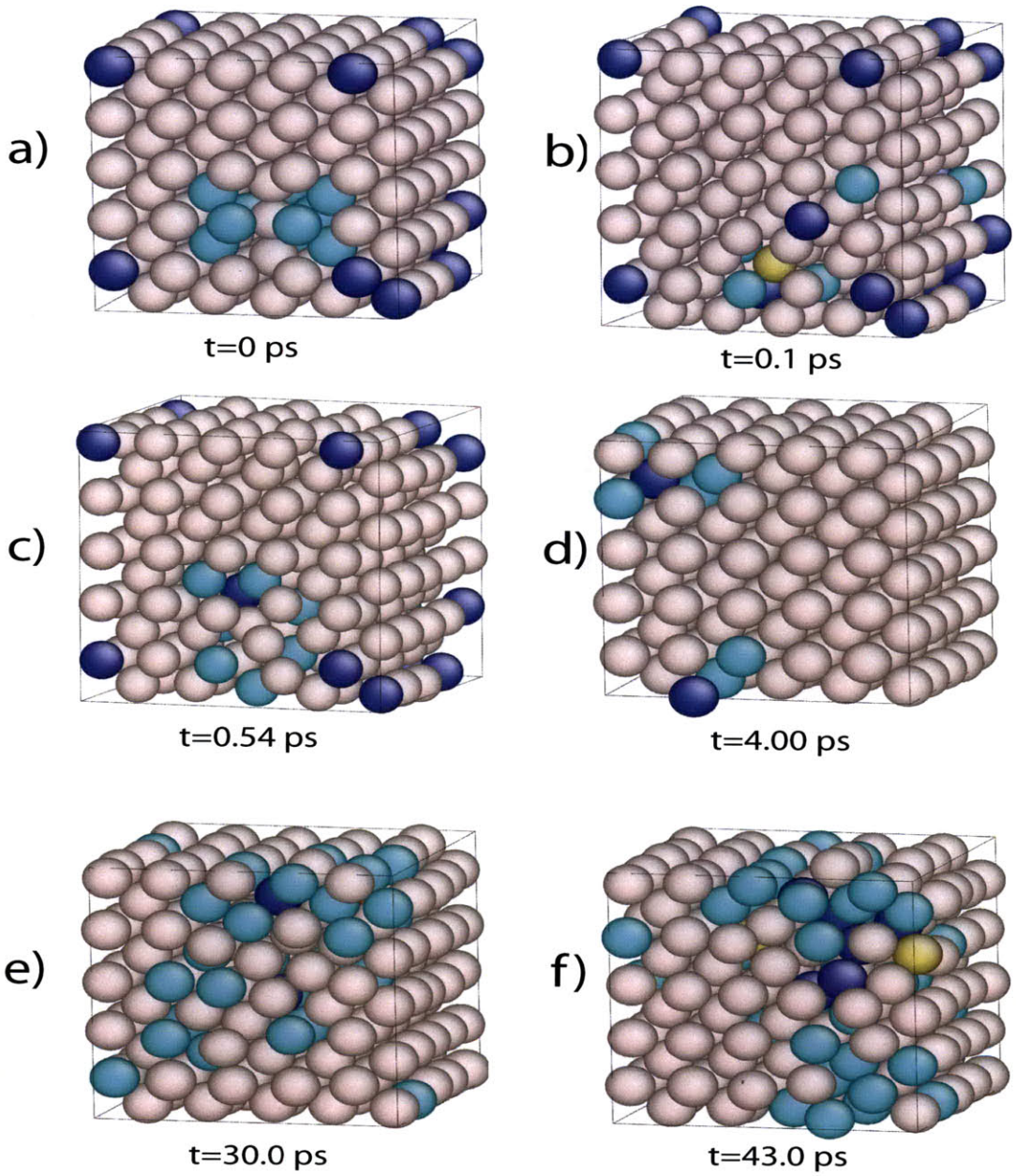

Figure E-2: Evolution of an irradiated Fe cell at $T = 1000$ K followed using MD.The atoms are colored according to their coordination number. a) The initial configuration is a separated Frenkel pair, b)the SIA relaxes to a $\langle 111 \rangle$ dumbbell, c) the initial SIA starts migrating, d) another SIA is introduced annihilating the vacancy, e)the SIA diffuses several times and three more SIAs are introduced sequentially, f)the SIAs cluster and diffuse.

Appendix F

Isothermal Linear Viscoelasticity

The three dimensional theory of linear viscoelasticity is important in understanding the nature of the type of experimental measurements and theoretical calculations that one can perform to determine the stress relaxation of an aging viscoelastic material such as a cement slurry. Following a review by Golden and Graham [147] here we present the essential results.

First, for non-aging, deforming materials at constant temperature we can write the stored potential energy density at a given point as in terms on the local strain history as:

$$V(t) = \frac{1}{2}\int_{-\infty}^{t} dt_1 \int_{-\infty}^{t} dt_2 K_{ijkl}(t-t_1, t-t_2)\dot{\epsilon}_{ij}(t_1)\dot{\epsilon}_{kl}(t_2) \tag{F.1}$$

where we omit the spatial index for convenience, and assume that the strain vanishes in the distant past. By symmetry we have that $K_{ijkl}(t,t') = K_{klij}(t,t')$ and it is also symmetric under exchanges of i and j, or k and l. Differentiating Equation (F.1) we find:

$$\dot{V}(t) = \dot{\epsilon}_{ij}(t)\int_{\infty}^{t} dt_2 K_{ijkl}(0, t-t_2)\dot{\epsilon}_{kl}(t_2) + \frac{1}{2}\int_{-\infty}^{t} dt_1 \int_{-\infty}^{t} dt_2 \frac{\partial}{\partial t} K_{ijkl}(t-t_1, t-t_2)\dot{\epsilon}_{ij}(t_1)\dot{\epsilon}_{kl}(t_2) \tag{F.2}$$

where we use the Einstein summation convention throughout. Now we know that the

rate of increase of mechanical energy density is given by the sum of terms of the form $\sigma_{ij}(t)\dot{\epsilon}_{kl}(t)$, therefore:

$$\sigma_{ij}(t) = \int_{\infty}^{t} dt_2 K_{ijkl}(0, t - t_2)\dot{\epsilon}_{kl}(t_2) \tag{F.3}$$

and the rate of dissipation of mechanical energy into heat is given by:

$$\dot{D}(t) = \frac{1}{2}\int_{-\infty}^{t} dt_1 \int_{-\infty}^{t} dt_2 \frac{\partial}{\partial t} K_{ijkl}(t - t_1, t - t_2)\dot{\epsilon}_{ij}(t_1)\dot{\epsilon}_{kl}(t_2) \tag{F.4}$$

we then assume that $K_{ijkl}(t, t') = Gijkl(t-t')$ [147] where G is the relaxation function of the system. Then we find:

$$\sigma_{ij}(t) = \int_{\infty}^{t} dt_1 G_{ijkl}(t - t_1)\dot{\epsilon}_{kl}(t_1) \tag{F.5}$$

$$\dot{D}(t) = \frac{1}{2}\int_{-\infty}^{t} dt_1 \int_{-\infty}^{t} dt_2 \frac{\partial}{\partial t} G_{ijkl}(2t - t_1 - t_2)\dot{\epsilon}_{ij}(t_1)\dot{\epsilon}_{kl}(t_2) \tag{F.6}$$

Now by definition we have:

$$\epsilon_{ij}(r, t) = \frac{1}{2}(\frac{\partial u_i}{\partial x_i} + \frac{\partial u_j}{\partial x_i}) \tag{F.7}$$

and from a force balance of body and surface forces:

$$\rho\frac{\partial^2 u_i}{\partial t^2} = \frac{\partial \sigma_{ij}}{\partial x_j} + b_i \tag{F.8}$$

where ρ is the density of the material and b_i accounts for body forces such as gravity. Plugging Equations (F.5) and (F.7) into Equation (F.8) we obtain the constitutive relationship, a generalization of Equation (5.8):

$$\rho\frac{\partial^2}{\partial t^2} u_i(\mathbf{r}, t) = \frac{1}{2}\int_{-\infty}^{t} dt' \eta_{ijkl}(t - t')(u_{l,jk} + u_{k,jl})(\mathbf{r}, t') \tag{F.9}$$

where the subscripts after the comma represent differentiation with respect to the

corresponding spatial variables, and:

$$\eta_{ijkl}(t) = G_{ijkl}(0)\delta(t) + \dot{G}_{ijkl}(t)H(t) \tag{F.10}$$

are the complex moduli. In Fourier space we thus find:

$$\begin{aligned}\tilde{\sigma}_{ij}(\mathbf{r},\omega) &= \tilde{\eta}_{ijkl}(\omega)\tilde{\epsilon}_{kl}(\mathbf{r},\omega) - \rho\omega^2\tilde{u}_i(\mathbf{r},\omega) = \\ &= \frac{1}{2}\tilde{\eta}_{ijkl}(\omega)(\tilde{u}_{l,jk}(\mathbf{r},\omega) + \tilde{u}_{k,jl}(\mathbf{r},\omega))\end{aligned} \tag{F.11}$$

The exact constitutive relationships become more complicated for aging materials such as cement as there are additional associated time scales, but the basic principles are identical to the non-aging case. We refer the reader to Golden's work [147] and the references therein for additional information.

Bibliography

[1] S. Yip, editor. *Handbook of Materials Modeling*, Berlin, Germany, 2005. Springer.

[2] B. Hammer and J. K. Norskov. *Advances in Catalysis*, 45:71, 2000.

[3] J. Eapen, J. Li, and S. Yip. *Phys. Rev. Lett.*, 98:028302, 2007.

[4] M. A. Crisfield. *Non-Linear Finite Element Analysis of Solids and Structures: Advanced Topics.* John Wiley and Sons, Inc., New York, NY, USA, 1997.

[5] M. I. Baskes. *Phys. Rev. Lett.*, 59:2666, 1987.

[6] F. Ercolessi and J. B. Adams. *Europhys. Lett.*, 26:583, 1994.

[7] Y. Mishin, D. Farkas, M. J. Mehl, and D. A. Papaconstantopoulos. *Phys. Rev. B*, 59:3393, 1999.

[8] E. B. Tadmor, R. Phillips, and M. Ortiz. *Langmuir*, 12:4529, 1996.

[9] M. S. Child. *Molecular Collision Theory.* Academic Press, London, United Kingdom, 1974.

[10] T. Campbell, R. K. Kalia, A. Nakano, F. Shimojo, K. Tsuruta, and P. Vashishta. *Phys. Rev. Lett.*, 82:4018, 1999.

[11] A. Puzder, A. J. Williamson, J. C. Grossman, and G. Galli. *J. Chem. Phys.*, 117:6721, 2002.

[12] A. Kushima, X. Lin, J. Li, X. Qian, J. Eapen, J.C. Mauro, P. Diep, and S. Yip. *J. Chem. Phys.*, 130:224504, 2009.

[13] E. Wigner. *Trans. Farady Soc.*, 34:29, 1938.

[14] S. Glasstone, K. L. Laidler, and H. Eyring. *Theory of Rate Processes.* McGraw-Hill, New York, NY, USA, 1941.

[15] K. Laidler and C. King. *J. Phys. Chem.*, 87:2657, 1983.

[16] K. Laidler and C. King. *The Chemical Intelligencer*, 4:39, 1998.

[17] G.H. Vineyard. *Phys. Chem. Solids*, 3:121, 1957.

[18] R. Zwanzig. *Ann. Rev. Phys. Chem.*, 16:67, 1965.

[19] W. E, W. Ren, and E. Vanden-Eijnden. *J. Phys. Chem. B*, 109:6688, 2005.

[20] F. Ercolessi. In *Spring College in Computational Physics*, ICTP,Trieste, Italy, 1997.

[21] R. Car and M. Parrinello. *Phys. Rev. Lett.*, 55:2471, 1985.

[22] Y. C. Chen, Z. Lu, K. I. Nomura, W. Wang, R. K. Kalia, A. Nakano, and P. Vashishta. *Phys. Rev. Lett.*, 99:155506, 2007.

[23] J. R. Ray. *Phys. Rev. E*, 59:4781, 1999.

[24] J. Nose. *J. Chem. Phys.*, 81:511, 1984.

[25] M. Parrinello and A. Rahman. *J. Appl. Phys.*, 52:7182, 1981.

[26] N. Metropolis, A. W. Rosenbluth, M. N. Rosenbluth, A. H. Teller, and E. Teller. *J. Chem. Phys.*, 21:1087, 1953.

[27] A. F. Voter. In K. E. Sickafus and E. A. Kotomin, editors, *Radiation Effects in Solids*, Dordrecht, The Netherlands, 2005. NATO Publishing Unit.

[28] A. B. Bortz, M. H. Kalos, and J. L. Lebowitz. *J. Comp. Phys.*, 17:10, 1975.

[29] G. Henkelman and H. Jonsson. *J. Chem. Phys.*, 111:7010, 1999.

[30] A. Laio and M. Parrinello. *Proc. Natl. Acad. Sci.*, 99:12562, 2002.

[31] A. Laio and F. L. Gervasio. *Rep. Prog. Phys.*, 71:126601, 2008.

[32] H. Jonsson, G. Mills, and K. W. Jacobsen. Nudged elastic band method for finding minimum energy paths of transition. In B. J. Berne, G. Ciccotti, and D. F. Coker, editors, *Classical and Quantum Dynamics in Condensed Phase Simulations*, Singapore, 1998. World Scientific.

[33] L. Xu and G. Henkelman. *J. Chem. Phys.*, 129:114104, 2008.

[34] R. Martonak, A. Laio, and M. Parrinello. *Phys. Rev. Lett.*, 90:075503, 2003.

[35] P. R. Monasterio, T. T. Lau, S. Yip, and K. J. Van Vliet. *Phys. Rev. Lett.*, 103:085501, 2009.

[36] M. Iwamoto and Y. Fukai. *Mater. Trans., JIM*, 40:606, 1999.

[37] Y. Fukai. *J. Alloys and Compounds*, 356-357:263–269, 2003.

[38] E. Hayashi, Y. Kurokawa, and Y. Fukai. *Phys. Rev. Lett.*, 80:5588, 1998.

[39] T. N. Veziroglu. In *Proceedings of the Hydrogen Economy Energy Conference*, University of Miami, Coral Gables, FL, 1974.

[40] R. A. Oriani. *Ann. Rev. Mater. Sci.*, 8:327, 1978.

[41] J. P. Hirth. *Metall. Trans. A*, 11A:861, 1980.

[42] P. R. Monasterio Velasquez. Hydrogen effects on the point defect spectrum in fe-c alloys. Master's thesis, Massachusetts Institute of Technology, 2008.

[43] I.M Bernstein and A. W. Thompson, editors. *Hydrogen in Metals*, Metals Park, OH, 1974. ASM.

[44] A. W. Thompson and I. M. Bernstein, editors. *Effect of Hydrogen on Behavior of Materials*, New York, NY, 1976. TMS-AIME.

[45] I. M. Robertson. *Engineering Fracture Mechanics*, 64:649, 1999.

[46] P. Sofronis, Y. Liang, and N. Aravas. *Eur. J. Mech. A/Solids*, 20:857, 2001.

[47] Y. Liang, P. Sofronis, and N. Aravas. *Acta Materialia*, 51:2717–2730, 2003.

[48] M. Nagumo, K. Takai, , and N. Okuda. *J. Alloys and Compounds*, 293-295:310–316, 1999.

[49] M. Nagumo, K. Ohta, and H. Saitoh. *Scripta Materialia*, 40:313–319, 1999.

[50] M. Nagumo, M. Nakamura, and K. Takai. *Metall. Mater. Trans. A*, 32A:339–347, 2001.

[51] M. Nagumo. *ISIJ International*, 41(6):590–598, 2001.

[52] M. Nagumo, T. Ishikawa, T. Endoh, and Y. Inoue. *Scripta Materialia*, 49:837–842, 2003.

[53] G. Kresse and J. Furthmuller. *Phys. Rev. B*, 54:169, 1996.

[54] P. E. Blochl. *Phys. Rev. B*, 50:17953, 1994.

[55] M. Methfessel and A. T. Paxton. *Phys. Rev. B*, 40:3616, 1989.

[56] C. Forst, J. Slycke, K. Van Vliet, and S. Yip. *Phys. Rev. Lett.*, 96:175501, 2006.

[57] A. Vehanen et al. *Phys. Rev. B*, 26:762, 1982.

[58] H. D. Carstanjen. *Phys. Status Solidi A*, 59:11, 1980.

[59] C. G. Chen and H. K. Birnbaum. *Phys. Status Solidi*, 36a:687, 1976.

[60] Y. Tateyama and T. Ohno. *Phys. Rev. B*, 67:174105, 2003.

[61] S. M. Myers et al. *Rev. Mod. Phys.*, 64:559, 1992.

[62] This image was made with VMD software support. VMD is developed with NIH support by the Theoretical and Computational Biophysics group at the Beckman Institute, University of Illinois at Urbana-Champaign.

[63] D. A. Jones. *Principles and Prevention of Corrosion.* Prentice Hall, Upper Saddle River, NJ, USA, 1996.

[64] J. Li. *Modelling Simul. Mater. Sci. Eng.*, 11:173, 2003.

[65] T. T. Lau, X. Lin, S. Yip, and K. J. Van Vliet. Submitted.

[66] J. Bardeen and C. H. Herring. In W. Shockley, editor, *Imperfections in Nearly Perfect Crystals*, page 261, New York, USA, 1952. John Wiley and Sons.

[67] K. Compaan and Y. Haven. *Trans. Faraday Soc.*, 52:786, 1956.

[68] D. A. Faux and D. K. Ross. *J. Phys. C: Solid State Phys.*, 20:1441, 1987.

[69] I. V. Belova, D. S. Gentle, and G. E. Murch. *Phil. Mag. Lett.*, 82:37, 2002.

[70] C. D. Beachem. *Metall. Trans.*, 3:437, 1972.

[71] J. P. Hirth. In *Environment Sensitive Fracture of Metals and Alloys*, page 79, Arlington, VA, 1987. Office of Naval Research.

[72] H. K. Birnbaum. In *Environment Sensitive Fracture of Metals and Alloys*, page 105, Arlington, VA, 1987. Office of Naval Research.

[73] G. Lu et al. *Phys. Rev. Lett.*, 87:095501, 2001.

[74] G. Lu et al. *Phys. Rev. B*, 65:064102, 2002.

[75] T. Matsumoto, J. Eastman, and H. K. Birnbaum. *Scripta Metall.*, 15:1033, 1981.

[76] H. K. Birnbaum. *Mat. Sci. and Eng.*, A176:191, 1994.

[77] Yu. Jagodzsinski et al. *Scripta Materialia*, 43:245, 2000.

[78] M. Kabir, T. T. Lau, D. Rodney, S. Yip, and K. J. Van Vliet. In review.

[79] L. K. Mansur. *J. Nucl. Mat.*, 216:97, 1994.

[80] M. T. Robinson. *J. Nucl. Mat.*, 216:1, 1994.

[81] C. Cawthorne and E. Fulton. *Nature*, 216:575, 1967.

[82] P. T. Heald. *Philos. Mag.*, 31:551, 1975.

[83] K. C. Russell. *Acta Met.*, 19:753, 1971.

[84] A. D. Brailsford and R. Bullough. *J. Nucl. Mat.*, 44:121, 1972.

[85] L. K. Mansur. *Nucl. Technol.*, 40:5, 1978.

[86] F. A. Garner and W. G. Wolfer. *J. Nucl. Mat.*, 122/123:201, 1984.

[87] T. Okita, T. Sato, N. Sekimura, F. A. Garner, and L. R. Greenwood. *J. Nucl. Mat.*, 307:322, 2002.

[88] M. P. Surh, J. B. Sturgeon, and W. G. Wolfer. *J. Nucl. Mat.*, 378:86, 2008.

[89] K. Q. Bagley, J. I. Bramman, and C. Cawthorne. In S. F. Pugh et al., editor, *Proceedings of the British Nuclear Energy Society Conference*, Reading University, UK, 1971.

[90] R. S. Nelson, D. J. Mazey, and J. A. Hudson. In S. F. Pugh et al., editor, *Proceedings of the British Nuclear Energy Society Conference*, Reading University, UK, 1971.

[91] P. R. Monasterio, B. D. Wirth, and G. R. Odette. *J. Nucl. Mat.*, 361:127, 2007.

[92] M. P. Surh, J. B. Sturgeon, and W. G. Wolfer. *J. Nucl. Mat.*, 328:107, 2004.

[93] D. S. Gelles. *J. Nucl. Mat.*, 225:163, 1995.

[94] Y. Limoge and A. Barbu. *Phys. Rev. B*, 30:2212, 1984.

[95] J. Nord, K. Nordlund, and J. Keikonen. *Phys. Rev. B*, 65:165329, 2002.

[96] H. Hsieh and S. Yip. *Phys. Rev. Lett.*, 59:2760, 1987.

[97] M. J. Caturla, T. Diaz de la Rubia, and G. Gilmer. *J. Appl. Phys.*, 77:3120, 1995.

[98] G. J. Ackland, M. I. Mendelev, D. J. Slorovitz, S. W. Han, and A. V. Barashev. *J. Phys: Condens. Matter*, 16:S2629, 2004.

[99] Y. Limoge, A. Rahman, H. Hsieh, and S. Yip. *J. Non-Cryst. Sol.*, 99:75, 1988.

[100] A. Rota et al. *Surf. Sci.*, 600:3718, 2006.

[101] B. D. Wirth and G. R. Odette. In *Multiscale Modelling of Materials: a Materials Research Society Symposium*, page 211, Boston, MA, USA, 1999.

[102] C. Domain, C. S. Becquart, and L. Malerba. *J. Nucl. Mat.*, 335:121, 2004.

[103] G. Biroli. *Nature Physics*, 3:222, 2007.

[104] C. H. Rycroft. *Multiscale Modeling of Granular Flow.* PhD thesis, Massachusetts Institute of Technology, 2007.

[105] A. S. Keys, A. R. Abate, S. C. Glotzer, and D. J. Durian. *Nature Physics*, 3:260, 2007.

[106] C. Donati et al. *Phys. Rev. Lett.*, 80:2338, 1998.

[107] D. Lootens, H. Van Damme, and P. Hébraud. *Phys. Rev. Lett.*, 90:178301, 2003.

[108] E. I. Corwin, H. M. Jaeger, and S. R. Nagel. *Nature*, 435:1075, 2005.

[109] T. S. Majmudar and R. P. Behringer. *Nature*, 435:1079, 2005.

[110] A. Nonat. *Mat. and Struc.*, 27:187, 1994.

[111] H. F. W. Taylor. *Cement Chemistry.* Thomas Telford Publishing, London, UK, second edition, 2003.

[112] P. Barret and D. Bertrandie. *J. Chim. Phys.*, 83:765, 1986.

[113] D. Damidot and A. Nonat. In A. Nonat and J. C. Mutin, editors, *Hydration and Setting of Cements*, page 23, London, UK, 1992. E and F Spon.

[114] D. Lootens, P. Hebraud, E. Lecolier, and H. Van Damme. *Oil and Gas Sci. and Tech.*, 59:31, 2004.

[115] S. P. Jiang, J. C. Mutin, and A. Nonat. *Cem. Concr. Res.*, 25:779, 1995.

[116] S. P. Jiang, J. C. Mutin, and A. Nonat. *Cem. Concr. Res.*, 26:491, 1996.

[117] L. Nachbaur, P. C. Nkinamubanzi, A. Nonat, and J. C. Mutin. *J. Coll. Interf. Sci.*, 202:261, 1998.

[118] J. J. Thomas, A. J. Allen, and H. M. Jennings. *J. Phys. Chem. C*, 113:19836, 2009.

[119] J. C. Maxwell. *Proc. R. Soc.*, 148:48, 1873.

[120] D. J. Evans and G. P. Morriss. *Statistical Mechanics of Nonequilibrium Liquids.* Academic Press, San Diego, CA, 1990.

[121] J. Li, A. Kushima, J. Eapen, X. Lin, X. Qian, J. C. Mauro, P. Diep, and S. Yip. *J. Chem. Phys.* Submitted.

[122] E. Del Gado and W. Kob. *Soft Matter*, 2010. In Press.

[123] H. Shiba and A. Onuki. Submitted.

[124] W. G. Hoover et al. *Phys. Rev. Ser. A*, 22:1690, 1980.

[125] D. J. Evans and G. P. Morriss. *Phys. Rev. Ser. A*, 30:1528, 1984.

[126] H. M. Jennings. *Cem. Concr. Res.*, 30:101, 2000.

[127] H. M. Jennings. *Cem. Concr. Res.*, 38:855, 2008.

[128] F. Ridi. *J. Phys. Chem. B*, 113:3080, 2009.

[129] R. Alizadeh, L. Raki, J. Makar, J. Beaudoin, and I. Moudrakovski. *J. Mater. Chem*, 19:7937, 2009.

[130] M. Ciccotti. *J. Phys. D: Appl. Phys.*, 42:214006, 2009.

[131] R. J.-M. Pellenq, A. Kushima, R. Shahsavari, K. J. Van Vliet, M. J. Buehler, S. Yip, and F.-J. Ulm. *Proc. Natl. Acad. Sci.*, 106:16102, 2009.

[132] K. S. Anseth, C. M. Wang, and C. N. Bowman. *Macromolecules*, 27:650, 1994.

[133] V. Normand, S. Muller, J-C. Ravey, and A. Parker. *Macromolecules*, 33:1063, 2000.

[134] G. Henkelman and H. Jonsson. *J. Chem. Phys.*, 115:9657, 2001.

[135] M. A. Snyder, A. Chatterjee, and D. G. Vlachos. *Computers and Chemical Engineering*, 29:701, 2005.

[136] E. Martinez, J. Marian, M.H. Kalos, and J.M. Perlado. *J. Comp. Phys.*, 227:3804, 2008.

[137] B. D. Lubachevsky. *J. Comp. Phys.*, 75:103, 1988.

[138] G. Korniss, Z. Toroczkai, M. A. Novotny, and P. A. Rikvold. *Phys. Rev. Lett.*, 84:1351, 2003.

[139] G. Korniss, M. A. Novotny, H. Guclu, Z. Toroczkai, and P. A. Rikvold. *Science*, 299:677, 2003.

[140] Y. Shim and J. G. Amar. *Phys. Rev. B*, 71:115436, 2005.

[141] E. Martinez, P. R. Monasterio, and J. Marian. Submitted.

[142] J. Li. *Modeling Microstructural Effects on Deformation Resistence and Thermal Conductivity.* PhD thesis, Massachusetts Institute of Technology, 2000.

[143] H. F. W. Taylor. *Adv. Cem. Bas. Mat.*, 1:38, 1993.

[144] E. Bonaccorsi, S. Merlino, and A. R. Kampf. *J. Am. Ceram. Soc.*, 88:505, 2005.

[145] E. Bonaccorsi, S. Merlino, and H. F. W. Taylor. *Cem. Con. Res.*, 34:1481, 2004.

[146] A.J. Allen, J. J. Thomas, and H. M. Jennings. *Nature Materials*, 6:311, 2007.

[147] J. M. Golden and G. A. C. Graham. *Boundary Value Problems in Linear Viscoelasticity.* Springer-Verlag, Berlin, Germany, 1988.